PSEUDO-POTENTIAL LATTICE BOLTZMANN MODEL FOR WETTABILITY GRADIENT-BASED MICRODROPLET MANIPULATION

A Dissertation Presented

by

Adebayo Adeniran Adebiyi

to

The Department of Mechanical and Industrial Engineering

in partial fulfillment of the requirements
for the degree of

Doctor of Philosophy

in the field of

Mechanical Engineering

Northeastern University
Boston, Massachusetts

May 2017

ACKNOWLEDGEMENTS

First, I give glory to God who by His mercy and grace has allowed me to start and finish this PhD program.

I would like to thank my advisor Professor Mohammad Taslim for supporting, encouraging and guiding me throughout my study here at Northeastern University. I especially thank you for the opportunity to independently pursue a research that I am interested in. Also, I thank you for you are always available to discuss problems and your many instructions that guided me through my research.

I extend many thanks to the members of my dissertation committee, Professor John Cipolla and Professor Jaydeep Bardhan. Thank you for your time and consideration. My warm regards go to the front office staffs of the Mechanical and Industrial engineering department, whom on many occasions have assisted in different capacities.

I would like to thank my many mentors for the numerous words of encouragement, spiritual support and contributions towards the success of my studies. They are: Mr. Ayo-Yakubu Owolewa, Mrs. Bolade Owolewa, Dr. Sheila Nutt, Dr. Keith Crawford, Pastor and Pastor (Mrs.) Sorinmade.

Finally, I would like to express my sincere gratitude to my family, my father Jacob, my mother Felicia and by siblings: Adenike, Adewale and Adedoyin. You all have supported me throughout my entire life. I thank you for your unconditional love and unlimited moral support.

TABLE OF CONTENTS

LIST OF FIGURES

LIST OF TABLES

ABSTRACT

In the past few years, there has been a rapid growth of sample-in/answer-out micro total analysis technology (also called lab-on-chip). These platforms can integrate standardized lab protocols in a single device. Initially, continuous flow systems have been the default approach for fluid handling for these technologies, however, the use of droplet-based system have become increasingly popular. Droplet handling methods are often the source of system complexity and operational problems. For example, these methods often require incorporation of complex microfluidic components such as: micropumps, microvalve, tube connections and other active controls that require external off-chip controllers. Therefore, an in-depth understanding of droplet dynamics behavior is essential for improving the overall efficiency of droplet-based microfluidic systems. Especially those systems that employ passive on-chip droplet manipulation.

The focus of this work is wedge-patterned wettability gradient passive on-chip droplet manipulation. Specifically, this work investigated the effect of different droplet parameters, namely: wedge-surface relative wettability, pattern wedge angle, initial droplet position and gravitational acceleration on the droplet dynamic behavior on a numerical basis. To this end, we used the lattice Boltzmann method (LBM)-an alternative powerful method for solving fluid dynamics problems.

1. CHAPTER ONE: DISCRETE FLOW SYSTEMS

Studies in discrete flow systems (Droplet-based systems) continue to garnered significant interest because of its many applications in different industries and scientific research. For example, droplet based systems have many applications in different areas such as in miniaturized total analysis systems (Xing et al., 2013) (microfluidics), biological systems (Hodges and Jensen, 2002), enhanced oil recovery (Genabeek and Rothman, 1996), precision film coating (Dimitrakopoulos and Higdon, 1997), and cooling operations (Kumari et al., 2010; Freund et al., 2010). These applications often involve processes that include the formation and manipulation of freely suspended or attached droplets. To improve the design and overall efficiencies of these processes, the fluid flow and geometry configuration parameters that affect these designs require extensive investigations. Although processes that involve freely suspended droplets have been addressed by several studies, more investigations are needed in processes that involve droplet interaction with solid substrate.

Researchers, in several studies, have employed analytical (Blawzdziewicz et al., 2002a; 2002b), experimental (Ha et al., 2003; Tucker and Moldenaers, 2002) and numerical methods to understand droplet dynamics. For many droplet-based systems of interest, analytical studies often require some simplifying assumptions (for geometry and flow variables) and experimental studies are often empirical in nature. Therefore, direct numerical solutions have become increasingly important.

These numerical methods can be generally grouped into two categories – interface tracking methods (IT) and interface capturing methods (IC). Interface tracking method consists of the boundary integral method (Yeo et al., 2003; Pozrikidis, 2002; Cristini et al., 2001), finite element method (Manservisi and Scardovelli, 2009; Notz et al., 2001), and immersed boundary conditions (Shin and Juric, 2002; Tryggavson et al., 2001; Nobari et al., 1996). In these IT methods, the computational mesh lay in part or fully on the fluid-fluid interface such that complex cut-and-connect algorithm is often required in some of these methods for the simulation to proceed through droplet evolution (Shin and Juric, 2002; Trygagvason, 2001). In addition, these methods are limited in their ability to provide a robust understanding of the underlying microscopic dynamics at a much more fundamental level. The IC methods include constrained interpolation profile method (Takashi et al., 2001), level-set method (Lee and Son, 2011; Sussman et al., 1994; Osher and Fedkiw, 2001), volume-of-fluid method (Nikolopoulos et al., 2009; Scardovelli and Zaleski, 1999; Xian et al., 2013) and lattice Boltzmann equation method (Gong and Chen, 2012; Kang et al., 2005; Zhang et al., 2013). For these methods, the fluid-fluid interface evolves through the mesh because the mesh elements do not lie on the interface. Among the interface capturing method mentioned above, only lattice Boltzmann method does not describe the flow at the macroscopic scale directly. It is based on simplified mesoscopic kinetic model that relies on macroscopic averaged properties to capture the macroscopic dynamics (Shan and Chen, 1993). This method can simulate surface dynamics and wetting conditions in a parallel fashion and because the interface is not tracked, the computational cost is further reduced. Furthermore, since the interface region is characterized by large range of spatial-temporal scales, the lattice Boltzmann equation method is particularly suitable for modeling these interfacial dynamics.

Navier-Stokes (N-S) computational fluid dynamics (CFD) is a set of numerical techniques applied to the fluid conservation equations to obtain approximate solutions to the fluid flow as well as mass transfers. Although, traditional N-S CFD is a promising method for understanding droplet dynamic behavior, it however has some drawbacks such as high cost of computational resources required to incorporate microscopic interaction, introduction of numerical diffusion in volume of fluid (VOF), and mass conservation problems near the interface. Unlike traditional N-S CFD, an alternative powerful method for solving fluid dynamics problems is the lattice Boltzmann method (Qian and Orszag 1993; Chen and Doolen 1998) (LBM). This method is based on microscopic models and mesoscopic kinetic equations. It can simulate fluid dynamics at a reduced computation cost and promotes parallelization because all information transfer is local in time and space. In addition, it is also able to handle interfacial dynamics effectively for multiphase problems because the governing equations are developed based on microscopic description of fluid. Hence, the interaction between the phases can be naturally included. In LBM, the fluid is replaced with fictitious particles that reside on a lattice. These particles collide at the lattice site and stream along given lattice links with discrete velocities that can be represented by some velocity distribution functions. Consequently, the hydrodynamic moments of these distribution functions provide the connection to the macroscopic fluid properties. Owing to its simplicity, the lattice Bhatnagar-Gross-Krook (BGK) equation based on a single-relaxation-time approximation to the Boltzmann equation (BE) is the most popular LBM (Bhatnagar et al., 1954; Qian et al., 1992; Chen et al., 1992). However, it is well known that the BGK model exhibits viscosity-dependent truncation errors that in turn affects the quality of the results in term of numerical stability/accuracy (D’Humières and Ginzburg, 2009). Some alternatives to the BGK model have been proposed to overcome this flaws, such as; the entropic lattice Boltzmann equation (ELBE) method (Karlin et al., 1999; Ansumali and Karlin, 2002), the two-relaxation-time (TRT) method (Ginzburg, 2005; Ginzburg, 2008; D’Humières and Ginzburg, 2009) and multi-relaxation time (MRT) method (D’Humières, 1994; Lallemand et al., 2000, D’Humières, 2002). Overview of some of these methods are provided in this paper.

1.1 Background and Relevance

In the past few years, there has been a growing interest in the development of sample-in/answer-out (Culbertson et al., 2014) micro total analysis technology (Manz et al., 1990; Harrison et al., 1992) (also called lab-on-chip). One of the challenges faced by researchers in the design of these microfluidic platforms is the complexity in incorporating all the different microfluidic components into a fully automated platform that can perform some standardized biochemical protocols on a single miniaturized device (Mark et al., 2010). This has led to the development of different arrays of microfluidic systems that can be classified according to their fluid actuation principle, namely: capillary driven microfluidics (Zimmermann et al., 2009; Gervais and Delamarche 2009) , pressure driven microfluidics (Wu et al., 2008; Yamada and Seki 2006; Bhagat et al 2008) , electrowetting-on-dielectric (Lee et al., 2002; Pollack et al., 2000) , electrokinetics (Unni et al., 2007; Chang and Yang 2007), centrifugal microfluidics (Madou et al., 2001; Duffy et al., 1999) and acoustic microfluidics (Beyssen et al., 2006; Wixforth et al., 2004).

Recently, discrete flow microfluidic platforms have become increasingly popular (Teh et al., 2008; Huebner et al., 2008). These platforms use droplet-based systems and provide a unique opportunity to monitor different biochemical processes in a small volume environment and the ability to perform parallel experiments without increasing the device size or complexity. Especially, the high surface-to-volume ratio droplets not only enhance mass and heat transfer but also can be controlled by electrically induced forces or electrowetting (Sung et al., 2003).

Meanwhile, different droplet handling techniques in droplet-based applications are often the source of system complexity and operational problems. For example, these methods sometimes require incorporation of complex microfluidic components such as: micorpumps, microvalves, tube connections and other active controls that require external off-chip controllers (Sin et al., 2011). Addition of these components introduces complexities into the system and decreases the portability of such devices and increases experimental uncertainty.

Accordingly, the area of focus of many works has been dedicated to the elimination of these off-chip control elements and improving the portability of these droplet-based microfluidic devices. As such, purely passive on-chip droplet manipulation has become increasingly significant. Particularly in the design and optimization of point-of-care (POC) devices. These are devices that are low cost, portable, robust, and promotes ease of use. These devices are often essential for public health intervention in resource-poor, remote and developing countries. Therefore, an in-depth understanding of droplet dynamics behavior is essential for improving the overall efficiency of droplet-based microfluidic systems. Especially those systems that employ passive on-chip droplet manipulation.

Over the past few years, different passive on-chip droplet manipulation methods have been designed by researchers. Experimental investigations by Nakashima et al., (2015), Khoo and Tseng (2009) and Ghosh et al., (2014) have demonstrated that carefully designed wedge-shaped wettability pattern can be used to automatically transport droplet on different surfaces. As a fundamental element, these methods are designed to better exploit the capillary force imbalance that is created by spatial gradient of surface wettability. In a recent study, Xianhua et al., (2016) employed a combination of numerical and experimental methods to demonstrate droplet removal and water collection on a wedged-shaped wettability patterned surface. It is noteworthy that the numerical simulation in this study consist of a droplet on a single wedge, although in the experiment the droplet was on multiple wedges.

Although in these studies, researchers were successful in transporting the droplet a distance on the microchannel, however, their techniques are often empirical and not founded on a rigorous exploration and understanding of the droplet dynamic and the parameters that affects these dynamics. In addition, some of these empirical studies often involve droplet on a multi-wedge patterned surface (Nakashima et al., 2015; Xianhua et al., 2016). To the best of our knowledge, there is yet to be a numerical study that focuses on the interactions between the droplet and multiple wedges. Therefore, in our study we will provide a numerical framework to explore and understand the effect of different droplet parameters on the droplet dynamics on a multi-wedge patterned surface. Furthermore, the simulations by Xianhua et al., (2016) used a numerical method that is a combination of traditional Navier-Stokes-based computational fluid dynamics (N-S CFD) with front capturing or front tracking methods such as volume of fluid (VOF) (Hirt and Nichols, 1981) or level set method (L-S) (Sussman at al., 1998). Therefore, for the current study we used the lattice Boltzmann method (LBM)-an alternative powerful method for solving fluid dynamics problems. The main objective of the current study is to investigate the effect of different droplet parameters namely: density ratio, viscosity ratio, advancing and receding contact angles on the droplet dynamic behavior. To achieve this, we considered different droplet physical systems and our immediate aims are:

- Evaluate the performance of different pseudo-potential wetting schemes in the context of multicomponent multiphase lattice Boltzmann (BGK) models using two benchmark tests: (i) migration of a droplet placed on a vertical ideal wall under the influence of gravity and (ii) deformation-breakup-coalescence of a droplet past obstacles under the influence of gravity.
- Propose a new adhesion interaction force model for single component multiphase lattice Boltzmann (BGK) models and applied it to numerically investigate the effect of different droplet-surface parameters on the automatic motion of a droplet on a wedge-shaped patterned microchannel surface.
- Extended our investigation in the second aim by incorporating recent advancements in lattice Boltzmann models addressing some of the short -comings of the multiphase lattice Boltzmann method. Particularly, incorporating the appropriate equation of states and the problem of thermodynamic inconsistencies.

1.2 Unique Opportunities

This study presents a unique framework that can be employed to design and optimize passive on-chip droplet manipulation techniques and corresponding point-of-care (POC) technology. Considering that infectious disease is the second most common cause of death (WHO[1]), the need for a quick turn-around time for identification of infectious agent is of great importance. The development of genetic based molecular diagnostics has provided processes that have greatly reduced this turn-around time. One of the major advantages of point-of-care sample-in/answer-out micro total analysis systems is the opportunity to incorporating this genetic based molecular processes on such device. In addition, POC devices have also been applied to medical situations in which a fast or early diagnostic is of great importance. For example, in diagnosis and treatment of heart attack and early cancer detection.

---

[1] WHO. The world health report 2004-changing history. 2004

1.3 References

Ansumali S, Karlin IV (2002) Entropy Function Approach to the Lattice Boltzmann Method Journal of Statistical Physics 107:291-308 doi:10.1023/A:1014575024265

Beyssen D, Le Brizoual L, Elmazria O, Alnot P (2006) Microfluidic device based on surface acoustic wave Sensors and Actuators B: Chemical 118:380-385 doi:http://dx.doi.org/10.1016/j.snb.2006.04.084

Bhagat AAS, Kuntaegowdanahalli SS, Papautsky I (2008) Continuous particle separation in spiral microchannels using dean flows and differential migration Lab on a Chip 8:1906-1914 doi:10.1039/B807107A

Bhatnagar PL, Gross EP, Krook M (1954) A Model for Collision Processes in Gases. I. Small Amplitude Processes in Charged and Neutral One-Component Systems Physical Review 94:511-525

Bławzdziewicz J, Cristini V, Loewenberg M (2002) Critical behavior of drops in linear flows. I. Phenomenological theory for drop dynamics near critical stationary states Physics of Fluids 14:2709-2718 doi:doi:http://dx.doi.org/10.1063/1.1485076

Chang C-C, Yang R-J (2007) Electrokinetic mixing in microfluidic systems Microfluidics and Nanofluidics 3:501-525 doi:10.1007/s10404-007-0178-z

Chen H, Chen S, Matthaeus WH (1992) Recovery of the Navier-Stokes equations using a lattice-gas Boltzmann method Physical Review A 45:R5339-R5342

Chen S, Doolen GD (1998) LATTICE BOLTZMANN METHOD FOR FLUID FLOWS Annual Review of Fluid Mechanics 30:329-364 doi:10.1146/annurev.fluid.30.1.329

Cristini V, Bławzdziewicz J, Loewenberg M (2001) An Adaptive Mesh Algorithm for Evolving Surfaces: Simulations of Drop Breakup and Coalescence Journal of Computational Physics 168:445-463 doi:http://dx.doi.org/10.1006/jcph.2001.6713

Culbertson CT, Mickleburgh TG, Stewart-James SA, Sellens KA, Pressnall M (2014) Micro Total Analysis Systems: Fundamental Advances and Biological Applications Analytical Chemistry 86:95-118 doi:10.1021/ac403688g

d’Humières D (1994) Generalized Lattice-Boltzmann Equations. In: Rarefied Gas Dynamics: Theory and Simulations. Progress in Astronautics and Aeronautics. American Institute of Aeronautics and Astronautics, pp 450-458.
doi:doi:10.2514/5.9781600866319.0450.0458
10.2514/5.9781600866319.0450.0458

d’Humières D (2002) Multiple–relaxation–time lattice Boltzmann models in three dimensions Philosophical Transactions of the Royal Society of London Series A: Mathematical, Physical and Engineering Sciences 360:437

d’Humières D, Ginzburg I (2009) Viscosity independent numerical errors for Lattice Boltzmann models: From recurrence equations to “magic” collision numbers Computers & Mathematics with Applications 58:823-840 doi:http://dx.doi.org/10.1016/j.camwa.2009.02.008

Dimitrakopoulos P, Higdon JJL (1997) Displacement of fluid droplets from solid surfaces in low-Reynolds-number shear flows Journal of Fluid Mechanics 336:351-378

Duffy DC, Gillis HL, Lin J, Sheppard NF, Kellogg GJ (1999) Microfabricated Centrifugal Microfluidic Systems: Characterization and Multiple Enzymatic Assays Analytical Chemistry 71:4669-4678 doi:10.1021/ac990682c

Freund S, Pautsch AG, Shedd TA, Kabelac S (2007) Local heat transfer coefficients in spray cooling systems measured with temperature oscillation IR thermography International Journal of Heat and Mass Transfer 50:1953-1962 doi:http://dx.doi.org/10.1016/j.ijheatmasstransfer.2006.09.028

Gambosi TI (1994) Kinetic theory of gases Cambridge atmospheric and space science series

Genabeek Ov, Rothman DH (1996) MACROSCOPIC MANIFESTATIONS OF MICROSCOPIC FLOWS THROUGH POROUS MEDIA: Phenomenology from Simulation Annual Review of Earth and Planetary Sciences 24:63-87 doi:10.1146/annurev.earth.24.1.63

Gervais L, Delamarche E (2009) Toward one-step point-of-care immunodiagnostics using capillary-driven microfluidics and PDMS substrates Lab on a Chip 9:3330-3337 doi:10.1039/B906523G

Ghosh A, Ganguly R, Schutzius TM, Megaridis CM (2014) Wettability patterning for high-rate, pumpless fluid transport on open, non-planar microfluidic platforms Lab on a Chip 14:1538-1550 doi:10.1039/C3LC51406D

Ginzburg I (2005) Equilibrium-type and link-type lattice Boltzmann models for generic advection and anisotropic-dispersion equation Advances in Water Resources 28:1171-1195 doi:http://dx.doi.org/10.1016/j.advwatres.2005.03.004

Ginzburg I (2008) Consistent lattice Boltzmann schemes for the Brinkman model of porous flow and infinite Chapman-Enskog expansion Physical Review E 77:066704

Gong S, Cheng P (2012) Numerical investigation of droplet motion and coalescence by an improved lattice Boltzmann model for phase transitions and multiphase flows Computers & Fluids 53:93-104 doi:http://dx.doi.org/10.1016/j.compfluid.2011.09.013

Ha JW, Yoon Y, Leal LG (2003) The effect of compatibilizer on the coalescence of two drops in flow Physics of Fluids 15:849-867 doi:doi:http://dx.doi.org/10.1063/1.1555803
Harrison DJ, Manz A, Fan Z, Luedi H, Widmer HM (1992) Capillary electrophoresis and sample injection systems integrated on a planar glass chip Analytical Chemistry 64:1926-1932 doi:10.1021/ac00041a030

Hirt CW, Nichols BD (1981) Volume of fluid (VOF) method for the dynamics of free boundaries Journal of Computational Physics 39:201-225 doi:http://dx.doi.org/10.1016/0021-9991(81)90145-5

Hodges SR, Jensen OE (2002) Spreading and peeling dynamics in a model of cell adhesion Journal of Fluid Mechanics 460:381-409

Huebner A, Sharma S, Srisa-Art M, Hollfelder F, Edel JB, deMello AJ (2008) Microdroplets: A sea of applications? Lab on a Chip 8:1244-1254 doi:10.1039/B806405A

Kang Q, Zhang D, Chen S (2005) Displacement of a three-dimensional immiscible droplet in a duct Journal of Fluid Mechanics 545:41-66

Karlin IV, Ferrante A, Öttinger HC (1999) Perfect entropy functions of the Lattice Boltzmann method EPL (Europhysics Letters) 47:182

Khoo HS, Tseng F-G (2009) Spontaneous high-speed transport of subnanoliter water droplet on gradient nanotextured surfaces Applied Physics Letters 95:063108 doi:doi:http://dx.doi.org/10.1063/1.3197574

Kumari N, Bahadur V, Hodes M, Salamon T, Kolodner P, Lyons A, Garimella SV (2010) Analysis of evaporating mist flow for enhanced convective heat transfer International Journal of Heat and Mass Transfer 53:3346-3356 doi:http://dx.doi.org/10.1016/j.ijheatmasstransfer.2010.02.027

Lallemand P, Luo L-S (2000) Theory of the lattice Boltzmann method: Dispersion, dissipation, isotropy, Galilean invariance, and stability Physical Review E 61:6546-6562

Lee J, Moon H, Fowler J, Schoellhammer T, Kim C-J (2002) Electrowetting and electrowetting-on-dielectric for microscale liquid handling Sensors and Actuators A: Physical 95:259-268 doi:http://dx.doi.org/10.1016/S0924-4247(01)00734-8

Madou MJ, Lee LJ, Daunert S, Lai S, Shih C-H (2001) Design and Fabrication of CD-like Microfluidic Platforms for Diagnostics: Microfluidic Functions Biomedical Microdevices 3:245-254 doi:10.1023/a:1011419515576

Manservisi S, Scardovelli R (2009) A variational approach to the contact angle dynamics of spreading droplets Computers & Fluids 38:406-424 doi:http://dx.doi.org/10.1016/j.compfluid.2008.05.001

Manz A, Graber N, Widmer HM (1990) Miniaturized total chemical analysis systems: A novel concept for chemical sensing Sensors and Actuators B: Chemical 1:244-248 doi:http://dx.doi.org/10.1016/0925-4005(90)80209-I

Mark D, Haeberle S, Roth G, von Stetten F, Zengerle R (2010) Microfluidic lab-on-a-chip platforms: requirements, characteristics and applications Chemical Society Reviews 39:1153-1182 doi:10.1039/B820557B

Nakashima Y, Nakanishi Y, Yasuda T (2015) Automatic droplet transportation on a plastic microfluidic device having wettability gradient surface Review of Scientific Instruments 86:015001 doi:doi:http://dx.doi.org/10.1063/1.4905530

Nikolopoulos N, Nikas KS, Bergeles G (2009) A numerical investigation of central binary collision of droplets Computers & Fluids 38:1191-1202 doi:http://dx.doi.org/10.1016/j.compfluid.2008.11.007

Nobari MR, Jan YJ, Tryggvason G (1996) Head-on collision of drops—A numerical investigation Physics of Fluids 8:29-42 doi:doi:http://dx.doi.org/10.1063/1.868812

Notz PK, Chen AU, Basaran OA (2001) Satellite drops: Unexpected dynamics and change of scaling during pinch-off Physics of Fluids 13:549-552 doi:doi:http://dx.doi.org/10.1063/1.1343906

Pollack MG, Fair RB, Shenderov AD (2000) Electrowetting-based actuation of liquid droplets for microfluidic applications Applied Physics Letters 77:1725-1726 doi:doi:http://dx.doi.org/10.1063/1.1308534

Pozrikidis C (2002) Expansion of a two-dimensional foam Engineering Analysis with Boundary Elements 26:495-504 doi:http://dx.doi.org/10.1016/S0955-7997(01)00102-3

Qian YH, Humières DD, Lallemand P (1992) Lattice BGK Models for Navier-Stokes Equation EPL (Europhysics Letters) 17:479

Qian YH, Orszag SA (1993) Lattice BGK Models for the Navier-Stokes Equation: Nonlinear Deviation in Compressible Regimes EPL (Europhysics Letters) 21:255

Scardovelli R, Zaleski S (1999) DIRECT NUMERICAL SIMULATION OF FREE-SURFACE AND INTERFACIAL FLOW Annual Review of Fluid Mechanics 31:567-603 doi:doi:10.1146/annurev.fluid.31.1.567

Shan X, Chen H (1993) Lattice Boltzmann model for simulating flows with multiple phases and components Physical Review E 47:1815-1819

Shin S, Juric D (2002) Modeling Three-Dimensional Multiphase Flow Using a Level Contour Reconstruction Method for Front Tracking without Connectivity Journal of Computational Physics 180:427-470 doi:http://dx.doi.org/10.1006/jcph.2002.7086

Sin MLY, Gao J, Liao JC, Wong PK (2011) System Integration - A Major Step toward Lab on a Chip Journal of Biological Engineering 5:6 doi:10.1186/1754-1611-5-6

Sung Kwon C, Hyejin M, Chang-Jin K (2003) Creating, transporting, cutting, and merging liquid droplets by electrowetting-based actuation for digital microfluidic circuits Journal of Microelectromechanical Systems 12:70-80 doi:10.1109/JMEMS.2002.807467

Sussman M, Fatemi E, Smereka P, Osher S (1998) An improved level set method for incompressible two-phase flows Computers & Fluids 27:663-680 doi:http://dx.doi.org/10.1016/S0045-7930(97)00053-4

Teh S-Y, Lin R, Hung L-H, Lee AP (2008) Droplet microfluidics Lab on a Chip 8:198-220 doi:10.1039/B715524G

Tryggvason G et al. (2001) A front-tracking method for the computations of multiphase flow J Comput Phys 169:708-759 doi:10.1006/jcph.2001.6726

Tucker Iii CL, Moldenaers P (2002) MICROSTRUCTURAL EVOLUTION IN POLYMER BLENDS Annual Review of Fluid Mechanics 34:177-210 doi:10.1146/annurev.fluid.34.082301.144051

Unni HN, Keh HJ, Yang C (2007) Analysis of electrokinetic transport of a spherical particle in a microchannel ELECTROPHORESIS 28:658-664 doi:10.1002/elps.200600576

Wang X, Hirano H, Xie G, Xu D (2013) VOF Modeling and Analysis of the Segmented Flow in Y-Shaped Microchannels for Microreactor Systems Advances in High Energy Physics doi:10.1155/2013/732682

Wixforth A, Strobl C, Gauer C, Toegl A, Scriba J, v. Guttenberg Z (2004) Acoustic manipulation of small droplets Analytical and Bioanalytical Chemistry 379:982-991 doi:10.1007/s00216-004-2693-z

Wu X, Chon CH, Wang Y-N, Kang Y, Li D (2008) Simultaneous particle counting and detecting on a chip Lab on a Chip 8:1943-1949 doi:10.1039/B804319A

Xianhua T, Yiying Z, Tielin S, Zirong T, Guanglan L (2016) Patterned gradient surface for spontaneous droplet transportation and water collection: simulation and experiment Journal of Micromechanics and Microengineering 26:115009

Xing S, Jiang J, Pan T (2013) Interfacial microfluidic transport on micropatterned superhydrophobic textile Lab on a Chip 13:1937-1947 doi:10.1039/C3LC41255E

Yabe T, Xiao F, Utsumi T (2001) The constrained interpolation profile method for multiphase analysis J Comput Phys 169:556-593 doi:10.1006/jcph.2000.6625

Yamada M, Seki M (2006) Microfluidic Particle Sorter Employing Flow Splitting and Recombining Analytical Chemistry 78:1357-1362 doi:10.1021/ac0520083

Yeo LY, Matar OK, Perez de Ortiz ES, Hewitt GF (2003) Film drainage between two surfactant-coated drops colliding at constant approach velocity Journal of Colloid and Interface Science 257:93-107 doi:http://dx.doi.org/10.1016/S0021-9797(02)00033-4

Zhang B, Wang J, Zhang X (2013) Effects of the Hierarchical Structure of Rough Solid Surfaces on the Wetting of Microdroplets Langmuir : the ACS journal of surfaces and colloids 29:6652-6658 doi:10.1021/la400800u

Zimmermann M, Hunziker P, Delamarche E (2009) Autonomous capillary system for one-step immunoassays Biomedical Microdevices 11:1-8 doi:10.1007/s10544-008-9187-2

2. CHAPTER TWO: INTRODUCTION TO THE LATTICE BOLTZMANN METHOD

2.1 Boltzmann-Maxwell Equation

In kinetic theory, the state of a gas or gas mixture at an instant is completely specified if the distribution function of the molecular velocities and position is known throughout the gas (Gombosi, 1994). Therefore, we consider the single particle probability distribution denoted by $f(\mathbf{r}, \boldsymbol{\xi}, t)$ so that at time t, the number of molecules in the volume element $\mathrm{d}^3\mathrm{r}$ around the location $\mathbf{r}$ with velocity vector within the volume element $\mathrm{d}^3\xi$ is given by

$$\mathrm{d}^6\mathrm{N} = f(\mathbf{r}, \boldsymbol{\xi}, t)\mathrm{d}^3\mathrm{r}\mathrm{d}^3\xi \tag{2.1}$$

When an external force field is applied to each particle of the gas, the imposed external force field results in the acceleration, $\boldsymbol{a}$ of the individual molecules (this acceleration is usually assumed to be divergence free in velocity space i.e. $\nabla_\xi \boldsymbol{a} = 0$). During the interval dt, if there were no collision all the particles that were located inside the phase space element would occupy the volume element $\mathrm{d}^3\mathrm{r}'$ near the spatial location $\mathbf{r} + \boldsymbol{\xi} dt$ with velocities in the range $\mathrm{d}^3\xi'$ at velocity $\boldsymbol{\xi} + \mathbf{a}dt$. Because the particle acceleration is divergence free, we conclude that $\mathrm{d}^3\mathrm{r}\mathrm{d}^3\xi = \mathrm{d}^3\mathrm{r}'\mathrm{d}^3\xi'$ and the number of the particles in the modified set without collision is given by

$$\mathrm{d}^6\mathrm{N}' = f(\mathbf{r} + \boldsymbol{\xi} dt, \boldsymbol{\xi} + \mathbf{a}dt, t + dt)\mathrm{d}^3\mathrm{r}\mathrm{d}^3\xi \tag{2.2}$$

However, because gas molecules interact with each other via a collision process that alters the velocities of the colliding particles the total number of molecules inside the infinitesimal phase-space may change during the interval dt. This change due to collision is proportional to $\mathrm{d}^3\mathrm{r}\mathrm{d}^3\xi dt$ and is denoted by $\frac{\delta f}{\delta t}\mathrm{d}^3\mathrm{r}\mathrm{d}^3\xi dt$ where $\frac{\delta f}{\delta t}$ is the rate of change of the phase space distribution function (formally known as the collision term).

Therefore, on can write

$$f(\mathbf{r}+\boldsymbol{\xi}dt,\boldsymbol{\xi}+\mathbf{a}dt,t+dt)\mathrm{d}^3\mathrm{r}\mathrm{d}^3\xi-f(\mathbf{r},\boldsymbol{\xi},t)\mathrm{d}^3\mathrm{r}\mathrm{d}^3\xi= \frac{\delta f}{\delta t}\mathrm{d}^3\mathrm{r}\mathrm{d}^3\xi dt \tag{2.3}$$

Dividing both sides by $\mathrm{d}^3\mathrm{r}\mathrm{d}^3\xi dt$ and taking the limit $dt\rightarrow 0$ the transport equation for f can be expressed as (Huang, 1963)

$$\left(\partial_t+\boldsymbol{\xi}\cdot\nabla_{\mathbf{r}}+\mathbf{a}\cdot\nabla_{\boldsymbol{\xi}}\right)f(\mathbf{r},\boldsymbol{\xi},t)=(\partial_t f)_{\mathrm{coll}} \tag{2.4}$$

2.1.1 Collision Term

Furthermore, we can see above that the single particle distribution function f depends on the scattering of the particle due to collision with another particle. Hence, the two-body distribution function $f^{(2)}$ is required to represent the effect of the intermolecular interaction. Similarly, $f^{(2)}$ will require knowing the effect of scattering on the two particles due to collision with a third particle which will involve the three-body particle distribution function $f^{(3)}$. Eq. (2.4) can be replaced by a set of N coupled equations to account for the multi-particle interactions known as the BBGKY hierarchy (Liboff , 1969). Without closure Eq. (2.4) is not very useful. Therefore, the following simplifying assumptions are made:

- The gas is sufficiently dilute that only binary collisions are taken into account.

- The velocities of the colliding molecules are assumed to be statistically independent. Any possible correlations between the velocity and the position of any molecule are neglected. This is known as the assumption of molecular chaos.
- The effect of the external force on the collision cross-section is neglected
- Scale length of the distribution function is much larger than the range of intermolecular forces.

Based on the following assumptions, the BBGKY hierarchy can be truncated at $f^{(2)}$ and this two-particle distribution can be replaced by the product of the single particle distribution for both particles. This result in the Boltzmann equation with the collision term expressed as (Chapman and Cowling, 1970; Huang, 1963; Koga, 1970)

$$(\partial_t f)_{\mathrm{coll}} = \int d\Omega \int \mathrm{d}^3\xi^{(2)}\, \sigma(\Omega)(f'_1 f'_2 - f_1 f_2) \tag{2.5}$$

where f' and f denote the distribution function before and after collision; $\sigma(\Omega)$ is the differential cross-section of the binary collision $\{\boldsymbol{\xi}^{(1)}, \boldsymbol{\xi}^{(2)}\} \rightarrow \{\boldsymbol{\xi}'^{(1)}, \boldsymbol{\xi}'^{(2)}\}$ with scattering angle Ω.

2.1.2 Equilibrium Distribution Function

An important consequence of Eq. (2.5) is that the collision process drives the distribution function towards equilibrium state in an irreversible way. Consider a gas with spherical particles that are subject to no external force and contain only translational energy. Next we introduce the Boltzmann function,

$$\mathrm{H} = \int \mathrm{d}^3\xi\, f \ln f \tag{2.6}$$

If f satisfies the Boltzmann transport Eqs. (2.4) and (2.5), then H is a monotonically decreasing function of t,

$$\frac{\mathrm{dH(t)}}{\mathrm{dt}} \leq 0 \tag{2.7}$$

This is referred to as the H-theorem and is fully consistent with the fundamental laws of thermodynamics. It can be shown that H is related to the total entropy of a gas, i.e. $\mathrm{H} = -{}^{\mathrm{S}}/_{k_{\mathrm{B}}}$. Therefore, the theorems states that the entropy of the system increases with time until equilibrium is reached (Huang, 1963).

In addition, the equilibrium is reached when

$$f'_1 f'_2 = f_1 f_2 \tag{2.8}$$

and by definition, the total time derivative in the phase space vanishes $\frac{\partial f}{\partial t} = 0$

and $\frac{\mathrm{dH}}{\mathrm{dt}} = 0$.

The solution of Eq. (2.8) will yield the Maxwell-Boltzmann distribution function (Huang, 1963) given as

$$f^{eq} = \frac{\rho}{(2\pi RT)^{\mathrm{D}/2}} \exp\left[-\frac{(\boldsymbol{\xi} - \mathbf{u})^2}{2RT}\right] \tag{2.9}$$

where D, R, T, ρ and $\mathbf{u}$ are the spatial dimension, gas constant, temperature, macroscopic density and velocity respectively.

2.1.3 BGK Approximation

Although it is almost impossible to evaluate the Boltzmann collision integral analytically, it however can be simplified for near-equilibrium state. This leads to the collision interval theory. The basic assumption in this theory is that the fraction of the particles, in a given volume, that undergoes collisions during the time interval δ_t which alter the particle distribution function from f to f^{eq} is equal to ${}^{\delta_t}/_{\tau}$ where τ is the relaxation time constant.

This theory led to the Bhatnagar, Gross, and Krook (1954) approximation, often referred to as the BGK approximation, where the collision term can therefore be expressed as

$$(\partial_t f)_{\text{coll}} = -\frac{f - f^{eq}}{\tau} \tag{2.10}$$

such that the Boltzmann equation with the BGK collision operator becomes

$$\left(\partial_t + \boldsymbol{\xi} \cdot \nabla_{\mathbf{r}} + \mathbf{a} \cdot \nabla_{\boldsymbol{\xi}}\right) f(\mathbf{r}, \boldsymbol{\xi}, t) = -\frac{f - f^{eq}}{\tau} \tag{2.11}$$

The macroscopic equations can be obtained by integrating in the particle momentum space and are given by

Density; $$\rho = \int f \, \mathrm{d}\boldsymbol{\xi} \tag{2.12a}$$

Macroscopic velocity; $$\mathbf{u} = \frac{1}{\rho} \int f \, \boldsymbol{\xi} \mathrm{d}\boldsymbol{\xi} \tag{2.12b}$$

Stress (pressure) tensor; $$\mathbf{p} = \int f \, \boldsymbol{\xi}\boldsymbol{\xi} \mathrm{d}\boldsymbol{\xi} \tag{2.12c}$$

Heat flux; $$\mathbf{q} = \int f \, \xi^2 \boldsymbol{\xi} \mathrm{d}\boldsymbol{\xi} \tag{2.12d}$$

Kinetic energy; $$E = \frac{1}{2}\int f\,\xi^2 \mathrm{d}\boldsymbol{\xi} \qquad (2.12e)$$

2.2 Lattice Boltzmann Equation

Historically the first lattice Boltzmann equation(LBE) (McNamara and Zanetti, 1988) was proposed to address the statistical noise drawbacks of its lattice gas cellular automaton (LGCA) predecessor (Frisch et al., 1986; Wolfram, 1986). The basic idea in these studies was to construct a model based on the mean particle population instead of the discrete particles in LGCA by assuming there are no correlations between the particles. Later studies showed that the LBE can be derived by systematically discretizing the continuous Boltzmann equation. This can be achieved via three forms of discretization, namely: velocity space, physical space and time discretization. In the LBM, the physical space of interest is filled with a regular lattice and the fluid is modeled with hypothetical particles moving from one lattice site to another with velocities that belong to a discrete set of velocities and colliding with each other at the lattice sites. In this section, we present an overview of the lattice Boltzmann model for the BGK approximation of the continuous Boltzmann equation.

2.2.1 Discretizing the Microscopic Velocity Space

In the BGK approximation of the continuous Boltzmann equation, the particle distribution function is a function of space $\mathbf{r}$, particle velocity $\boldsymbol{\xi}$ and time t. The discrete version of the Boltzmann equation can be obtained by first discretizing the microscopic velocity space such that evolution of the fictitious particles is restricted to velocities that belong to a finite set of discrete velocities. From literature, the process of discretizing the velocity space can be achieved in different ways, namely; the low Mach number approach (He and Luo, 1997; Shan et al., 2006), the Hermite polynomial approach (Shan 2006) and Entropic approach (Karlin et al., 1999; Ansumali et al., 2002; Chikatamarla et al., 2006). Next we provide a brief description of the approaches mentioned above.

2.2.2 Low Mach Number Method

Referring to the work of He and Luo (1997), the lattice Boltzmann equation can be considered as a special finite-difference approximation of the Boltzmann equation. The choice of the coefficients of expansion of the equilibrium distribution function (low Mach number expansion of the Maxwellian) and the discrete particle velocity (lattice structure) are the main results of this study. For sake of simplicity, we describe the derivation of the Boltzmann-BGK equation without a body force. Details of derivation with body force can be found in (He et al., 1997; Nourgaliev, 2003). The Boltzmann-BGK equation can be written in the form of an ordinary differential equation and integrated over a time interval δ_t such that

$$\begin{aligned} f(\mathbf{r}+\boldsymbol{\xi}\delta_t, \boldsymbol{\xi}, t+\delta_t) \\ &= e^{-\delta_t/\tau} f(\mathbf{r}, \boldsymbol{\xi}, t) \\ &+ \frac{1}{\tau} e^{-\delta_t/\tau} \times \int_0^{\delta_t} e^{t'/\tau} f^{eq}(\mathbf{r}+\boldsymbol{\xi}t', \boldsymbol{\xi}, t+t') dt' \end{aligned} \tag{2.13}$$

Assuming that δ_t is small enough and $f^{eq}$is smooth enough locally, the integral on the RHS of Eq. (2.13) can be approximated using trapezoidal rule and using the series expansion of $e^{-\delta_t/\tau}$ by δ_t (neglecting terms of $O(\delta_t{}^2)$) we obtain the following equation.

$$f(\mathbf{r}+\boldsymbol{\xi}\delta_t,\boldsymbol{\xi},t+\delta_t)-\ f(\mathbf{r},\boldsymbol{\xi},t)=-\frac{\delta_t}{\tau}[f(\mathbf{r},\boldsymbol{\xi},t)-f^{eq}(\mathbf{r},\boldsymbol{\xi},t)] \tag{2.14}$$

Also, one can expand the equilibrium distribution function as a Taylor series in the limit of constant temperature T and small velocity $\mathbf{u}$ while retaining the terms up to the $O(u^2)$

$$f^{eq}=\frac{\rho}{(2\pi RT)^{\mathrm{D}/2}}\exp\left[-\frac{\boldsymbol{\xi}^2}{2RT}\right]\times\left[1+\ \frac{(\boldsymbol{\xi}\cdot\mathbf{u})}{RT}+\frac{(\boldsymbol{\xi}\cdot\mathbf{u})^2}{2(RT)^2}-\frac{\mathbf{u}^2}{2RT}\right] \tag{2.15}$$

Substituting Eq. (2.15) into the conservation laws in Eq. (2.12) we obtain the moment integral of the following for

$$\int \boldsymbol{\xi}^m f^{eq}\,d\boldsymbol{\xi} \tag{2.16}$$

The above integral will contain terms of the following type that can be evaluated by the Gaussian-type quadrature as

$$\int\frac{\rho}{(2\pi RT)^{\mathrm{D}/2}}\exp\left[-\frac{\boldsymbol{\xi}^2}{2RT}\right]p(\boldsymbol{\xi})\,d\boldsymbol{\xi}=\sum\nolimits_{\boldsymbol{\alpha}}w_\alpha\exp\left[-\frac{\boldsymbol{\xi}^2}{2RT}\right]p(\boldsymbol{\xi}_\alpha) \tag{2.17}$$

where $p(\boldsymbol{\xi})$ is the polynomial in $\boldsymbol{\xi}$, w_α are the weights, and $\boldsymbol{\xi}_\alpha$ are the discrete velocities (abscissa) of the quadrature. Hence. The conservation laws can be expressed as

$$\rho=\sum\nolimits_\alpha f_\alpha=\sum\nolimits_\alpha f_\alpha^{eq} \tag{2.18a}$$

$$\rho\mathbf{u}=\sum\nolimits_\alpha \boldsymbol{\xi}_\alpha f_\alpha=\sum\nolimits_\alpha \boldsymbol{\xi}_\alpha f_\alpha^{eq} \tag{2.18b}$$

$$\rho\varepsilon=\frac{1}{2}\sum\nolimits_\alpha(\boldsymbol{\xi}_{\boldsymbol{\alpha}}-\mathbf{u})^{\mathbf{2}}f_\alpha=\frac{1}{2}\sum\nolimits_\alpha(\boldsymbol{\xi}_{\boldsymbol{\alpha}}-\mathbf{u})^{\mathbf{2}}f_\alpha^{eq} \tag{2.18c}$$

and the discrete distribution function f_α and equilibrium function f_α^{eq} as

$$f_\alpha=\ f_\alpha(\mathbf{r},t)=\ w_\alpha f(\mathbf{r},\boldsymbol{\xi}_\alpha,t) \tag{2.19a}$$

$$f_\alpha^{eq}=\ f_\alpha^{eq}(\mathbf{r},t)=\ w_\alpha f^{eq}(\mathbf{r},\boldsymbol{\xi}_\alpha,t) \tag{2.19b}$$

Finally, the lattice Boltzmann equation is given as

$$f_\alpha(\mathbf{r} + \boldsymbol{\xi}_\alpha \delta_t, t + \delta_t) - f(\mathbf{r}, t) = -\frac{\delta_t}{\tau}\left[f_\alpha(\mathbf{r}, t) - f_\alpha^{eq}(\mathbf{r}, t)\right] \tag{2.20}$$

2.2.3 Hermite Polynomial Method

In this approach, following the work by Grad et al., (1949), one assumes that the distribution function lies entirely in the subspace spanned by the Hermite polynomial up to the order of N. Here, Hermite polynomial are chosen because the expansion coefficients are exactly moments of the distribution function. Therefore, the single particle distribution function can be expanded based on the Hermite orthogonal polynomials in vector space.

We introduce the expansion,

$$f(\boldsymbol{r},\, \boldsymbol{\xi},\, t) \approx f^N(\boldsymbol{r},\, \boldsymbol{\xi},\, t) = \omega(\xi) \sum_{n=0}^{N} \frac{1}{n!} \boldsymbol{a}^{(n)}(\boldsymbol{r},\, t) \boldsymbol{\mathcal{H}}^{(\boldsymbol{n})}(\boldsymbol{\xi}) \tag{2.21}$$

where $\boldsymbol{a}^{(n)}$ and $\boldsymbol{\mathcal{H}}^{(n)}$ are tensors of the n-th rank and given as

$$\boldsymbol{a}^{(n)}(\boldsymbol{r},\, t) = \int f(\boldsymbol{r},\, \boldsymbol{\xi},\, t) \boldsymbol{\mathcal{H}}^{(n)}(\boldsymbol{\xi}) d\boldsymbol{\xi} \tag{2.22a}$$

$$\boldsymbol{\mathcal{H}}^{(n)}(\boldsymbol{\xi}) = \frac{(-1)^n}{\omega(\xi)} \boldsymbol{\nabla}^n \omega(\boldsymbol{\xi}) \tag{2.22b}$$

Up to the N^{th} order, $f(\boldsymbol{x},\, \boldsymbol{\xi},\, t)$ has the same velocity moments as the original function $f(\boldsymbol{x},\, \boldsymbol{\xi},\, t)$.

As a partial sum of the Hermite series with finite term, the truncated distribution function in Eq. (2.21) can be completely and uniquely determined by its values at a set of discrete abscissae. The integrand in Eq. (2.2a) can be written as

$$f^N(\boldsymbol{r},\ \boldsymbol{\xi},\ t)\boldsymbol{\mathcal{H}}^{(n)}(\boldsymbol{\xi}) = \omega(\xi)p(\boldsymbol{r},\ \boldsymbol{\xi},\ t) \tag{2.23}$$

where $p(\boldsymbol{r},\ \boldsymbol{\xi},\ t)$ is a polynomial in $\boldsymbol{\xi}$ of a degree not greater than $2N$. Furthermore, we know from the rules of Gaussian quadrature that the best estimate of the integral $\int \omega(\boldsymbol{\xi})\, f(\boldsymbol{\xi}) d\boldsymbol{\xi}$ can be obtained by choosing optimal set of abscissae $\xi_i,\ i = 1, \cdots, d$ such that

$$\int \omega(\xi) f(\boldsymbol{\xi}) d\boldsymbol{\xi} \cong\ \textstyle\sum_\alpha w_\alpha f(\boldsymbol{\xi}_\alpha) \tag{2.24}$$

where $\omega(\boldsymbol{\xi})$ is an arbitrary weighting function and $w_\alpha,\ \alpha = 1, \dots, d$ a set of constant weights. Therefore,

$$\begin{gathered}\boldsymbol{a}^{(n)} = \int \omega(\boldsymbol{\xi})p(\boldsymbol{x},\ \xi,\ t)d\boldsymbol{\xi} = \textstyle\sum_\alpha w_\alpha p(\boldsymbol{x},\ \boldsymbol{\xi}_\alpha,\ t) = \\ \textstyle\sum_\alpha \frac{w_i}{\omega(\xi_\alpha)} f^N(\boldsymbol{x},\ \boldsymbol{\xi}_\alpha,\ t)\boldsymbol{\mathcal{H}}^{(n)}(\boldsymbol{\xi}_\alpha)\end{gathered} \tag{2.25}$$

Now the governing equation for $f^N(\boldsymbol{x},\ \boldsymbol{\xi}_\alpha,\ t)$ can be obtained by projecting the Boltzmann-BGK equation on a Hermite-truncated basis evaluated at $\boldsymbol{\xi}_\alpha$. This can be accomplished term by term. First the equilibrium distribution function $f^{eq}$is projected.

$$\boldsymbol{f^{eq}} \approx \omega(\xi) \textstyle\sum_{n=0}^{N} \frac{\mathbf{1}}{\boldsymbol{n}!} \boldsymbol{a}_{eq}{}^{(\boldsymbol{n})}(\boldsymbol{x}, t)\boldsymbol{\mathcal{H}}^{(\boldsymbol{n})}(\boldsymbol{\xi}) \tag{2.26}$$

where $\boldsymbol{a}_{eq}{}^{(n)} \int f^{eq}\boldsymbol{\mathcal{H}}^{(n)}(\boldsymbol{\xi})d\boldsymbol{\xi}$. This yield the following explicit term for the equilibrium distribution function up to the third order

$$f^{eq}(\boldsymbol{\xi}) =$$

$$\omega(\xi)\rho\left\{\begin{matrix} 1+\boldsymbol{\xi}\cdot\mathbf{u}+\frac{1}{2}[(\boldsymbol{\xi}\cdot\mathbf{u})^2-\mathrm{u}^2+(\theta-1)(\boldsymbol{\xi}^{\mathbf{2}}-D)] \\ +\frac{\xi\cdot\boldsymbol{u}}{\mathbf{6}}[(\boldsymbol{\xi}\cdot\boldsymbol{u})^{\mathbf{2}}-3\mathrm{u}^2+3(\theta-1)(\xi^2-D-2)] \end{matrix}\right\} \tag{2.27}$$

For an isothermal system $\theta = 1$. Directly evaluating Eq. (2.11) at $\boldsymbol{\xi}_\alpha$ and multiplying by the constant ${}^{w_\alpha}/_{\omega(\xi_\alpha)}$ yields the lattice Boltzmann equation

$$\frac{\partial f_\alpha}{\partial t}+\boldsymbol{\xi_\alpha}\cdot\nabla_{\mathrm{r}}\boldsymbol{f_\alpha} = \frac{1}{\tau}(\boldsymbol{f_\alpha} - \boldsymbol{f_\alpha}^{\boldsymbol{eq}}) \tag{2.28}$$

where $f_\alpha(\mathbf{r},t) = w_\alpha f(\mathbf{r},\, \boldsymbol{\xi_\alpha},\, t)/\omega(\xi_\alpha)$.

The left-hand-side (LHS) of the lattice Boltzmann-BGK equation derived Eq. (2.28) be discretized in configuration space $(\boldsymbol{r},\, t)$ by employing the first-order upwind finite difference approximation for the time derivative

$$\frac{\partial f_\alpha(\boldsymbol{r},\, t)}{\partial t}+\boldsymbol{\xi}_\alpha\cdot\nabla f_\alpha(\boldsymbol{r},t) \cong \frac{1}{\delta_t}[f_\alpha(\boldsymbol{r}+\boldsymbol{\xi}_\alpha\delta_t,\, t+\delta_t)-f_\alpha(\boldsymbol{r},t)] \tag{2.29}$$

Note that the spatial grid should be such that if $\boldsymbol{r}$ is a node of the grid, $\boldsymbol{r}\rightarrow\boldsymbol{r}+\boldsymbol{\xi}_\alpha$ are also nodes on the grid. The following quadrature ${E_{2,5}}^7, {E_{2,5}}^9, {E_{3,5}}^{15}$ and ${E_{3,5}}^{19}$ all satisfy this requirement.

2.2.4 Entropic Method

The aim of this approach is to define the equilibrium population as a minimum of the H function under the constraint of local conservation laws (Ansumali, 2002). In the previous approach, the discrete velocities are constructed from the zeroes of the Hermite polynomial. Here, the discrete velocity model is linked to the entropic Grad's method (maximum entropy approximation). One starts by evaluating the Boltzmann H function in Eq. (2.6) using Gauss-Hermite quadrature such that (Ansumali et al., 2002). For interested reader, more detailed derivation can be found in the following references (Karlin et al., 1999; Ansumali et al., 2002, 2006; Chikatamarla et al., 2006, Chikatamarla and Karlin, 2009)

$$H = \sum_{\alpha=1}^{d} f_\alpha \ln\left(\frac{f_\alpha}{w_\alpha}\right) \tag{2.30}$$

where w_α is the weight associated with the $\alpha -$ th discrete velocity $\boldsymbol{\xi}_\alpha$. The particle mass and the Boltzmann constant $k_{\mathrm{B}}$are set equal to unity. Also, the discrete velocity populations $f_\alpha(\boldsymbol{\xi})$ are related to the continuous single-particle distribution function at the nodes of the quadrature as $f_\alpha(\boldsymbol{\xi}) = w_\alpha (2\pi RT)^{\mathrm{D}/2} \exp\left[-\frac{\xi_\alpha^2}{2RT}\right] f(\mathbf{r}, \boldsymbol{\xi}_\alpha)$

For this review, we consider the case of a one-dimensional simulation (D = 1) isothermal hydrodynamics where the entropic function in Eq. (2.30) is constructed using the third-order Hermite polynomial. The minimizing discrete velocities are $\boldsymbol{\xi} = \{-1, 0, 1\}$ with the corresponding weights $\boldsymbol{\xi} = \{-1, 0, 1\}$. Details for higher order Hermite velocity polynomial can be found in (Chikatamarla et al., 2006)

The discrete-velocity local equilibrium minimizes the corresponding entropy function under density and momentum conservation constraint.

$$\sum_{\alpha=1}^{d} f_\alpha^{eq} \{1, \quad \xi_\alpha\} = \{\rho, \quad \rho\mathbf{u}\} \tag{2.31}$$

and the explicit solution to this conditional minimization problem yields

$$f_\alpha^{eq} = \rho w_\alpha \prod_{i=1}^{D} \left(2 - \sqrt{1 + 3u_i^2}\right) \left(\frac{2u_i + \sqrt{1 + 3u_i^2}}{1 - u_i}\right)^{\xi_{\alpha i}} \tag{2.32}$$

where the sound speed $c_s = \, ^1/_{\sqrt{3}}$ and the exponent $\xi_{\alpha i}$ takes the value $\{0, \pm 1\}$. Note that the expansion the equilibrium distribution in the equation above to the order of u^2 corresponds to the polynomial equilibria used in the lattice Boltzmann method (Ansumali et al., 2002).

Hence, the entropic lattice BGK model for the local equilibrium in Eq. (2.32) become

$$\begin{aligned} &f_\alpha(\boldsymbol{r} + \boldsymbol{\xi_\alpha}\delta_{\boldsymbol{t}}, t + \delta_{\boldsymbol{t}}) - f_\alpha(\boldsymbol{r}, t) \\ &\qquad = -\beta\alpha\big(f_\alpha(\boldsymbol{r}, t)\big) - f_\alpha^{eq}\left(\rho\big(\mathbf{f}(\boldsymbol{r}, t)\big), \mathbf{u}\big(\mathbf{f}(\boldsymbol{r}, t)\big)\right) \end{aligned} \tag{2.33}$$

where the relationship between parameter β that is used to match the viscosity coefficient in the hydrodynamic limit and the relaxation parameter in the BGK model is given by

$$\beta = \frac{\delta_{\boldsymbol{t}}}{2\tau + \delta_t} \tag{2.34}$$

Also, the over-relaxation parameter α can be computed on each lattice site from the entropy condition estimate.

$$H\left(\mathbf{f} - \alpha\big(\mathbf{f} - \mathbf{f}^{eq}(\mathbf{f})\big)\right) = H(\mathbf{f}) \tag{2.35}$$

Eq. (2.33) can reconstruct the Navier-Stokes equation with the viscosity, $\nu = c_s^2\tau = c_s^2\delta_{\boldsymbol{t}}\left(\frac{1}{2\beta} - \frac{1}{2}\right)$

Recall from (Karlin et al., 1999) that the expansion of the discrete equilibrium function in Eq. (2.32) to the second order in $\mathbf{u}$ and approximate solution of the entropy estimate in Eq. (2.35) with $\alpha = 2$ will result in the lattice BGK model below

$$f_\alpha(\boldsymbol{r} + \boldsymbol{\xi}_\alpha \delta_t, t + \delta_t) - f_\alpha(\boldsymbol{r}, t) = -\frac{2\delta_t}{2\tau + \delta_t}\left[f_\alpha^{eq}(\boldsymbol{r}, t) - f_\alpha(\boldsymbol{r}, t)\right] \tag{2.36}$$

2.3 Derivation of the Hydrodynamic Equations

The long-time and large-scale hydrodynamic behavior (Navier-Stokes equations) can be derived from the lattice Boltzmann model via the Chapman-Enskog analysis (Chapman and Cowling, 1970) or the mode analysis of the dispersion equation (von Neumann analysis) (Lallemand and Luo, 2000). In this section, we provide a brief overview of the derivation of the hydrodynamic equation using the Chapman-Enskog approach. More detailed application of this approach can be found in latter chapters of this paper.

Consider the isothermal lattice Boltzmann Eq. (2.20), a series expansion for the distribution function in terms of the lattice Knudsen number ϵ around the equilibrium distribution function can be expressed as

$$f_\alpha = f_\alpha^{(0)} + \epsilon f_\alpha^{(1)} + \epsilon^2 f_\alpha^{(2)} + \cdots = \sum_{n=0}^{\infty} f_\alpha^{(n)} \tag{2.37}$$

where $f_\alpha^{(0)} = f_\alpha^{(eq)}$ is the equilibrium distribution function.

For the first two moments of the zeroth approximation, we obtain the following macroscopic variables.

$$\sum_{\alpha} f_{\alpha} = \rho; \qquad \sum_{\alpha} f_{\alpha}\, \boldsymbol{\xi}_{\alpha} = \rho\mathbf{u} \tag{2.38}$$

The equilibrium distribution function also yield the same moment

$$\sum_{\alpha} f_{\alpha}^{(0)} = \rho; \qquad \sum_{\alpha} f_{\alpha}^{(0)} \boldsymbol{\xi}_{\alpha} = \rho\mathbf{u} \tag{2.39}$$

Hence, the higher order expansions are defined in such a way so that

$$\sum_{\alpha} f_{\alpha}^{(n)} = 0; \qquad \sum_{\alpha} f_{\alpha}^{(n)} \boldsymbol{\xi}_{\alpha} = 0, \quad \text{for n} > 0 \tag{2.40}$$

Now, substituting the expansion in Eq. (2.37) into the lattice Boltzmann Eq. (2.20) and taking the first and second discrete moment result in

Mass conservation equation,

$$\partial_t \rho + \partial_j \rho u_j = 0 \tag{2.41}$$

And the momentum conservation equation,

$$\partial_t \rho u_i + \partial_j \rho u_i u_j = -\partial_j \sum_{n=0}^{\infty} \epsilon^n \, \mathrm{P}_{ij}^{(n)}$$

where nth approximation of the pressure tensor is given as (Nourgaliev et al., 2003)

$$\mathrm{P}_{ij}^{(n)} = \sum_{n=0}^{\infty} (\xi_{\alpha i} - u_i)\,(\xi_{\alpha j} - u_j) f_{\alpha}^{(n)}$$

Taken together, lattice Boltzmann transport equation can be expressed as

$$\begin{aligned}\left[\left(\partial_{t_0} + \epsilon\partial_{t_1} + \epsilon^2\partial_{t_2} + \cdots\right) + D\right]\left(f_{\alpha}^{(0)} + \epsilon f_{\alpha}^{(1)} + \epsilon^2 f_{\alpha}^{(2)} + \cdots\right) \\ = \frac{1}{\epsilon\tau}\left[\left(f_{\alpha}^{(0)} + \epsilon f_{\alpha}^{(1)} + \epsilon^2 f_{\alpha}^{(2)} + \cdots\right) - f_{\alpha}^{eq}\right]\end{aligned} \tag{2.42}$$

with the consistent expansion $\partial_t = \partial_{t_0} + \epsilon\partial_{t_1} + \epsilon^2\partial_{t_2} + \ldots$; $Df_\alpha = \xi_{\alpha j}\partial_j f_\alpha^{(0)} + \epsilon\xi_{\alpha j}\partial_j f_\alpha^{(1)} + \epsilon^2\xi_{\alpha j}\partial_j f_\alpha^{(2)} + \ldots$ and $\partial_t \rho u_i = -\partial_j \sum_{n=0}^{\infty} \epsilon^n \sum_\alpha f_\alpha^{(n)} \xi_{\alpha i}\xi_{\alpha j}$

where $f_\alpha^{(n)}$ is defined such that the coefficients of each power of ϵ vanish separately in the equation above (Nourgaliev et al., 2003). Therefore, in other to obtain the Navier-Stokes equations only the approximations $f_\alpha^{(0)}$ and $f_\alpha^{(1)}$are required and the following equations need to be solved

$$f_\alpha^{(0)} = f_\alpha^{eq} \tag{2.43a}$$

$$\partial_{t_0} f_\alpha^{(0)} + Df_\alpha^{(0)} = -\frac{f_\alpha^{(1)}}{\tau} \tag{2.43b}$$

2.4 Boundary Conditions

Next, we provide a summary of the boundary conditions that were used for the lattice Boltzmann method in this study. Detailed description of boundary conditions in lattice Boltzmann model can be found in (Maier et al., 1996; Latt and Chopard, 2008; Zhang, 2011). Prior to the collision step, density distribution functions on the boundary nodes entering the fluid domain after the advection step are not known. The role of the boundary condition is to find a substitute for these unknown distribution functions, such that macroscopic velocity and pressure requirements are satisfied on the domain boundary. Therefore, it is imperative that the different boundary conditions are implemented on the boundary nodes in a way that will produce the same dynamics as the bulk nodes.

2.4.1 No-Slip

The no-slip boundary condition constrains a fluid locally to have the same tangential velocity as the wall that confine it. It is commonly implemented with the standard bounce-back condition. In this method, the boundary condition is resolved on links crossing the solid boundary from the solid to the fluid lattice nodes such that the momentum parallel to the boundary is conserved and the perpendicular momentum is reserved. However, since the primitive variable in the LBM is the particle distribution function and not the velocity field, enforcement of zero velocity through the distribution function may not be enough. Therefore, the implementation should ensure that the momentum flux condition is not violated near the solid boundary (Chen et al., 1996). Because the basic bounce-back boundary condition gives first order numerical accuracy, many other improved bounce-back method have been proposed. Among which the mid-way bounce back (Succi, 2001) method has found wide application. For the mid-way bounce back, a fluid particle can go into the boundary site, reverse its velocity and stream back into the boundary fluid site all in one time step. (make picture and put here)

$$f_{\bar{\alpha}}(\mathbf{x}_b, t + \delta_t) = f'_{\alpha}(\mathbf{x}_b, t) \tag{2.44}$$

where $\boldsymbol{\xi}_{\bar{\alpha}} = -\boldsymbol{\xi}_{\alpha}$ is the reversed lattice velocity, f'_{α} is the distribution function leaving the boundary node $\mathbf{x}_b$ after collision at time t.

Several modifications of the bounce-back boundary condition have also been proposed to incorporate the effects of; moving boundaries (Ladd, 1994; Aidun et al. 1998), curved boundaries (Filippova and Hanel, 1998; Mei et al., 1999, Guo et al. 2002), and deformable membrane (Peskin, 1977)

2.4.2 Periodic Boundary Condition

The periodic boundary condition is a basic implementation of the open boundary condition. The basic idea is to map any outgoing particle to the incoming particle where there is mass and momentum continuity on the opposite boundaries. Therefore, all particles leaving the domain re-enters the domain from the opposite end. It is noteworthy, that periodic conditions cannot exist with a pressure gradient since a pressure gradient will require that different particle densities at either ends of the boundaries. The work around for this problem is to impose the constant pressure gradient by applying a body force after the collision process as shown

$$f'_{\alpha(inlet)} = f'_{\alpha(outlet)} - w_\alpha \frac{3}{c^2}\frac{dp}{dx}\boldsymbol{\xi}_\alpha \cdot \hat{\boldsymbol{x}} \tag{2.45}$$

where $\frac{dp}{dx}$ is the constant pressure gradient, $\hat{\boldsymbol{x}}$ is the unit vector in the $\boldsymbol{x}$ direction and $f'_{\alpha()}$ superscript denote the post-collision state.

2.4.3 Constant Pressure/Velocity

Often in several applications, the pressure gradient through a flow field may not be modelled with a constant body force. In such applications, the flow can be modeled with prescribed velocity or pressure at the boundary. In the case of a pressure boundary condition, a pressure gradient can be set between the inlet and outlet of the geometry. This can be achieved by setting the density at slightly different value between the two ends. Subsequently, an extrapolation scheme can be used to determine the unknown distribution functions at the boundary. A detailed description of this scheme can be found in (Chen et al., 1996). On the other hand, with the Dirichlet velocity boundary condition, the known distribution function and the specified value of the velocity on a straight wall can be used to determine the value of the density on the boundary nodes. Detailed theoretical analysis of this boundary condition for a straight wall can be found in (Latt and Chopard, 2008).

2.4.4 Numerical Implementation and Single Phase Validations

Lattice Boltzmann equation is usually implemented through a two-step approach. Namely,

The collision step:

$$f'_\alpha(\boldsymbol{x},\ t) = f_\alpha(\boldsymbol{x}, t) - \frac{1}{\tau}\left[f_\alpha(\boldsymbol{x}, t) - f_\alpha{}^{(eq)}(\boldsymbol{x}, t)\right] \tag{2.46}$$

Streaming step:

$$f_\alpha(\boldsymbol{x} + \boldsymbol{\xi}_\alpha \delta_t,\ t + \delta_t) = f'_\alpha(\boldsymbol{x},\ t) \tag{2.47}$$

where f'_α is the post-collision state of the distribution function.

To validate our custom code for single phase fluid, we simulated two benchmark cases:

(a) 3-D lid-driven cavity and compared our results with equivalent simulation in Ansys FLUENT.

(b) 3-D Poiseuille (pressure-driven and gravity-driven) and compared our result to the analytical solution.

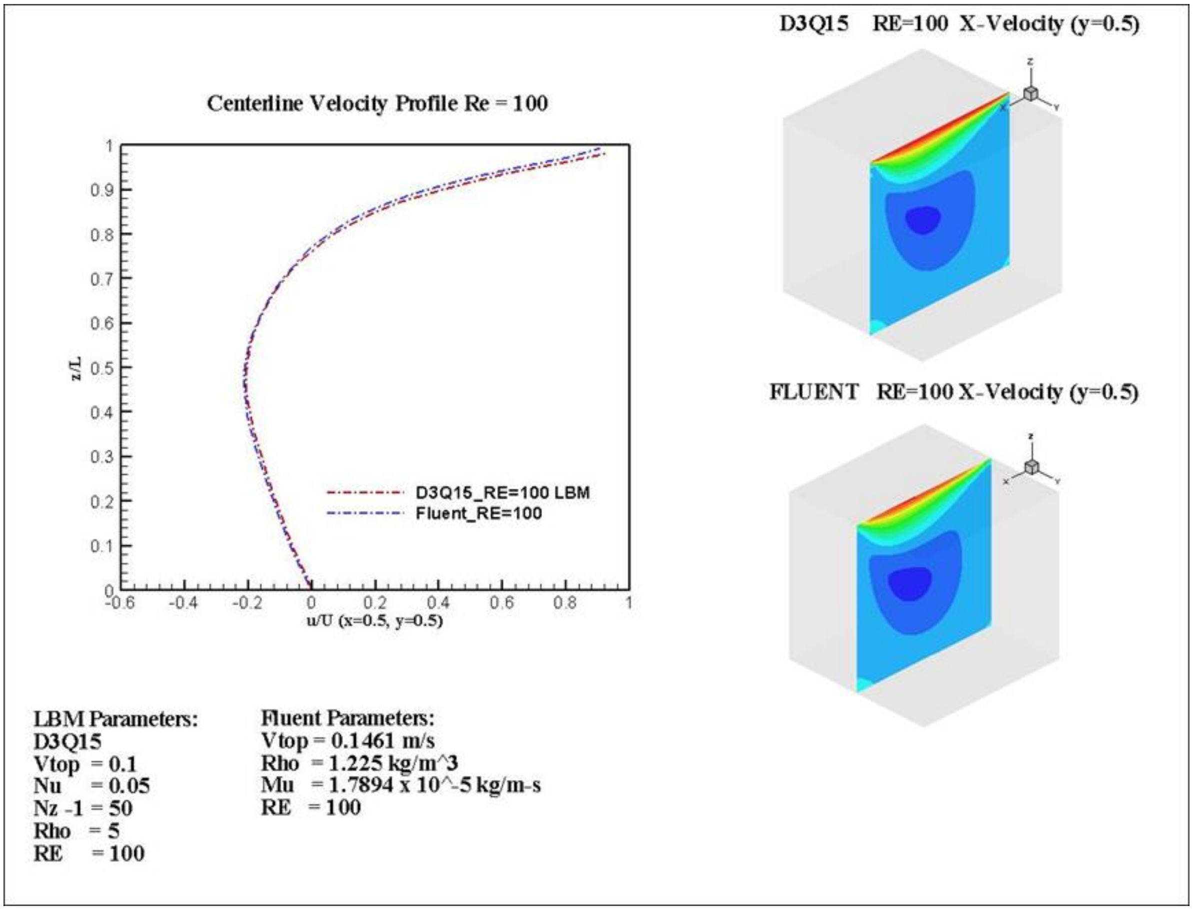

Centerline Velocity Profile Re = 100

D3Q15 RE=100 X-Velocity (y=0.5)

FLUENT RE=100 X-Velocity (y=0.5)

LBM Parameters:
D3Q15
Vtop = 0.1
Nu = 0.05
Nz -1 = 50
Rho = 5
RE = 100

Fluent Parameters:
Vtop = 0.1461 m/s
Rho = 1.225 kg/m^3
Mu = 1.7894 x 10^-5 kg/m-s
RE = 100

Fig. 2.1 Comparison of u_x using $51 \times 51 \times 51$ D3Q15 lattice with a Navier-Stokes solution from Ansys FLUENT for $\mathrm{Re} = 100$ in a lid-driven cavity flow. Note that simulation parameters are provided on figure.

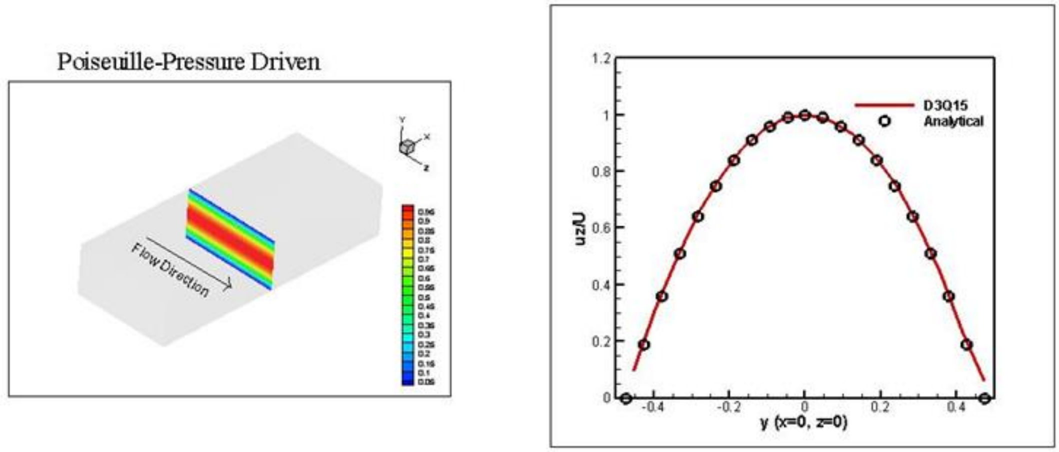

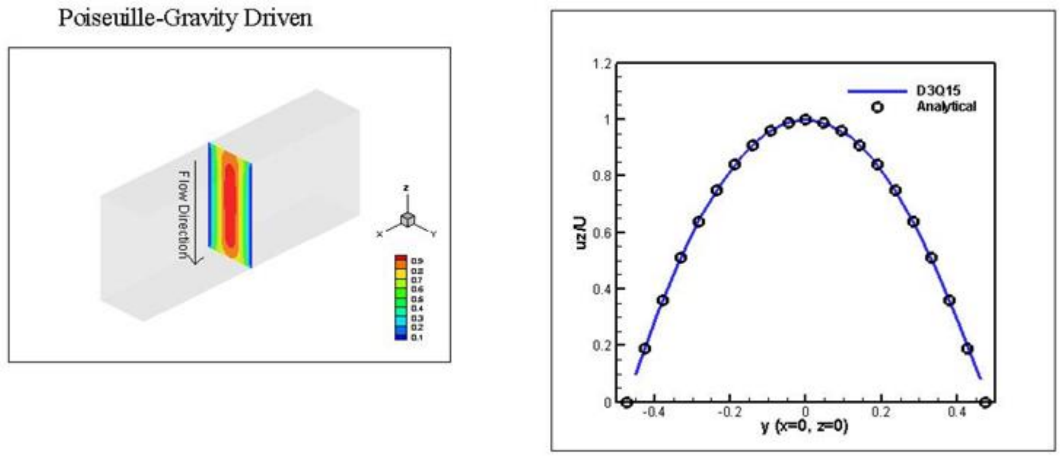

Fig. 2.2 LBM node-wise simulated velocities with the analytical Poiseuille velocity profile for gravity driven flow and pressure driven flow with mid-way bounce back (no slip) and periodic boundaries.

2.5 References

Aidun CK, Lu Y, Ding EJ (1998) Direct analysis of particulate suspensions with inertia using the discrete Boltzmann equation Journal of Fluid Mechanics 373:287-311 doi:10.1017/S0022112098002493

Ansumali S, Karlin IV (2002) Single relaxation time model for entropic lattice Boltzmann methods Physical Review E 65:056312

Bhatnagar PL, Gross EP, Krook M (1954) A Model for Collision Processes in Gases. I. Small Amplitude Processes in Charged and Neutral One-Component Systems Physical Review 94:511-525

Chapman, S., Cowling, T.G., (1970) The Mathematical Theory of Non-Uniform Gases. Cambridge University Press

Chen S, Martínez D, Mei R (1996) On boundary conditions in lattice Boltzmann methods Physics of Fluids 8:2527-2536 doi:10.1063/1.869035

Chikatamarla SS, Ansumali S, Karlin IV (2006) Entropic Lattice Boltzmann Models for Hydrodynamics in Three Dimensions Physical Review Letters 97:010201

Chikatamarla SS, Karlin IV (2009) Lattices for the lattice Boltzmann method Physical Review E 79:046701

Filipovic N, Ivanovic M, Kojic M (2009) A comparative numerical study between dissipative particle dynamics and smoothed particle hydrodynamics when applied to simple unsteady flows in microfluidics Microfluidics and Nanofluidics 7:227-235 doi:10.1007/s10404-008-0379-0

Frisch U, Hasslacher B, Pomeau Y (1986) Lattice-Gas Automata for the Navier-Stokes Equation Physical Review Letters 56:1505-1508

Gambosi TI (1994) Kinetic theory of gases Cambridge atmospheric and space science series

Grad H (1949) On the kinetic theory of rarefied gases Communications on Pure and Applied Mathematics 2:331-407 doi:10.1002/cpa.3160020403

Guo Z, Zheng C, Shi B (2002) Discrete lattice effects on the forcing term in the lattice Boltzmann method Physical Review E 65:046308

He X, Luo L-S (1997) A priori derivation of the lattice Boltzmann equation Physical Review E 55:R6333-R6336

He X, Zou Q, Luo L-S, Dembo M (1997) Analytic solutions of simple flows and analysis of nonslip boundary conditions for the lattice Boltzmann BGK model Journal of Statistical Physics 87:115-136 doi:10.1007/BF02181482

Huang, K., (1963) Statistical Mechanics. John Wiley & Sons, Inc

Karlin IV, Ferrante A, Öttinger HC (1999) Perfect entropy functions of the Lattice Boltzmann method EPL (Europhysics Letters) 47:182

Koga, T., (1970) Introduction to Kinetic Theory Stochastic Processes in Gaseous Systems. Pergamon Press.

Ladd A (1994a) Numerical simulations of particulate suspensions via a discretized Boltzmann-equation. 2. Numerical results. J Fluid Mech 271:311–339

Lallemand P, Luo L-S (2000) Theory of the lattice Boltzmann method: Dispersion, dissipation, isotropy, Galilean invariance, and stability Physical Review E 61:6546-6562

Latt J, Chopard B, Malaspinas O, Deville M, Michler A (2008) Straight velocity boundaries in the lattice Boltzmann method Physical Review E 77:056703

Liboff, R.L., (1969) Introduction to the Theory of Kinetic Equations. John Wiley & Sons, Inc.

Maier RS, Bernard RS, W. GD (1996) Boundary conditions for the lattice Boltzmann method Physics of Fluids 8:1788-1801 doi:10.1063/1.868961

McNamara GR, Zanetti G (1988) Use of the Boltzmann Equation to Simulate Lattice-Gas Automata Physical Review Letters 61:2332-2335

Mei R, Luo L-S, Shyy W (1999) An Accurate Curved Boundary Treatment in the Lattice Boltzmann Method Journal of Computational Physics 155:307-330 doi:http://dx.doi.org/10.1006/jcph.1999.6334

Nourgaliev RR, Dinh TN, Theofanous TG, Joseph D (2003) The lattice Boltzmann equation method: theoretical interpretation, numerics and implications International Journal of Multiphase Flow 29:117-169 doi:http://doi.org/10.1016/S0301-9322(02)00108-8

Peskin CS (1977) Numerical analysis of blood flow in the heart Journal of Computational Physics 25:220-252 doi:http://dx.doi.org/10.1016/0021-9991(77)90100-0

Shan X (2006) Analysis and reduction of the spurious current in a class of multiphase lattice Boltzmann models Physical Review E 73:047701

Wolfram S (1986) Cellular automaton fluids 1: Basic theory Journal of Statistical Physics 45:471-526 doi:10.1007/BF01021083

Zhang J (2011) Lattice Boltzmann method for microfluidics: models and applications Microfluidics and Nanofluidics 10:1-28 doi:10.1007/s10404-010-0624-1

3. CHAPTER THREE: MULTIPHASE LATTICE BOLTZMANN METHOD

It has been argued that for modeling interfacial phenomena, the LBE method has potential to be superior compared to other traditional-CFD methods (Shan and Chen, 1993, 1994; Shan and Doolen, 1995; Swift et al., 1995, 1996; Wagner and Yeomans, 1997). This is mainly because LBE methods are developed based on microscopic description of the fluids. As such, by dealing with the underlying microphysics it is convenient to incorporate intermolecular interactions which are the physical origin of the interface phenomena (Sehgal et al, 1999). Different multiphase LBE models have been successfully used to study numerous complex flow systems. An important step in developing these multiphase LBE models is the method through which the interaction between the particles of the different phases are incorporated into the evolution equation of the particle distribution function.

Over the years, several multiphase models have been proposed. Firstly, the Gunstensen method, based on the Rothman-Keller lattice gas model that uses a color gradient (two kind of colored particles are introduced for the two phases) to separate and model the interaction at the interface (Gunstensen et al., 1991; Rothman, 1988; Grunau et al., 1993). Secondly, the Shan and Chen method in which the interaction between the different particles of the different phases (components) are included into the kinetic equation via effective two-body pseudo-potential (Shan and Chen, 1993; Shan and Doolen, 1995). Thirdly, is the free energy based model in which the equilibrium properties of the model are constructed to be consistent with an underlying free energy functional, embedding both the hard-core effects and the weak interacting tail (Swift et al., 1995; 1996). In addition, there are other multiphase LBE models such as the finite-density model by He, Chen and Zhang (He et al., 1999) which is a significant modification of the Shan and Chen model.

For well-separated phases, the single-component multiphase (SCMP) model can be used. We provide more detailed description and analysis of the SCMP in latter chapters. In preparation for our study in the next chapter, we briefly describe the BGK-multicomponent multiphase (BGK-MCMP) approach using the Shan and Chen method to incorporate the interaction among constituent molecules in the next section. We refer the reader to (Chen et al., 2014) for a detailed description of this method.

3.1 Pseudopotential Multiphase Multicomponent LBE Method

In the BGK-MCMP pseudo-potential (Shan and Chen) model, each fluid component is represented by its own particle distribution function. These distribution functions follow the evolution equation

$$\begin{aligned} f_\alpha^\sigma(\mathbf{x}+\boldsymbol{\xi}_\alpha \Delta t, t+\ \Delta t) - \ f_\alpha^\sigma(\mathbf{x},t) \\ = -\frac{\delta_t}{\tau_\sigma}\left[f_\alpha^\sigma(\mathbf{x},t) - f_\alpha^{\sigma,(eq)}(\mathbf{x},t)\right] \end{aligned} \tag{3.1}$$

where $(\mathbf{x},t)$ is the lattice (two- or three- dimensional) configuration space. For convenience, the time step in the numerical scheme is set as $\delta_t = 1$. The discrete set of velocities $(\boldsymbol{\xi}_\alpha, \alpha = 0, \dots, N)$ are such that $\Delta\mathbf{x}_{\boldsymbol{\alpha}} = \boldsymbol{\xi}_\alpha \delta_t$. Also, $f_\alpha^{\sigma,(eq)}$ and f_α^σ are the Maxwell-Boltzmann distribution function and density distribution function of the σ^{th} component along the α^{th} velocity direction respectively. τ_σ is a non-dimensional lattice relaxation time that fixes the kinematic viscosity $\nu_\sigma = c_s^2\left(\tau_\sigma - \frac{1}{2}\right)$ where $c_s^2 = {}^{c}/_{\sqrt{3}}$ in the present work with $c = \frac{\delta_t}{\delta_x}$. The total body force acting on a fluid particle in multiphase fluid is given by

$$\mathbf{F}^{\sigma} = \mathbf{F}^{\sigma}{}_{\boldsymbol{ext}} + \mathbf{F}^{\sigma}{}_{\boldsymbol{int}} \tag{3.2}$$

where $\mathbf{F}^{\sigma}{}_{\boldsymbol{ext}}$ is the external body force, for example, gravity and pressure gradient. $\mathbf{F}^{\sigma}{}_{\boldsymbol{int}}$ is the self-consistently generated mean field intermolecular force between particles that provides non-local interaction between fluid components at each cell as a function of neighboring cell properties (Shand and Chen, 1993). For this interaction force, the separation of the fluid phases or components is automatic. The interaction force can be further subdivided into $\mathbf{F}^{\sigma}{}_{\boldsymbol{int}} = \mathbf{F}^{\sigma}{}_{f-f} + \mathbf{F}^{\sigma}{}_{f-s}$ (Fig. 3.1) where $\mathbf{F}^{\sigma}{}_{f-f}$ is the fluid-fluid interaction force and $\mathbf{F}^{\sigma}{}_{f-s}$ is the fluid-solid interaction force (further details provided in section 3.2)

The fluid-fluid interaction force (Shan and Chen, 1993) is given as

$$\boldsymbol{F}^{\sigma}_{f-f} = -\psi^{\sigma}(\mathbf{x}, t) \sum_{\sigma'=1}^{N} G^{\sigma\sigma'} \sum_{\alpha=1}^{N} w_{\alpha} \psi^{\sigma'} (\mathbf{x} + \boldsymbol{\xi}_{\alpha} \boldsymbol{\Delta} t, t) \boldsymbol{\xi}_{\alpha} \tag{3.3}$$

where $\psi^{\sigma}(\mathbf{x}, t)$ is the effective mass (pseudo-potential) and it is a function of the local density ρ_{σ} . The non-ideal behavior of the fluids is introduced via $\psi^{\sigma}(\mathbf{x}, t)$ and different choices of the effective mass yields different forms of equation of states (Yuan and Shaefer, 2006). $G^{\sigma\sigma'}$ is a coupling constant that is set to positive to mimic a cohesive force and the strength of the cohesive force is determined by the magnitude of $G^{\sigma\sigma'}$. Considering that the right-hand-side (RHS) of Eq. (3.3) above is a finite difference representation of $-\psi\nabla\psi$, with the right choice of normalization weight w_{α}, any number of neighbors can be included to obtain higher degree of isotropy (Sbragaglia et al., 2007; Shan 2006).

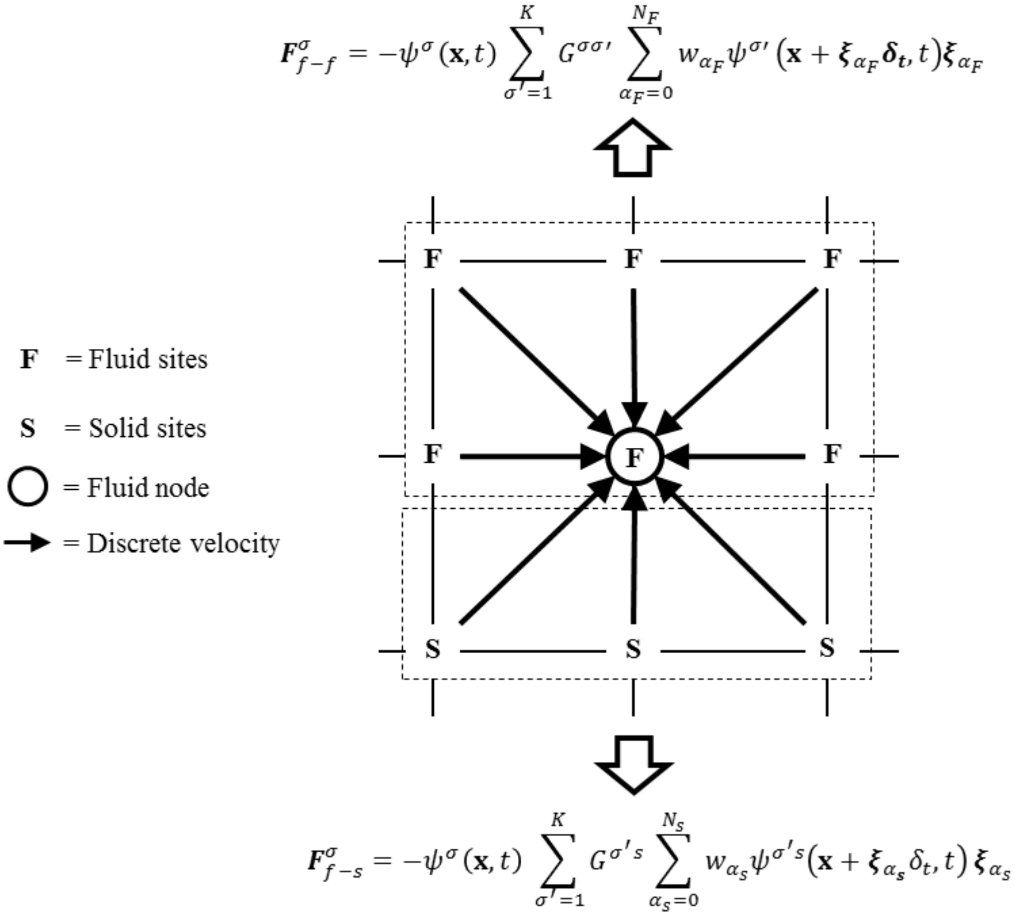

Fig. 3.1 Schematic of net interaction force on a fluid node near solid nodes

How to incorporate the total force into the pseudo-potential MPMC model is an important issue in the numerical stability and accuracy of the model. Different forcing schemes have been developed and evaluated (Guo et al., 2002; kupershtokh et al., 2009). In chapter 5, we will provide more details on these forcing schemes. In our study in the next chapter, the dynamic effect of the body force is incorporated into the evolution Eq. (3.1) by modifying the momentum values in the Maxwell-Boltzmann distribution $f_{\alpha}^{\sigma,(eq)}$

via the original Shan and Chen velocity shift force scheme (Shan and Chen, 1993). A brief description is provided below.

The equilibrium distribution function is given as

$$f_\alpha^{\sigma,(eq)} = w_\alpha \rho_\sigma \left(1 + \frac{\boldsymbol{\xi}_\alpha \mathbf{u}_\sigma^{eq}}{c_s^2} + \frac{\left(\boldsymbol{\xi}_\alpha \mathbf{u}_\sigma^{eq}\right)^2}{2c_s^4} - \frac{u_\sigma^{eq^2}}{2c_s^2} \right) \tag{3.4}$$

For the velocity shift method, the interaction force in incorporated into the model by shifting the velocity $\mathbf{u}_\sigma^{eq}$ in the equilibrium distribution function as shown below.

$$\mathbf{u}_\sigma^{eq}(\mathbf{x},t) = \mathbf{u}'_\sigma(\mathbf{x},t) + \frac{\tau_\sigma \mathbf{F}^\sigma(\mathbf{x},t)}{\rho_\sigma(\mathbf{x},t)} \tag{3.5}$$

$\mathbf{u}'_\sigma$, the composite macroscopic fluid velocity is defined as

$$\mathbf{u}'_\sigma(\mathbf{x},t) = \frac{\sum_\sigma \left(\sum_{\alpha=1}^{N} \frac{f_\alpha^\sigma \boldsymbol{\xi}_\alpha}{\tau_\sigma} \right)}{\sum_\sigma \frac{\rho_\sigma}{\tau_\sigma}} \tag{3.6}$$

Note that this velocity is different from the macroscopic uncoupled velocity of the individual components given in Eqs. (3.8) and (3.9).

The bulk macroscopic velocity can be obtained by averaging the momentum before and after collision and it is given by (Pan et al., 2004)

$$\rho\mathbf{u}(\mathbf{x},t) = \sum_\sigma \sum_{\alpha=1}^{N} f_\alpha^\sigma \boldsymbol{\xi}_\alpha + \frac{1}{2} \sum_\sigma \mathbf{F}^\sigma(\mathbf{x},t) \tag{3.7}$$

where $\rho = \sum_\sigma \rho_\sigma$ is the total density of the fluid.

The fluid mass density and momentum density for each component can now be obtained by

$$\rho_\sigma = \sum_{\alpha=1}^{N} f_\alpha^\sigma \tag{3.8}$$

$$\rho_\sigma \mathbf{u}_\sigma = \sum_{i=1}^{N} f_\alpha^\sigma \boldsymbol{\xi}_\alpha \tag{3.9}$$

In this chapter, we introduced the Shan and Chen (1993) method for the modeling of multiphase and multicomponent flows. This approach is based on phenomenological models of interface dynamics. This method introduces the intermolecular forces directly at the discrete lattice level among the constituent particles and are suitable for isothermal multicomponent flows. An important improvement, is the free-energy approach (Swift et al. 1995; 1996). In this model, the collisional properties of the model have been chosen in such a way that the equilibrium distribution is consistent with thermodynamics. In this study, we focus on the pseudo-potential based multiphase models and the recent improvements.

3.2 References

Chen L, Kang Q, Mu Y, He Y-L, Tao W-Q (2014) A critical review of the pseudopotential multiphase lattice Boltzmann model: Methods and applications International Journal of Heat and Mass Transfer 76:210-236 doi:http://dx.doi.org/10.1016/j.ijheatmasstransfer.2014.04.032

Grunau D, Chen S, Eggert K (1993) A lattice Boltzmann model for multiphase fluid flows Physics of Fluids A 5:2557-2562 doi:doi:http://dx.doi.org/10.1063/1.858769

Gunstensen AK, Rothman DH, Zaleski S, Zanetti G (1991) Lattice Boltzmann model of immiscible fluids Physical Review A 43:4320-4327

Guo Z, Zheng C, Shi B (2002) Discrete lattice effects on the forcing term in the lattice Boltzmann method Physical Review E 65:046308

He X, Chen S, Zhang R (1999) A Lattice Boltzmann Scheme for Incompressible Multiphase Flow and Its Application in Simulation of Rayleigh–Taylor Instability Journal of Computational Physics 152:642-663 doi:http://dx.doi.org/10.1006/jcph.1999.6257

Kupershtokh AL, Medvedev DA, Karpov DI (2009) On equations of state in a lattice Boltzmann method Computers & Mathematics with Applications 58:965-974 doi:http://dx.doi.org/10.1016/j.camwa.2009.02.024

Pan C, Hilpert M, Miller CT (2004) Lattice-Boltzmann simulation of two-phase flow in porous media Water Resources Research 40:n/a-n/a doi:10.1029/2003WR002120

Rothman DH (1988) Cellular-automaton fluids; a model for flow in porous media Geophysics 53:509-518

Sbragaglia M, Benzi R, Biferale L, Succi S, Sugiyama K, Toschi F (2007) Generalized lattice Boltzmann method with multirange pseudopotential Physical Review E 75:026702

Sehgal BR, Nourgaliev RR, Dinh TN (1999) Numerical simulation of droplet deformation and break-up by Lattice-Boltzmann method Progress in Nuclear Energy 34:471-488 doi:http://dx.doi.org/10.1016/S0149-1970(98)00025-0

Shan X (2006) Analysis and reduction of the spurious current in a class of multiphase lattice Boltzmann models Physical Review E 73:047701

Shan X, Chen H (1993) Lattice Boltzmann model for simulating flows with multiple phases and components Physical Review E 47:1815-1819

Shan X, Chen H (1994) Simulation of nonideal gases and liquid-gas phase transitions by the lattice Boltzmann equation Physical Review E 49:2941-2948

Shan X, Doolen G (1995) Multicomponent lattice-Boltzmann model with interparticle interaction Journal of Statistical Physics 81:379-393 doi:10.1007/BF02179985

Swift MR, Orlandini E, Osborn WR, Yeomans JM (1996) Lattice Boltzmann simulations of liquid-gas and binary fluid systems Physical Review E 54:5041-5052

Swift MR, Osborn WR, Yeomans JM (1995) Lattice Boltzmann Simulation of Nonideal Fluids Physical Review Letters 75:830-833

Wagner AJ, Yeomans JM (1997) Effect of Shear on Droplets in a Binary Mixture International Journal of Modern Physics C 08:773-782 doi:10.1142/S0129183197000667

Yuan P, Schaefer L (2006) Equations of state in a lattice Boltzmann model Physics of Fluids 18:042101 doi:doi:http://dx.doi.org/10.1063/1.2187070

4. CHAPTER FOUR: EVALUATION OF DIFFERENT PSEUDOPOTENTIAL-BASED MULTICOMPONENT MULTIPHASE LATTICE BOLTZMANN WETTING MODELS FOR DROPLET-BASED SYSTEMS

4.1 Abstract

As direct numerical solutions, have become increasingly important in the design and optimization of droplet-based microfluidics applications, multicomponent and multiphase pseudo-potential lattice Boltzmann equation (LBE) method continues to gain much success, specifically in problems that involves fluid-solid interactions and complex geometries. Recently, some improvements have been made to the initial pseudo-potential based wetting model, which does not use a virtual fluid on solid nodes, to address the unphysical density variation near solid substrate by introducing a virtual fluid on the solid nodes. In this work, we investigated the effect of this density variation on the dynamics of a droplet by evaluating the three different pseudo-potential based wetting models against two test droplet flow systems. Our results show that the choice of wetting model affects the dynamics of the droplet. This effect is more pronounced in the non-wetting droplet attached to a solid surface or a wetting droplet in a non-wetting carrier fluid interacting with a solid surface. Especially, we discovered that the model that does not implement a virtual fluid on the solid node performed poorly.

4.2 Introduction

Next to a solid phase, the interaction force needs to be modified to account for the fluid-solid interaction. This modification is subsequently used to tune the contact angle of the fluids at the fluid-solid interface with the aim of obtaining different wetting conditions. Thus, different MCMP pseudo-potential-based wetting (PPBW) models have been developed. The two most popular approaches are the model that does not employ a virtual fluid on the solid nodes but tunes the fluid-solid interaction strength (Marty and Chen, 1996) and the models that employ a virtual fluid on the solid nodes and tunes the contact angles with the density of the virtual fluid (Sbragaglia et al., 2006; Benzi et al., 2006; Jansen and Harting, 2011).

It is noteworthy, that the pseudo-potential method is not strictly immiscible (Hou et al. 1997). For example, a small amount of the second fluid component (dissolved fluid component) is present in the first fluid component (main fluid component). This slight mixing has been reported to produce a local density variation near the solid phase (LBM is slightly compressible) and in turn affect the simulated fluid dynamics near the contact line. Hence, the different MCMP pseudo-potential-based wetting models may behave differently (Chen et al., 2015). Therefore, a side-by-side comparison of these different models is necessary.

In this section, we evaluated the performance of different PPBW models against the following systems: migration of a droplet placed on a vertical ideal wall under the influence of gravity and deformation-breakup-coalesce of a droplet past obstacles under the influence of gravity.

4.3 Wetting Models

The fluid-solid interaction force can be computed by this general form (Marty and Chen, 1996)

$$\boldsymbol{F}_{f-s}^{\sigma} = -\psi^{\sigma}(\mathbf{x},t) \sum_{\sigma'=1}^{K} G^{\sigma' s} \sum_{i=\alpha}^{N} w_i \psi^{\sigma' s}(\mathbf{x}+\boldsymbol{\xi}_{\alpha}\boldsymbol{\Delta}t,t)\, s(\mathbf{x} + \boldsymbol{\xi}_{\alpha}\boldsymbol{\Delta}t,t)\boldsymbol{\xi}_{\alpha} \tag{4.1}$$

where $s(\mathbf{x}+\boldsymbol{\xi}_{\alpha}\boldsymbol{\Delta}t,t)$ is an indicator function that it set to 0 and 1 for a fluid node and a solid node respectively. $G^{\sigma s}$ (the interaction strength between a fluid node and a solid node) and $\psi^{\sigma s}({\rho^{s}}_{\sigma})$ are parameters in Eq. (4.1) that can be adjusted to obtain different wetting conditions. Here ${\rho^{s}}_{\sigma}$ is the fictitious density of the solid node. There are two most popular MCMP pseudo-potential based wettability approaches. The first approach involves setting $\psi^{\sigma s}({\rho^{s}}_{\sigma})$ as unity and adjusting $G^{\sigma s}$ to achieve a range of contact angles. For the second approach, $G^{\sigma s}$ is fixed ($G^{\sigma s} = G^{\sigma\sigma'} = G^{\sigma'\sigma}$) and ${\rho^{s}}_{\sigma}$ is tuned to obtain the desired contact angle (Sbragaglia et al., 2006; Benzi et al., 2006). The model proposed by Marty and Chen (1996) utilizes the first wetting approach while the models proposed by Jansen and Harting (2011), Yu Chen (2015) employs the second wetting approach. In what follows, we will provide a brief description of how these different models are implemented.

4.3.1 Marty and Chen (MC) Model

Marty and Chen model (MC model) is the first wetting model. It sets the effective mass on the solid nodes as unity (Fig. 4.1) and adjusts $G^{\sigma s}$ to introduce neutral or nonneutral wetting (Marty and Chen, 1996). Taking (Fig. 3.1 from chapter 3) as an example, the net fluid-fluid interaction on the boundary fluid nodes is given as

$$\boldsymbol{F}^{\sigma}_{f-f} = -\psi^{\sigma}(\mathbf{x},t)\sum_{\sigma'=1}^{N} G^{\sigma\sigma'}\sum_{\alpha_F=0}^{N_F} w_{\alpha_F}\psi^{\sigma'}\left(\mathbf{x}+\boldsymbol{\xi}_{\alpha_F}\boldsymbol{\Delta}t,t\right)\boldsymbol{\xi}_{\alpha_F} \tag{4.2}$$

where α_F are all lattice indices for which $\mathbf{x}+\boldsymbol{c}_{i_F}\boldsymbol{\Delta}t$ grid site is a fluid node and N_F is the number of these nodes. Such that,

$$\boldsymbol{F}^{\sigma}_{f-s} = -\psi^{\sigma}(\mathbf{x},t)\ \sum_{\sigma'=1}^{N} G^{\sigma's}\sum_{i_s=0}^{N_S} w_{\alpha_S}\,\boldsymbol{\xi}_{\alpha_S} \tag{4.3}$$

the net solid-fluid interaction force above is provided to balance the fluid-fluid interaction force on the boundary fluid node. Where α_S are all lattice indices for which $\mathbf{x}+\boldsymbol{\xi}_{\alpha_s}\boldsymbol{\Delta}t$ grid site is a solid node and N_S is the number of these grid sites. Resulting in the total interaction force on the fluid boundary node equal to

$$\begin{aligned}\mathbf{F}^{\sigma}{}_{\boldsymbol{int}} = -\psi^{\sigma}(\mathbf{x},t)\Bigg[&\sum_{\sigma'=1}^{N} G^{\sigma\sigma'}\sum_{\alpha_{NS}=0}^{N_{NS}} w_{\alpha_{NS}}\psi^{\sigma'}\left(\mathbf{x}+\boldsymbol{\xi}_{\alpha_{NS}}\boldsymbol{\Delta}t,t\right)\boldsymbol{\xi}_{\alpha_{NS}}\\ &+\sum_{\sigma'=1}^{N} G^{\sigma's}\sum_{\alpha_s=0}^{N_S} w_{i_s}\,\boldsymbol{\xi}_{\alpha_s}\Bigg]\end{aligned} \tag{4.4}$$

From Eq. (4.3), positive and negative values of $G^{\sigma s}$ results in wetting and non-wetting conditions on the solid phase respectively while $G^{\sigma s}=0$ leads to neutral wetting. Generally, the magnitude of the fluid-fluid interaction force is greater than the fluid-solid interaction force in simulations (Chen et al., 2015). Thus, a layer of increased density may form near the solid nodes. Jansen et al. (2011) demonstrated that this density variation may be significant for wetting fluid near the solid nodes.

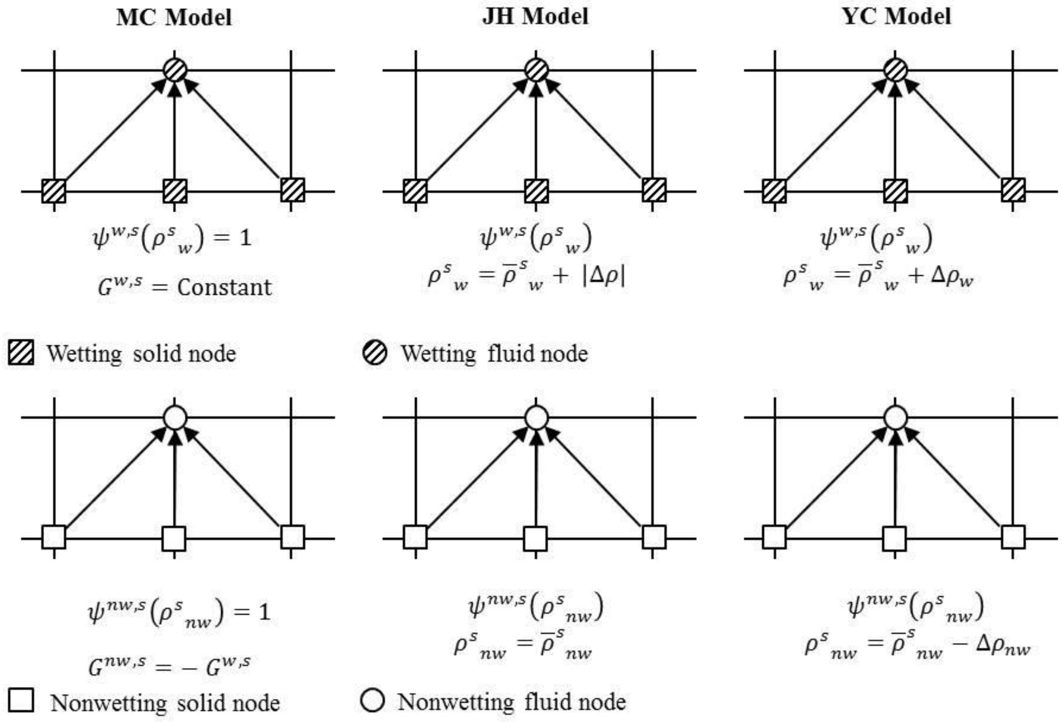

Fig. 4.1 Schematic illustrating the net fluid-solid interaction force for different wetting models while considering a hydrophilic wetting condition in a two-component multiphase system

4.3.2 Jansen and Harting (JH) Model

To alleviate the density variation in MC model, Jansen and Harting (2011) (JH model) proposed another wetting model that introduces a fictitious fluid on the solid boundary nodes. The density of the virtual fluid on a solid boundary node is approximated as the average fluid density of the surrounding fluid nodes. In this model, the net fluid-fluid interaction force on the fluid node next to the solid nodes is balanced by a similar fluid-fluid interaction force from the solid boundary node as shown in Fig. 4.1.

$$\mathbf{F}^{\sigma}{}_{int} = -\psi^{\sigma}(\mathbf{x},t)\left[\sum_{\sigma'=1}^{N} G^{\sigma\sigma'} \sum_{\alpha_F=0}^{N_F} w_{\alpha_F}\psi^{\sigma'}\left(\mathbf{x}+\boldsymbol{\xi}_{\alpha_F}\boldsymbol{\Delta}t,t\right)\boldsymbol{\xi}_{\alpha_F} + \sum_{\sigma'=1}^{N} G^{\sigma' s} \sum_{\alpha_S=0}^{N_S} w_{\alpha_S}\psi^{\sigma' s}\left(\rho^{s}{}_{\sigma'}\right)\boldsymbol{\xi}_{\alpha_S}\right] \tag{4.5}$$

Such that to obtain different wetting conditions the fictitious density on the solid node is increased by $|\Delta\rho|$ in the wetting component *(w)* and the non-wetting *(nw)* component left unmodified or vice versa. While for neutral wetting none of the components is modified.

$$\rho^{s}{}_{\sigma(w/nw)} = \overline{\rho}^{s}{}_{\sigma(w/nw)} + |\Delta\rho| \tag{4.6}$$

$$\rho^{s}{}_{\sigma(nw/w)} = \overline{\rho}^{s}{}_{\sigma(nw/w)} \tag{4.7}$$

where $\overline{\rho}^{s}{}_{\sigma} = \frac{1}{N_F}\sum_{\alpha_F=0}^{N_F}\rho_{\sigma}$ is the density of the fictitious fluid on the solid node.

For example, increasing the wetting component by an amount delta increases the repulsion between the wetting component (adjusted component) and the unmodified component, resulting in a hydrophilic condition. Whereas, increasing the non-wetting component results in a hydrophobic condition. It is noteworthy that the fictitious fluid is only used as a parameter to tune the net interaction force on the fluid node and does not take part in the LBM evolution equation (Sbgragaglia et al., 2006; Jansen and Harting, 2011). Although density variation still exists for this model because the addition of extra virtual fluid creates an imbalance of fluid-fluid interaction on the fluid boundary nodes, the magnitude of this density variation is small compared to the MC model. This density variation mainly appears on the non-wetting fluid region.

4.3.3 Yu Chen (Yu) Model

Following the JH model, Yu Chen (2015) (Yu model) recently proposed a modified wetting model that addressed the density variation in JH model. While this density variation cannot be eliminated, the YC model ensured equal level of density variation in both the non-wetting and wetting region of the domain. This was achieved by simultaneously increasing and decreasing, by equal amount, the fictitious fluid of the wetting and non-wetting component respectively.

$$\rho^{s}{}_{\sigma} = \overline{\rho}^{s}{}_{\sigma} + \Delta\rho_{\sigma} \tag{4.8}$$

This ensures that the fluid dynamics near the solid phase is not biased towards either component (Fig. 4.1). In Yu et al., (2015) the nonphysical effect produced by the density variation in this model was determined to be smaller than in the JH model.

4.4 Simulation Parameters

Since the focus of this study is to evaluate the different PPBW models, here we consider a two-component system (binary immiscible fluids) with identical viscosity $\left({}^{\nu_w}/{}_{\nu_{nw}} = 1\right)$ and density $\left({}^{\rho_w}/{}_{\rho_{nw}} = 1\right)$ for all cases. Therefore, viscosity and density ratio is equal to unity. For simplicity, the effective mass was chosen as $\psi^{\sigma}(\mathbf{x},t) = \rho_{\sigma}(\mathbf{x},t)$. Furthermore, we employed the three dimensional D3Q15 velocity model because it requires less memory. The weights are

$$w_i = \begin{cases} {}^{2}/{}_{9}, & i = 0 \\ {}^{1}/{}_{9}, & i = 1, \dots, 6, \\ {}^{1}/{}_{72}, & i = 7, \dots, 14 \end{cases} \tag{4.9}$$

and discrete velocities are defined as $\boldsymbol{\xi}_\alpha = c\boldsymbol{e}_\alpha$ with

$$[\boldsymbol{e}_0, \boldsymbol{e}_1, \boldsymbol{e}_2, \boldsymbol{e}_3, \boldsymbol{e}_4, \boldsymbol{e}_5, \boldsymbol{e}_6, \boldsymbol{e}_7, \boldsymbol{e}_8, \boldsymbol{e}_9, \boldsymbol{e}_{10}, \boldsymbol{e}_{11}, \boldsymbol{e}_{12}, \boldsymbol{e}_{13}, \boldsymbol{e}_{14}\ ]$$

$$= \begin{bmatrix} 0 & 1 & -1 & 0 & 0 & 0 & 0 & 1 & -1 & 1 & -1 & 1 & -1 & 1 & -1 \\ 0 & 0 & 0 & 1 & -1 & 0 & 0 & 1 & -1 & 1 & -1 & -1 & 1 & -1 & 1 \\ 0 & 0 & 0 & 0 & 0 & 1 & -1 & 1 & -1 & -1 & 1 & 1 & -1 & -1 & 1 \end{bmatrix} \tag{4.10}$$

From Eqs. (4.2) and (4.5), $G^{w,nw} = G^{nw,w} = G^{w,s} = G^{nw,s}$ given as (Pan et al., 2004)

$$G^{w,nw}(\mathbf{x}, \mathbf{x}') = \begin{cases} g, & \text{if } |\mathbf{x} - \mathbf{x}'| = 1 \\ g/\sqrt{3}, & \text{if } |\mathbf{x} - \mathbf{x}'| = \sqrt{3} \\ 0, & \text{otherwise} \end{cases} \tag{4.11}$$

g is the fluid-fluid interaction strength and from Eq. (4.5), $G^{ws} = -G^{nw,s}$ defined as (Pan et al., 2004)

$$G^{w,s}(\mathbf{x}, \mathbf{x}') = \begin{cases} g^{ws}, & \text{if } |\mathbf{x} - \mathbf{x}'| = 1 \\ g^{ws}/\sqrt{3}, & \text{if } |\mathbf{x} - \mathbf{x}'| = \sqrt{3} \\ 0, & \text{otherwise} \end{cases} \tag{4.12}$$

where g^{ws} is the fluid-solid interaction strength.

To determine the position of the interface we introduce an order parameter given by (Jansen and Harting, 2011)

$$\phi(\mathbf{x}, t) = \rho_w - \rho_{nw} \tag{4.13}$$

and we select the interface as the points where the order parameter is zero.

We set the fluid-fluid interaction coefficient $G^{w,nw} = G^{nw,w} = 0.001$ and obtained the surface tension $\sigma = 0.0067$. Also, for a quantitative comparison of these PPBW models, the wetting parameters in the models need to be tuned for identical contact angles. Therefore, we performed several preliminary simulations and provide the matching wetting parameters in Table 4.1.

	Contact Angle $\theta = 118^0$	Contact Angle $\theta = 78^0$	Contact Angle $\theta = 62^0$
Yu model	$G^{w,nw}\Delta\rho_w = -0.0146$ $G^{w,nw}\Delta\rho_{nw} = 0.0146$	$G^{w,nw}\Delta\rho_w = 0.0051$ $G^{w,nw}\Delta\rho_{nw} = -0.0051$	$G^{w,nw}\Delta\rho_w = 0.0146$ $G^{w,nw}\Delta\rho_{nw} = -0.0146$
JH model	$G^{w,nw}\Delta\rho_w = 0.0330$ $G^{w,nw}\Delta\rho_{nw} = 0$	$G^{w,nw}\Delta\rho_w = 0$ $G^{w,nw}\Delta\rho_{nw} = 0.0097$	$G^{w,nw}\Delta\rho_w = 0$ $G^{w,nw}\Delta\rho_{nw} = 0.0330$
MC model	$G^{w,nw}G^{w,s} = 1.5 \times 10^{-5}$ $G^{w,nw}G^{nw,s} = -1.5 \times 10^{-5}$	$G^{w,nw}G^{w,s} = -4.0 \times 10^{-6}$ $G^{w,nw}G^{nw,s} = 4.0 \times 10^{-6}$	$G^{w,nw}G^{w,s} = -1.5 \times 10^{-5}$ $G^{w,nw}G^{nw,s} = 1.5 \times 10^{-5}$

Table 4.1 Simulation parameters for all test cases.

4.5 Numerical Results and discussion

To evaluate the numerical performance of the different (PPBW) models described in the previous section, two numerical test cases were simulated. Namely, the dynamic behavior of a wetting and non-wetting droplets sliding down the bottom wall of a vertical duct under the influence of gravity and the deformation-breakup-coalesce of a wetting and non-wetting droplet past an octagonal and square bar obstacle under the influence of gravity.

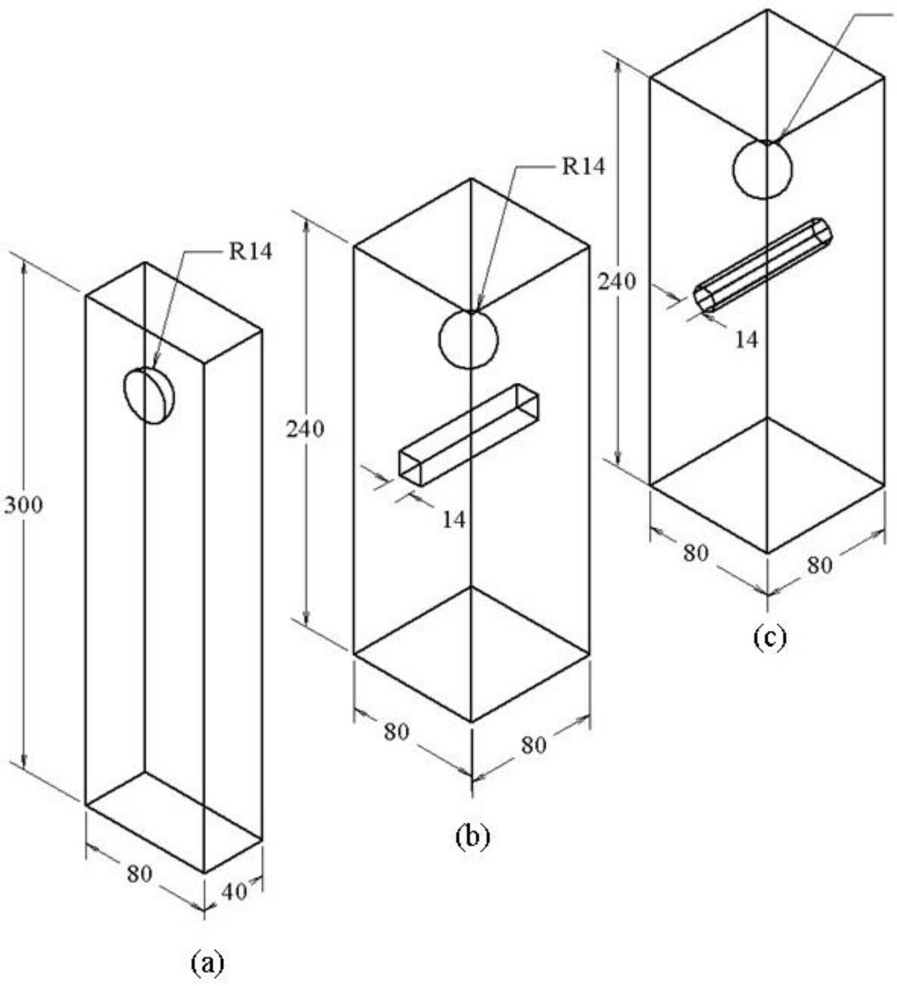

Fig. 4.2 Schematic illustration of the simulations geometries: (a) Sliding attached droplet (b) Square bar obstruction (c) Octagonal bar obstruction. All dimensions are in lattice unit.

4.5.1 Wetting and non-wetting droplet sliding on a vertical ideal wall under the influence of gravity

The first test case is a droplet (wetting or non-wetting) that is attached to the bottom ideal wall of a vertical duct and allowed to slide down the wall under the influence of gravity. The computational domain size is $40 \times 80 \times 300$ lattice units (Fig. 4.2) and $V/_{h^3} = 0.15$ as described in (Kang et al., 2005) where *h* is the height of the duct and *V* is the volume of the duct. Mid-way bounce back boundary condition was used on all walls and periodic boundary condition was used in the *z*- direction. Initially, the droplet was allowed to equilibrate and after 50 000 iteration a steady droplet was obtained. This lattice time was set as the initial time. Then, a constant body force was applied along the negative *z*-direction. The flow is characterized by the capillary number Ca which is defined as $Ca = {}^{\rho_{nw} g V}\!/_{\sigma h}$ (Kang et al., 2005) where ρ_{nw} is the density of the non-wetting fluid, g is the gravitational factor, V is the volume of the duct, h is the height of the duct and σ is the surface tension. During preliminary simulations, we varied the gravitational factor g to obtain different capillary number and determined that $Ca = 0.8$ is above the critical capillary number for the wetting and non-wetting droplet (data not shown). Therefore, in this test case we set $Ca = 0.8$ to capture the deformation and pinch-off of the droplet in the carrier fluid. The density variation on the boundary fluid node vanishes when the droplet has a neutral wettability (i.e. contact angle is 90^{o}) in the PPBW model that utilizes a virtual fluid on the solid nodes (Kang et al., 2005). Consequently, we simulated a sliding neutral wetting droplet with MC (MC ref) and JH models (ref.). In turn, we used the result as our reference solution to allow a quantitative comparison. Additionally, we simulated wetting and non-wetting droplets sliding for the three PPBW models and allowed the simulations to proceed until the droplet was about to re-enter the domain due to the periodic boundary condition along the *z*-direction. Afterwards, we inspected the results for similarities or differences and compared the solutions against the reference solutions. For the analysis of the results, we first measured the displacement *z* of the leading edge of the contact line from the top periodic boundary condition. The initial position at iteration time = 0 is z_o. Secondly, we measured the wetted length *l* by subtracting the displacement of the trailing edge of the contact line from its leading edge and normalized this value with the initial value l_o. Finally, we measured the wetted area A enclosed by the contact line. In a similar way, we normalized this value with the initial wetted area A_o.

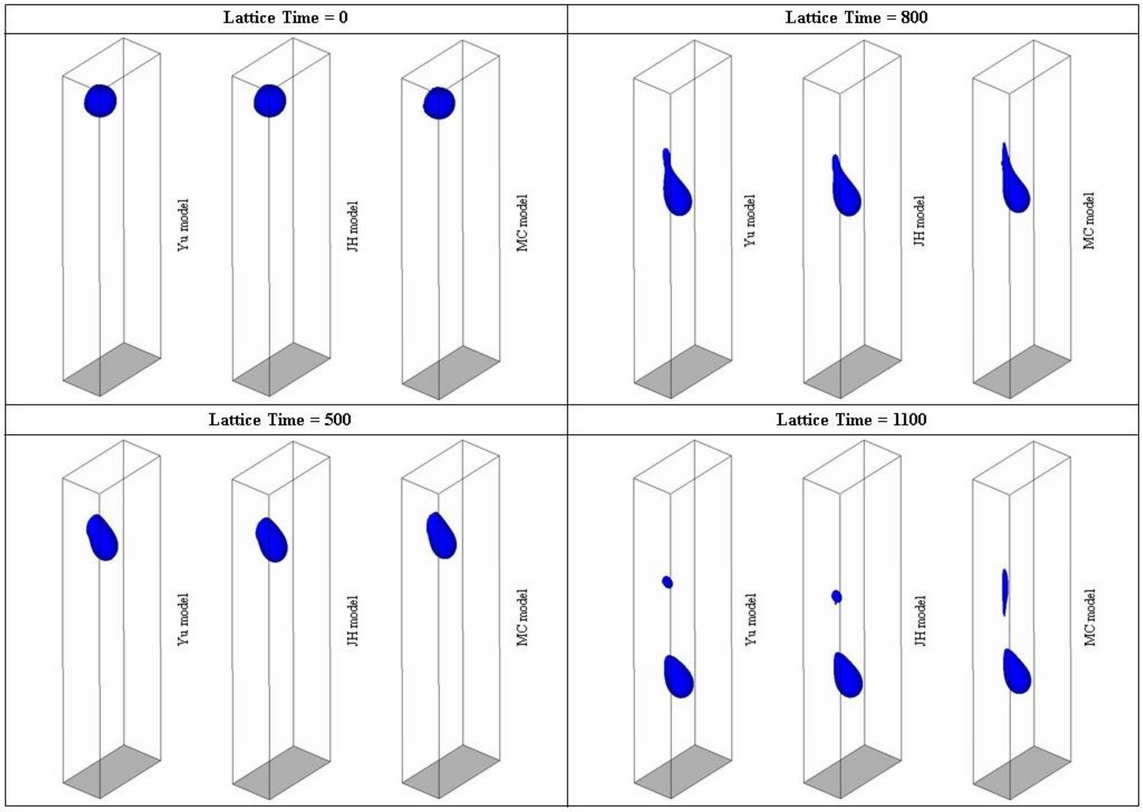

Fig. 4.3 Snapshots of a droplet on a hydrophobic wall ($\theta = 118^o$) with the different wetting schemes at different lattice times

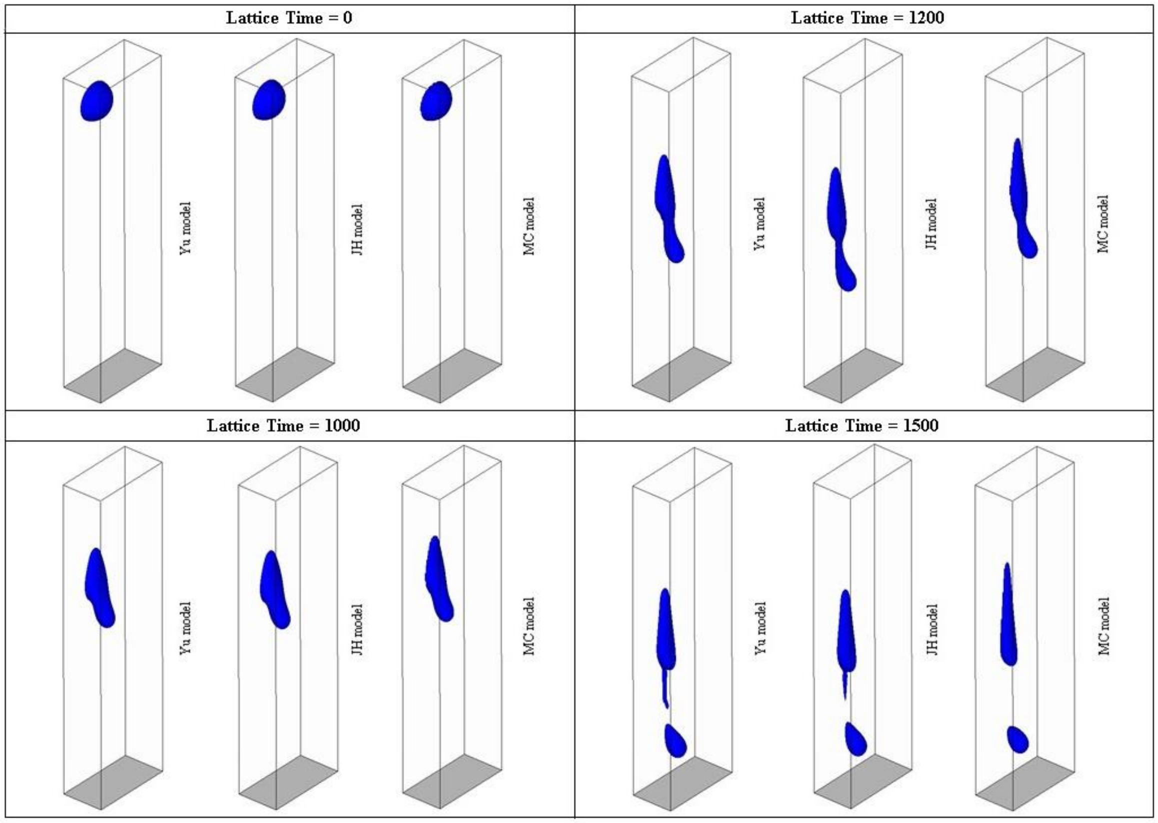

Fig. 4.4 Snapshots of the droplet on a hydrophilic wall ($\theta = 78^{\mathrm{o}}$) with the different wetting schemes at different lattice times.

Figure 4.3 shows snapshots of the dynamic behavior of the non-wetting. Here, we can see that the droplet experienced faster deformation in the JH and Yu model. This result in earlier pinch off of the portion of the droplet compared to the MC model. On the contrary, more wetting in general was observed in the MC model. Similarly, Figure 4.4 shows snapshots of the dynamic behavior of the wetting droplet. In this case, different from what we observed in Figure 4.3, we noticed a faster deformation and an earlier pinch off in the MC model.

Next we check the displacement of the neutral wetting droplet as it slides down the vertical wall for the MC (MC ref.) and JH (ref.) models. In Figure 4.5A and Figure 4.5B, we observe that the slip velocity of the contact line for the MC model is less than that of JH model for the neutral droplet. This suggests that the density variation that is present in MC ref. simulation tends to produce increased (unphysical) wetting (Fig. 4.5B) resulting in reduced slip velocity. For the non-wetting droplet (Fig. 4.5A), very little increase in the slip velocity was observed in MC model when compared to the reference (ref. on figure) model. In contrast, JH and Yu models produced a much greater increase in slip velocity as it is to be expected in a non-wetting droplet. As reported in Chen et al. (2015) for the non-wetting fluid, little variation in density of the dissolved component (wetting) was produced for both JH and Yu models while the density variation in the main component (non-wetting) for JH model is greater than in Yu model. This explains why the observed slip velocity in the JH model is greater than in Yu model.

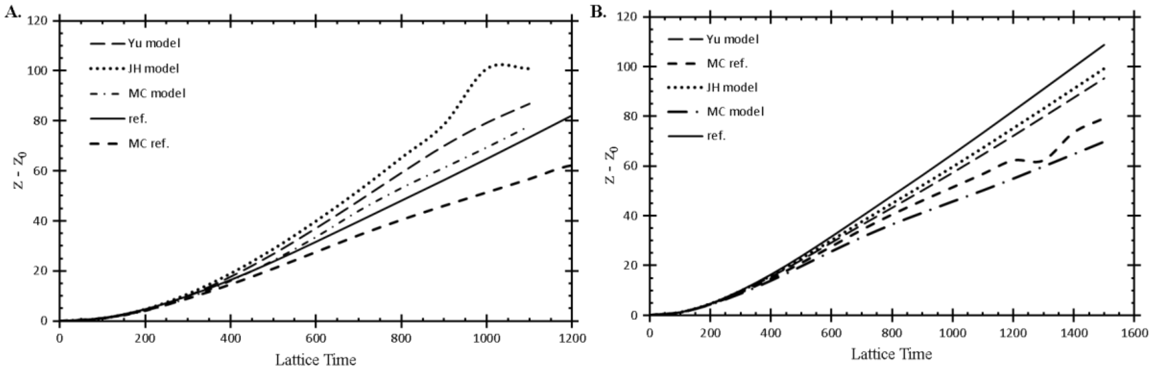

Fig. 4.5 Time history of the displacement of the sliding droplet from initial position. A. Non-wetting droplet ($\theta = 118^{\mathrm{o}}$) B. Wetting droplet ($\theta = 78^{\mathrm{o}}$).

In the case of a wetting droplet (Fig. 4.5B), we observed that the slip velocity of the contact line in JH and Yu models are less than in the reference case. Similarly, the contact line velocity in MC model is also less than that of MC reference. This is consistent with a wetting droplet because the velocity is reduced as a result of the wetting. Interestingly, the contact line slip velocities observed in JH and Yu model is still greater than that of the neutral droplet in the MC model.

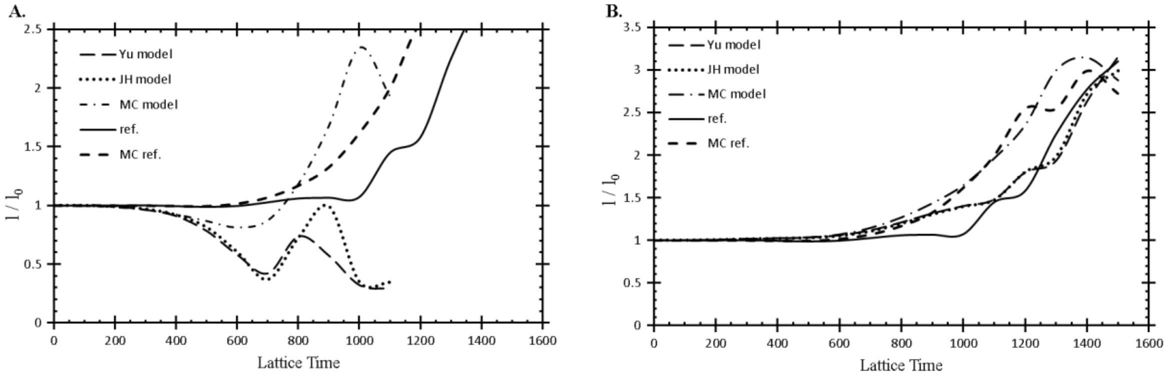

Fig. 4.6 Time history of the normalized wetted length of the sliding droplet. A. Non-wetting droplet ($\theta = 118^{o}$) B. Wetting droplet ($\theta = 78^{o}$).

Figures 4.6A and 4.6B show the normalized wetted length for the wetting and non-wetting droplets. We observe that in general it takes a longer time before the differences in the normalized wetted length for the three PPBW models begin to appear in the wetting droplet (lattice time = 700) compared to the non-wetting droplet (lattice time = 400). Consistent with our observations in the slip velocity, the neutral droplet in the reference MC model generates longer normalized wetted length compared to the reference JH model.

For the non-wetting droplet (Fig. 4.6A), we notice cycles of increase and decrease in the value of the normalized wetted length, suggesting that the motion of the contact line of the droplet involves a sequence of contracting (decrease in wetted length) and stretching (increase in wetted length) processes. The contact line initially contracts and then stretches, followed by another contraction just before a portion of the droplet pinches off. On the other hand, for the wetting droplet, the contact line stretches continuously for most the motion and a minute contraction was observed just before a portion of it pinches off (Fig. 4.6B). For the non-wetting droplet, the normalized wetted length in JH and Yu models vary similarly and its magnitude is below the JH model reference neutral droplet. On the contrary, pronounced stretching (stretching greater than as observed in a neutral droplet) was observed in the MC model when we compared it with both reference neutral droplets. We also notice that at iteration time = 800, while the Yu model was already contracting, JH model continued to stretch and did not begin contracting until iteration time = 900. Incidentally, the peak of this stretching for the JH model slightly corresponds to the sudden increase in the slip velocity observed in (Figure 4.5A).

In Figure 4.6B, for the wetting droplet, we observed identical profile for the normalized wetted length in both JH and Yu model. Although for most the flow the magnitude of the normalized wetted length for the JH and Yu model is greater than the JH model reference neutral droplet, at iteration time = 1250, the magnitude dropped below that of the neutral droplet and remained below for the droplet.

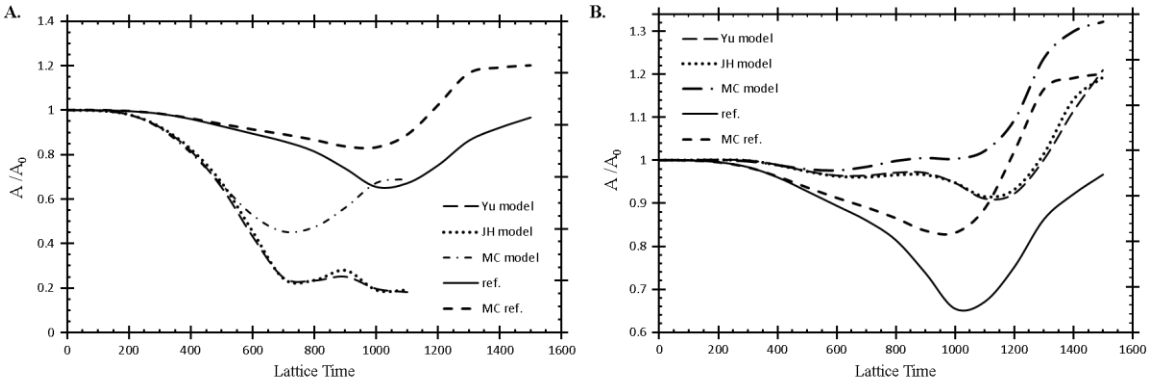

Fig. 4.7 Time history of the normalized wetted area of the sliding droplet. A. Non-wetting droplet ($\theta = 118^{o}$) B. Wetting droplet ($\theta = 78^{o}$).

Although we observed almost similar profile in the MC model, the magnitude did not drop below that of the neutral droplet for the duration of the flow. Also, as expected, MC model produced significantly increased wetted length when it was compared JH reference neutral wetting droplet.

We also compared the normalized wetted area. As shown in Figures 4.7A and 8B, the reference neutral droplet in MC model also generated more normalized wetted area when compared to the reference neutral droplet in JH model. For the non-wetting droplet, the magnitudes of the normalized wetted area in JH and Yu models are identical and below that of the neutral droplet throughout the flow duration while in the MC model an increase in this magnitude began to develop at iteration time = 700 and eventually exceeded the neutral wall at approximately iteration time = 1000. Also, the normalized wetted area in the MC model decreased at a slower rate than other two PPBW models. Furthermore, in Figure 4.7B we can see that for the wetting droplet, the magnitude of the normalized wetted area is greater than that of the neutral droplet in the three different PPBW models. Different from our observations in Figure 4.7A, MC model predicted a similar normalized wetted area profile to the other two PPBW models even though its magnitude is greater.

The above results demonstrate that the choice of PPBW models affects the flow physics. From the numerical formulation, fluid-fluid interaction and fluid-solid interaction forces for the MC model are in the same direction for either the wetting or the non-wetting droplet. This results in an increase in the density of the dissolved component on the fluid boundary node (Kang et al., 2005). This variation in the density of the dissolved component on the fluid boundary nodes will repel the main fluid. As a result, the density of the main fluid on the fluid boundary node is reduced (more reduction in non-wetting droplet). This explains the increased unphysical wetting observed in the non-wetting droplet evidenced by the reduced slip velocity, with greater magnitude in wetted length and wetted area. In JH model, this density variation is minimized by providing a virtual fluid on the solid boundary nodes to balance the fluid-fluid interaction force. Take the case of a non-wetting droplet as an example; this addition can minimize the increase in the density of the dissolved wetting component. Resulting in less unphysical wetting and increase in the slip velocity as observed in the results above. Like the JH model, Yu model also apply a virtual fluid on the solid boundary nodes. However, it minimizes density variations in both dissolved and main components through a counterbalance arrangement.

Summing up the above test case, we can see that while the results from JH model are very like that produced by Yu model. We discovered that the counterbalance in density variation implemented in Yu model could balance the slip velocity. In general, density variation on fluid boundary nodes produced unphysical wetting that reduces slip velocity which in turn produces earlier pinch off of the top of the droplet. This density variation effect was more pronounced in MC model.

4.5.2 Free droplet obstructed by octagonal and square bars

In the previous section, we evaluated the different PPBW models for attached non-wetting and wetting droplets. To further compare the different PPBW models, we consider a more complex problem that involves the interaction of a free wetting or non-wetting droplet with two differently shaped obstacles (square and octagonal prism). In our simulations, the computational domain size is $80 \times 80 \times 240$ lattice units and periodic boundary conditions were used on all boundaries. Initially, a droplet of diameter $D = 28$ lattice units was placed in the axis of the domain and allowed to equilibrate.

After which a square or octagonal prism was placed a distance from the droplet (Figure 3). The viscosity and density ratio are set as the previous case in section. The motion of the droplet is driven by gravity $= 2.0 \times 10^{-3}$.

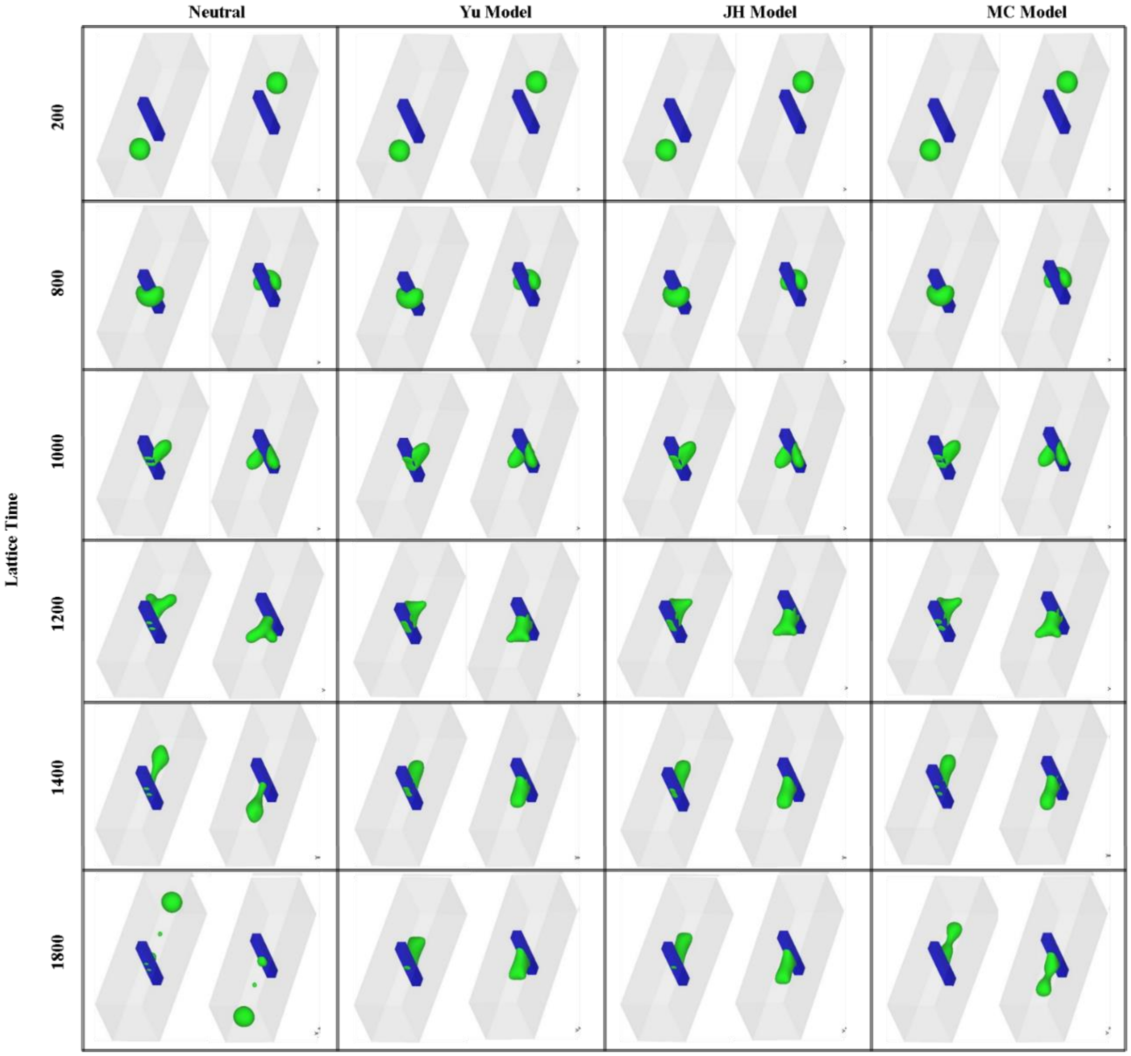

Fig. 4.8 Computed images (view from two opposing angles) of the impact of a wetting droplet ($\theta = 62^{\circ}$) onto a square obstacle at different lattice times for the different pseudo-potential based wetting models. Note that we included the image of a neutral droplet for reference.

Here we describe the dynamics of the droplet as it goes through a deformation, break up and coalescing processes. We also described the direction of the velocity vector field near the droplet and obstacle. To achieve this, we first created a YZ plane that represents the slice of the domain at position $x = 40$ lattice units and reported the interface evolution and the velocity vector field directions.

4.5.2.1 Wetting droplet in a non-wetting carrier fluid

In Figures 4.8 and 4.9, at iteration time = 800, the droplet begins to deform steadily as it encounters the obstacles and produces a concave meniscus around the obstacles. We observe a dead zone (layer of carrier fluid) enclosed between the valley of the meniscus and the upstream surface of the obstacles. This dead zone is shaped like a sliced sphere and we noticed that the diameter of the dead zone is generally greater in the square obstacle compared to the octagonal obstacle (Fig. 4.10). In addition, we notice for the square obstacle that in JH and Yu models the diameter of the dead zone is approximately equal and less than that in the MC model. For the octagonal obstruction, no difference was observed in the diameter of the dead zone between the different models.

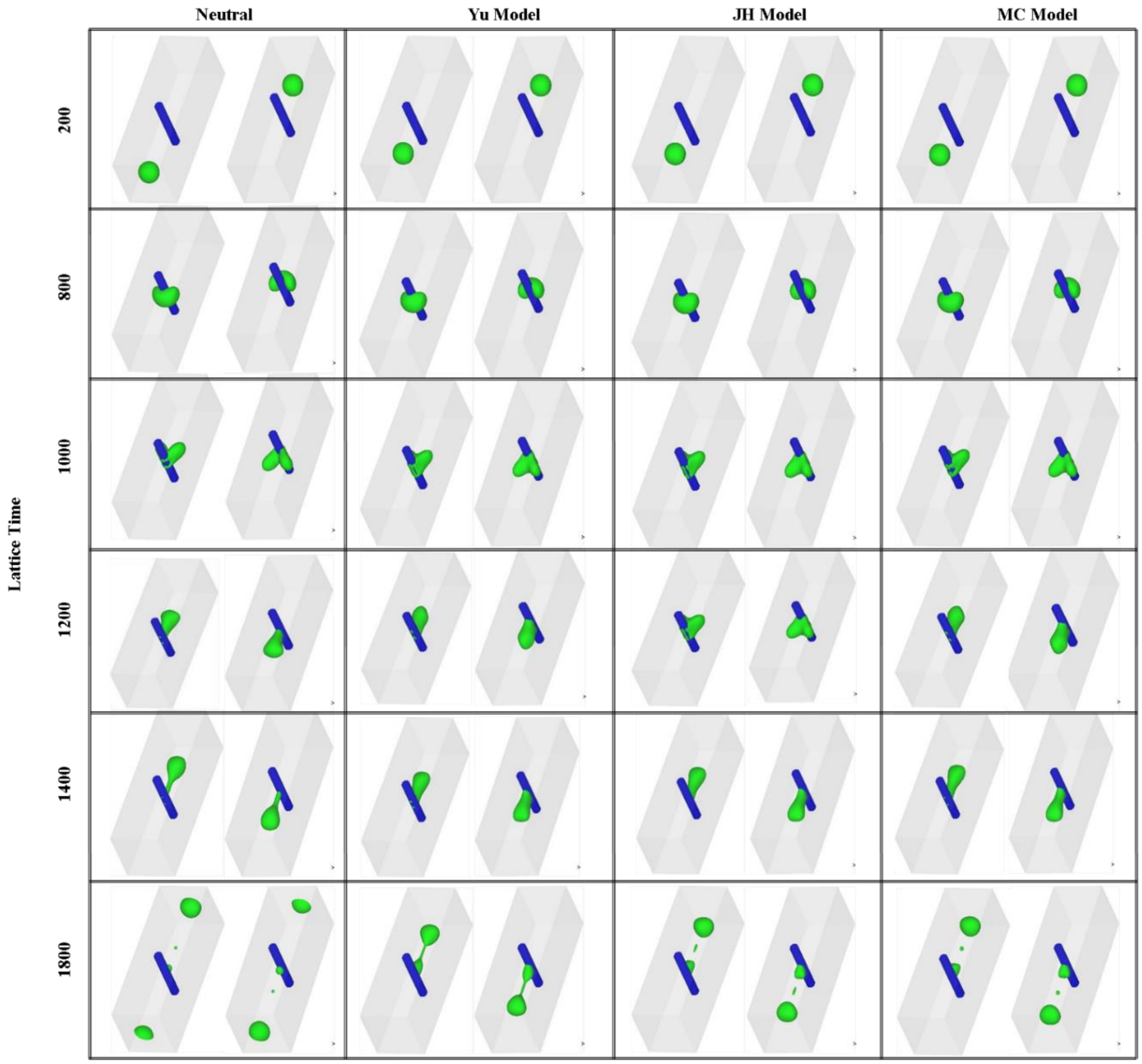

Fig. 4.9 Computed images (view from two opposing angles) of the impact of a wetting droplet ($\theta = 62^{o}$) onto an octagonal obstacle at different lattice times for the different pseudo-potential based wetting models. Note that we included the image of a neutral droplet for reference.

Fig. 4.10 Droplet dynamics as the wetting droplet ($\theta = 62^{o}$) impacts the obstacles for the different pseudo-potential based wetting models at lattice time = 800. The figure shows the interface profile and the velocity vector in the plane *x*=40. Arrows are included to show the general direction of the velocity vectors

We also observe more wetting by the two horns of the meniscus in the octagonal obstacle than that in the square obstacle (Fig. 4.10). While inspecting the velocity vector field in Figure 4.10, we noticed a recirculating region in the carrier fluid near the downstream surface of the square obstacle. Similar recirculating region was not observed in the downstream surface of the octagonal obstruction. Interestingly, we did not find any recirculating region inside the droplet as it interacts with the obstacles in Figure 4.10. We also observe an increase in the velocity near the downstream region of both horns of the meniscus and in the carrier fluid near this region. This increased velocity appears to pull

(Fig. 4.8 and 4.9) the meniscus around the obstacle which results in further deformation of the droplet.


MC Model

JH Model

Yu Model

Fig. 4.11 Droplet dynamics as the wetting droplet ($\theta = 62^{o}$) impacts the obstacles for the different pseudo-potential based wetting models at lattice time = 1000. The figure shows the interface profile and the velocity vector in the plane *x*=40. Arrows are included to show the general direction of the velocity vectors

At iteration time = 1000 (Fig. 4.8 and 4.9), the droplet continues to deform around the obstacles. In the octagonal obstacle case, the upstream regions of the two horns of the meniscus could force the carrier fluid out of the region and merge near the stagnation point on the downstream surface of the obstacle because there is no carrier fluid recirculating in this region.

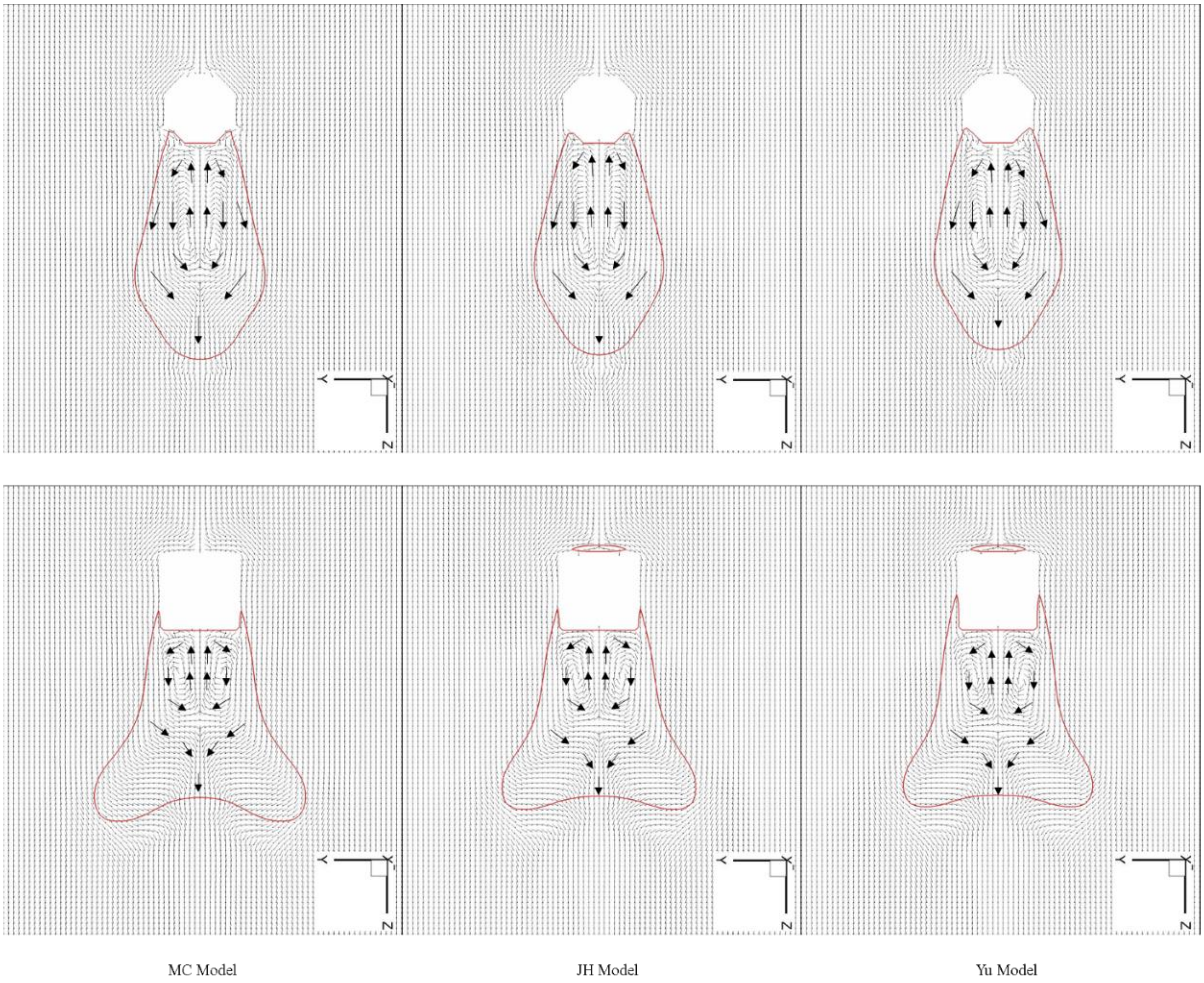

Fig. 4.12 Droplet dynamics as the wetting droplet ($\theta = 62^{o}$) impacts the obstacles for the different pseudo-potential based wetting models at lattice time = 1200. The figure shows the interface profile and the velocity vector in the plane *x*=40. Arrows are included to show the general direction of the velocity vectors

However, because of the carrier fluid recirculation near the stagnation point of the square obstacle, we did not observe similar merging of the upstream region of the horns of the meniscus (Fig. 4.11). A layer of the carrier fluid remains between the two horns. In Figures 4.8 and 4.11, we observed a blob of the droplet attached to the upstream face of the square obstacle in all the models.

Although similar blob was observed in JH and Yu models, however, a hole was left in the middle of the blob for MC model because of the greater size of the carrier fluid dead zone (Fig. 4.8). Also, we observed similar patterns in JH, Yu and MC models for the octagonal obstacle (Fig. 4.9). In general, the velocity vector field on the downstream surface of the both obstacles are pointing outwards as if the droplet is moving away from this surface. Upon further inspection, we notice for square obstacle that the velocity vector field inside the droplet (near the base of the separated horns) points towards the surface while the velocity field vectors in the carrier fluid (near the center of the surface) points outward as if the carrier fluid is being forced outwards (Fig. 4.11). The horns of the meniscus of the droplet continue to coalesce and the downstream tip of the droplet begins to assume a convex shape like a pendant droplet in the octagonal obstruction around lattice time = 1200 (Fig. 4.12). Similar behavior was observed in the square obstruction as the base of the meniscus horns have now merged while the downstream tip of the droplet is yet to assume a convex configuration. In the square obstruction, we observe a single satellite droplet in JH and Yu models but two satellite droplets in MC model. Likewise, we observe similar behavior in the octagonal obstacle except that two satellite droplets were formed in all models (Fig. 4.9).

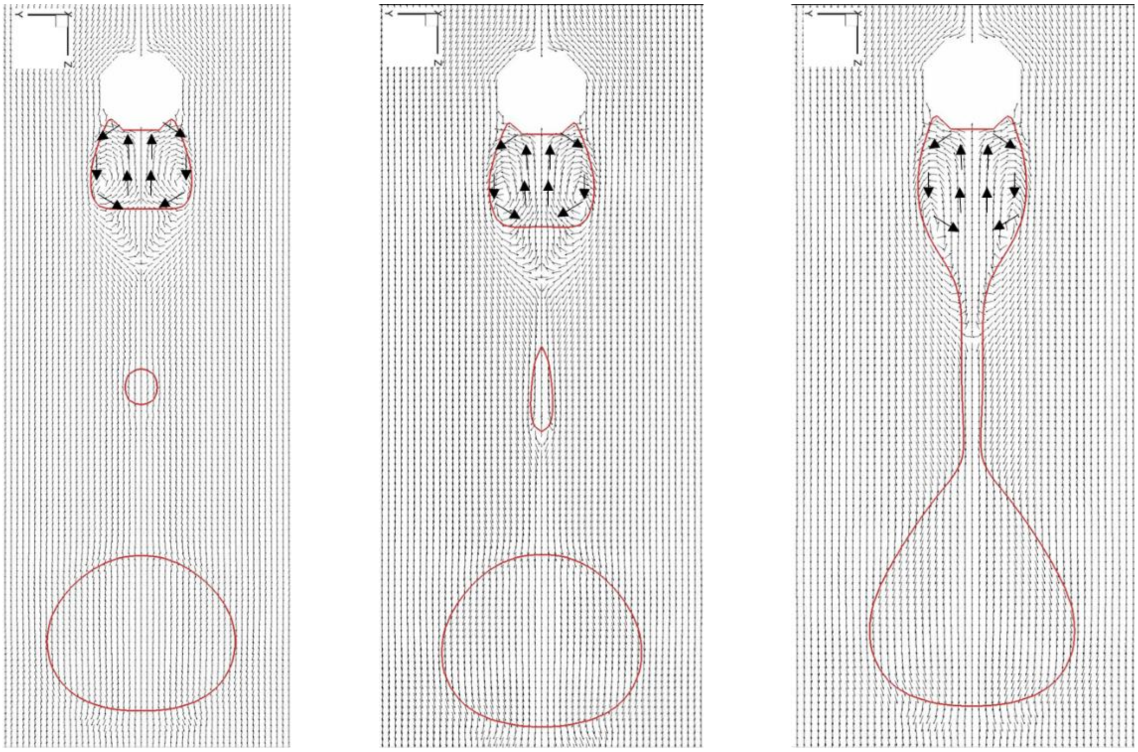

MC Model JH Model Yu Model

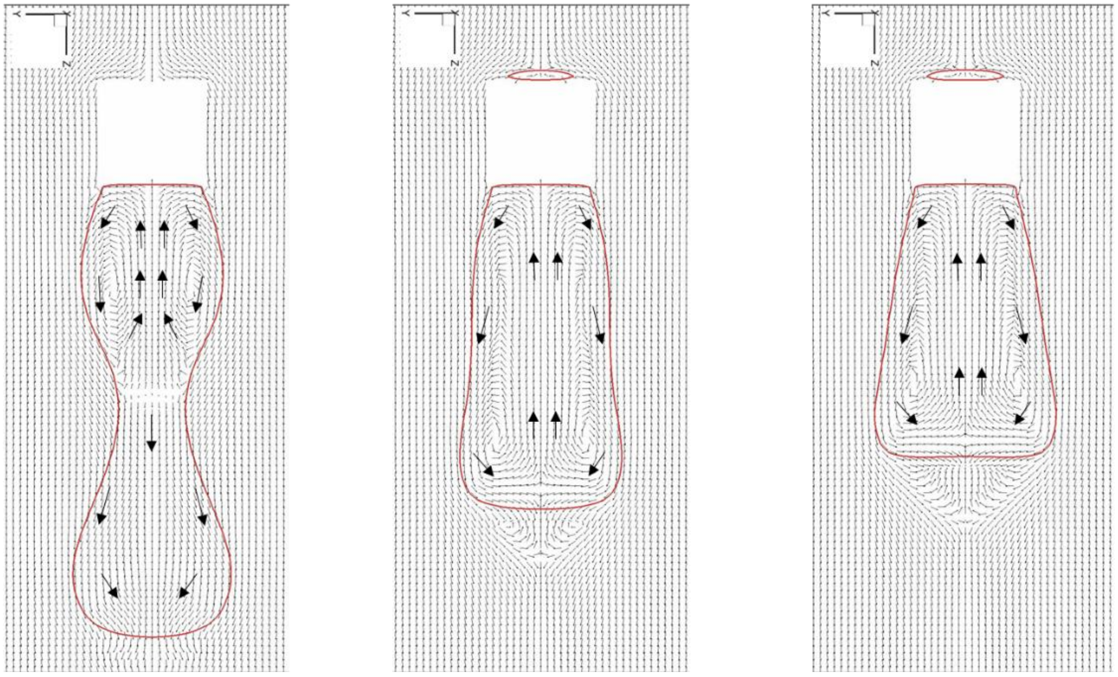

Fig. 4.13 Droplet dynamics as the wetting droplet ($\theta = 62^o$) impacts the obstacles for the different pseudo-potential based wetting models at lattice time = 1800. The figure shows the interface profile and the velocity vector in the plane *x*=40. Arrows are included to show the general direction of the velocity vectors.

Interestingly, recirculating region begins to appear in the center of the droplet together with a layer of flow near the interface of the droplet in the downstream direction for both obstacles (Fig. 4.12). The profile of the velocity vector field for the square obstruction is quite different from the octagonal obstacle. This explains why the downstream interface of the droplet is still concave. In addition, the strength of the recirculating region in MC model for the square obstacle appears to be smaller compared to the other models. Therefore, we notice more concavity in the MC model. In the octagonal prism case, the outer layer beyond the recirculating region appears to prevent the droplet from assuming a convex shape like a pendant droplet at a faster rate like the other two models.

In Figure 4.13, the inner recirculating velocity vector region in the pendant droplet attached to the octagonal obstacle resulted in the breakup of the droplet into a smaller pendant droplet as the outer velocity vector layer inside the droplet (near the interface of the droplet) produced daughter droplets. It is noteworthy, that the Yu model approached a pendant droplet at a slower rate than MC and JH models. At the same time, the tip of the droplet attached to the square obstacle begins to assume a convex shape as the recirculating region inside the droplet begins to grow- particularly in JH and Yu models. As such, no daughter droplets were formed in these models. Whereas, the droplet in the MC model continues to break up to form daughter droplets.

4.5.2.2 Non-wetting droplet in a wetting carrier fluid

Like our observations in the wetting droplet, the droplet deforms steadily around the obstacle and produces a concave meniscus around the obstacle (Figs. 4.14 and 4.15). Unlike the tip of the horns of the meniscus that bend inward toward the surface in the wetting droplet, the non-wetting droplet tip bends outwards and produces less wetting around both obstacles for all models (Fig. 4.16). In addition, the size of the carrier fluid dead zones is generally larger than in the wetting droplet and square obstacle appears to have more volume of dead zone than the octagonal obstacle in all models.

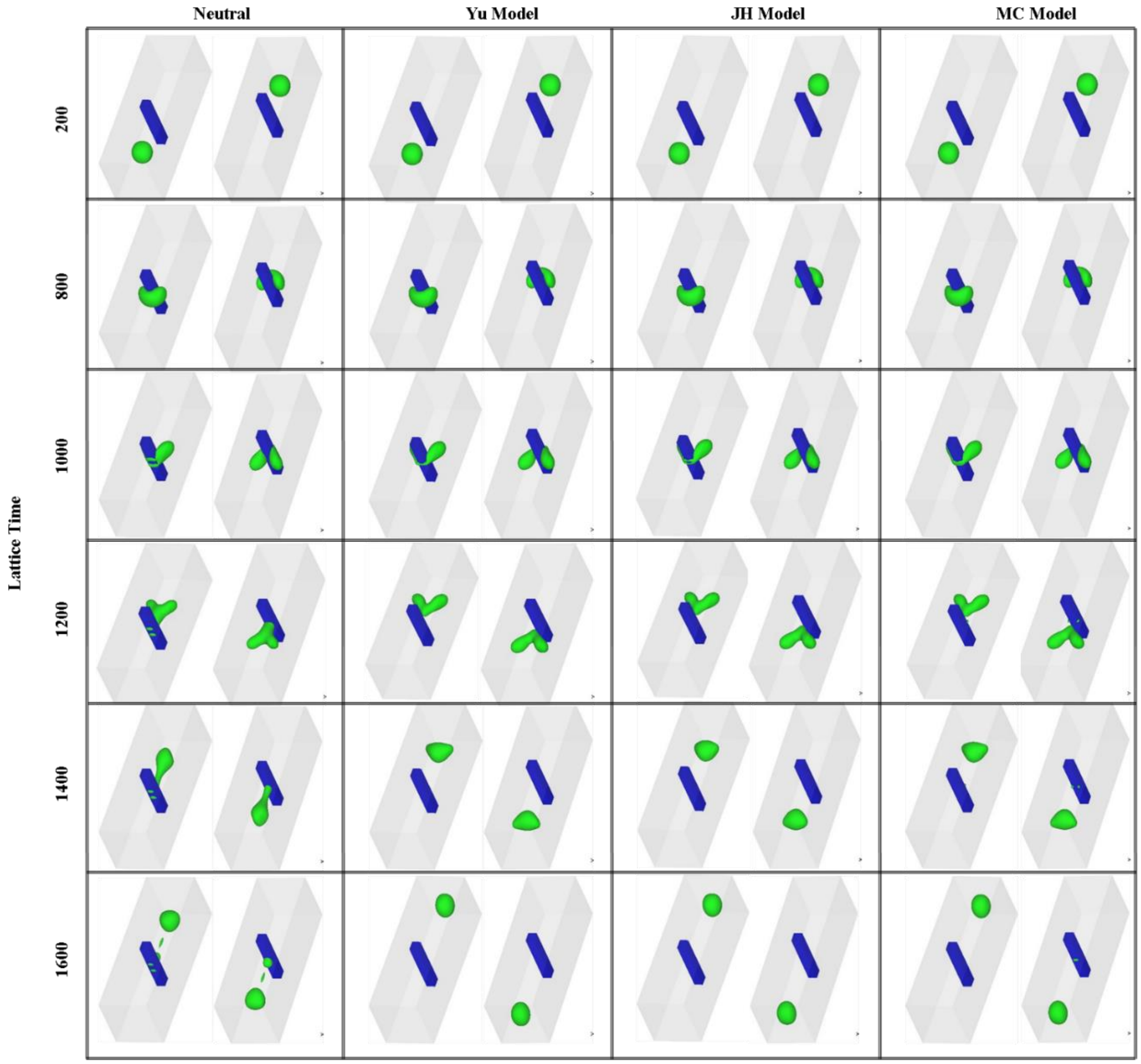

Fig. 4.14 Computed images (view from two different angles) of the impact of a non-wetting droplet ($\theta = 118^{o}$) onto a square prism obstacle at different lattice time for the different pseudo-potential based wetting model. Note that we included the image of a neutral droplet for reference.

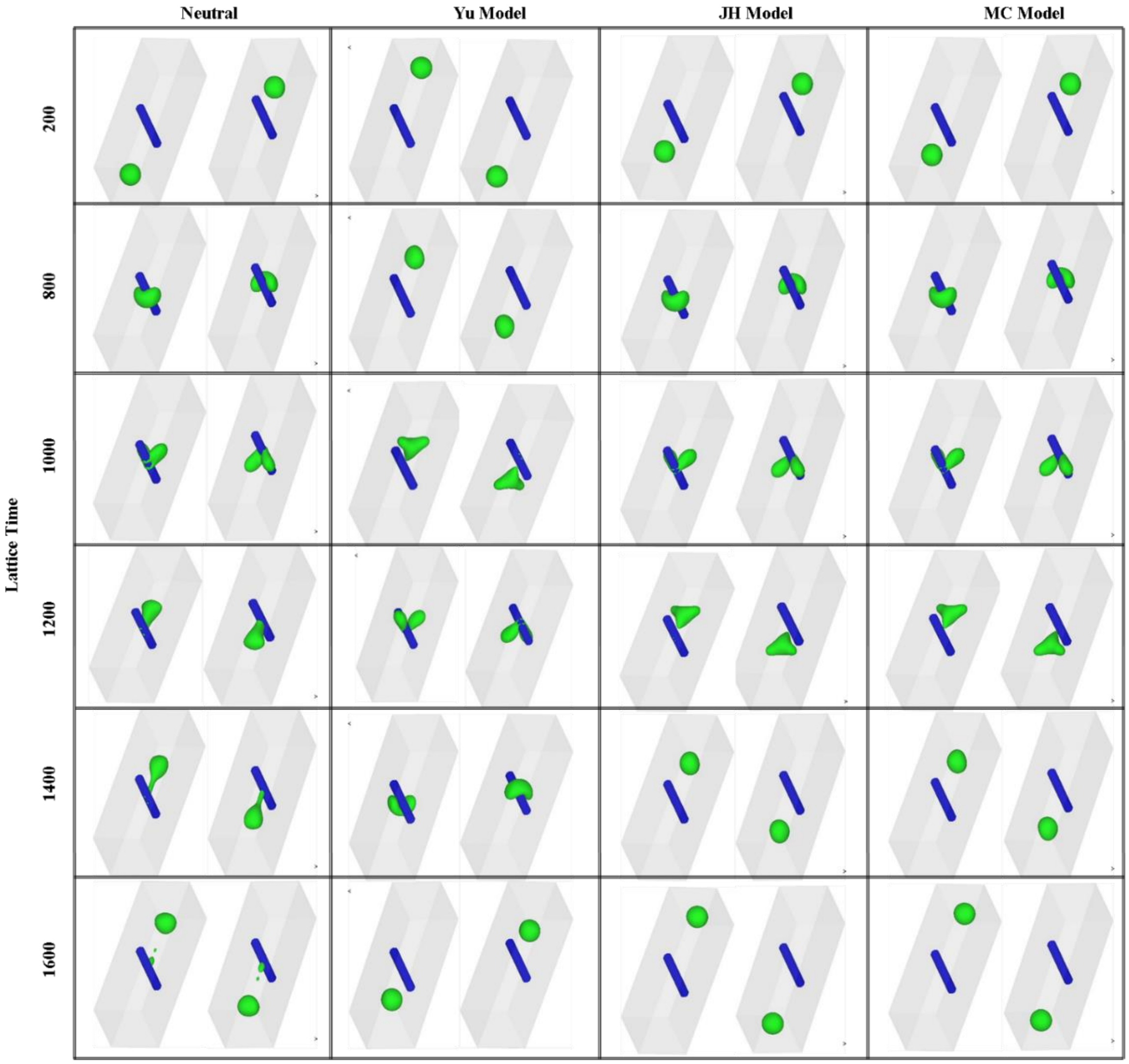

Fig. 4.15 Computed images (view from two different angles) of the impact of a non-wetting droplet ($\theta = 118^{\mathrm{o}}$) onto an octagonal prism obstacle at different lattice time for the different pseudo-potential based wetting model. Note that we included the image of a neutral droplet for reference.

Fig. 4.16 Droplet dynamics as the non-wetting droplet ($\theta = 118^{\circ}$) impacts the obstacles for the different pseudo-potential based wetting models at lattice time = 800. The figure shows the interface profile and the velocity vector in the plane *x*=40. Arrows are included to show the general direction of the velocity vectors.

In contrast to our observations in the wetting droplet, there were no recirculating regions of the carrier fluid on the downstream surface of the obstacles for all the models except for a small region in JH model for the square obstacle (Fig. 4.16).

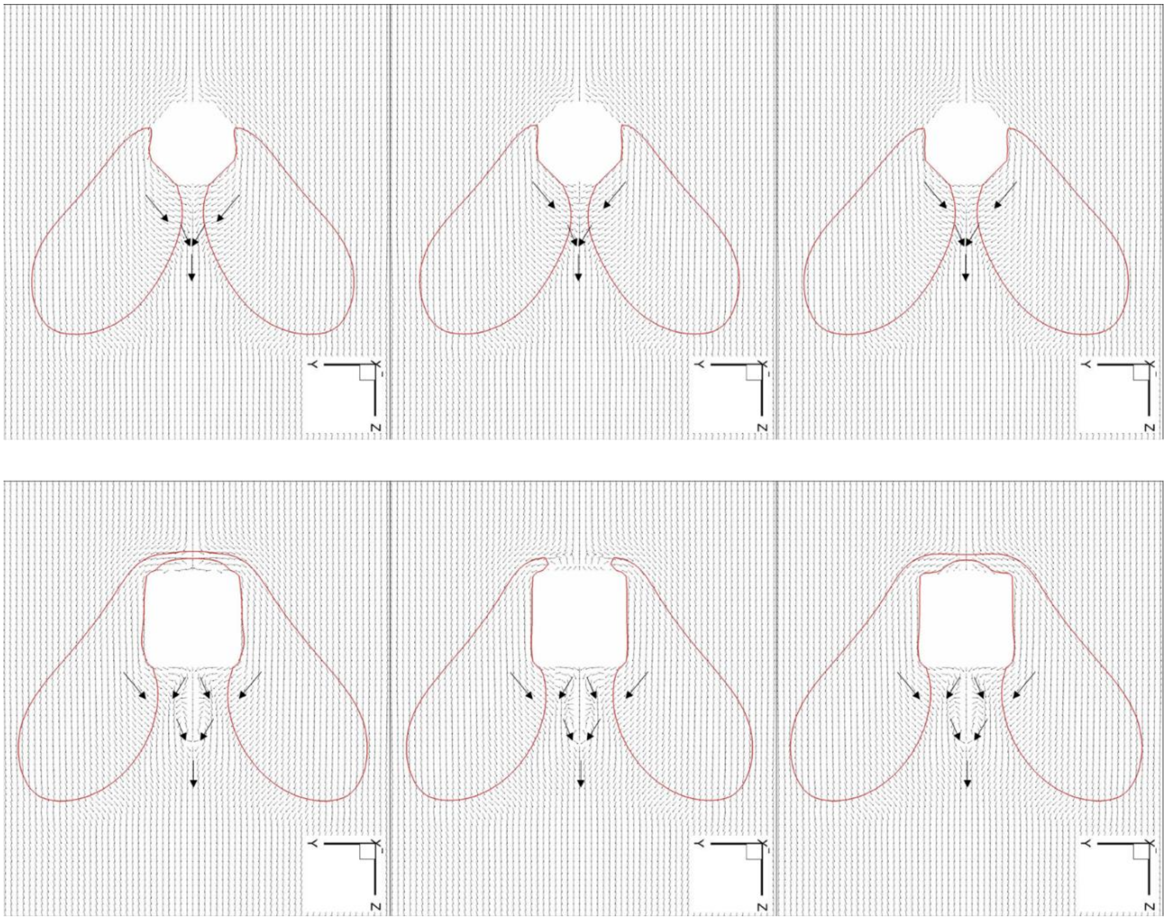

MC Model

JH Model

Yu Model

Fig. 4.17 Droplet dynamics as the non-wetting droplet ($\theta = 118^{\circ}$) impacts the obstacles for the different pseudo-potential based wetting models at lattice time = 1000. The figure shows the interface profile and the velocity vector in the plane *x*=40. Arrows are included to show the general direction of the velocity vectors.

The obstruction splits the droplet as it deforms as shown in Figure 4.17. Different from our observations in the wetting droplet case, the horns of the meniscus did not merge for the octagonal obstruction. A layer of the carrier fluid was enclosed between the two horns. We observed similar behavior in the square obstacle but the thickness of the layer is greater (Fig. 4.17). For the square prism, a thin liquid finger of the droplet was left behind on the upstream surface of the obstruction. Thicker finger was observed in MC model (Fig. 4.14).

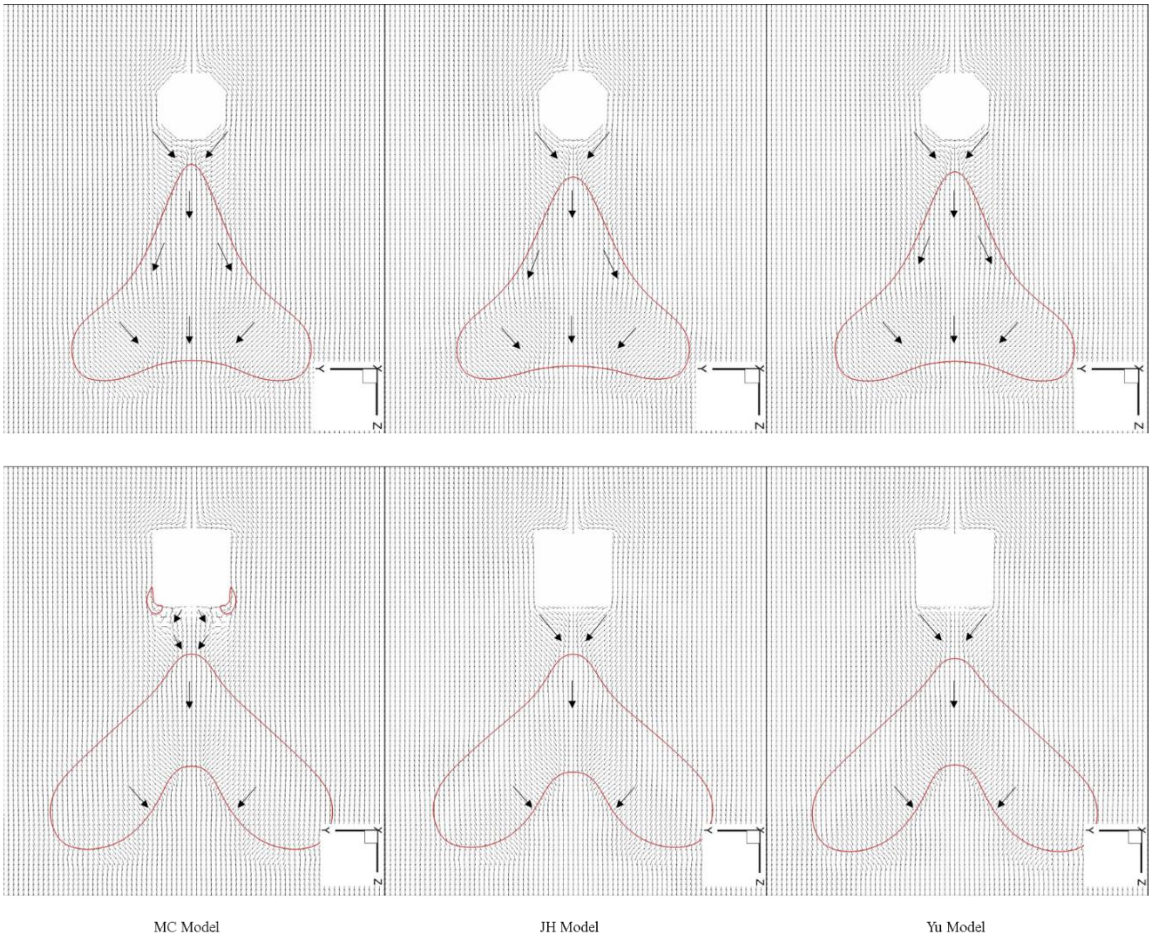

Fig. 4.18 Droplet dynamics as the non-wetting droplet ($\theta = 118^{o}$) impacts the obstacles for the different pseudo-potential based wetting models at lattice time = 1200. The figure shows the interface profile and the velocity vector in the plane *x*=40. Arrows are included to show the general direction of the velocity vectors.

The horns of the meniscus begin to coalesce at lattice time = 1200. The rate is faster in the octagonal obstacle than in the square obstacle because the tip of the droplet is more concave (Fig. 4.18). Satellite droplets where produced in the MC model for the square obstacle because of more wetting in the carrier fluid (Fig. 4.14). The velocity vector field continues to drag the droplet downstream as the horns merge together. In the MC model for the square prism, near the downstream surface of the obstacle, the carrier fluid appears to be moving outward in a concave manner. This motion helps to explain the formation of the satellite droplets.

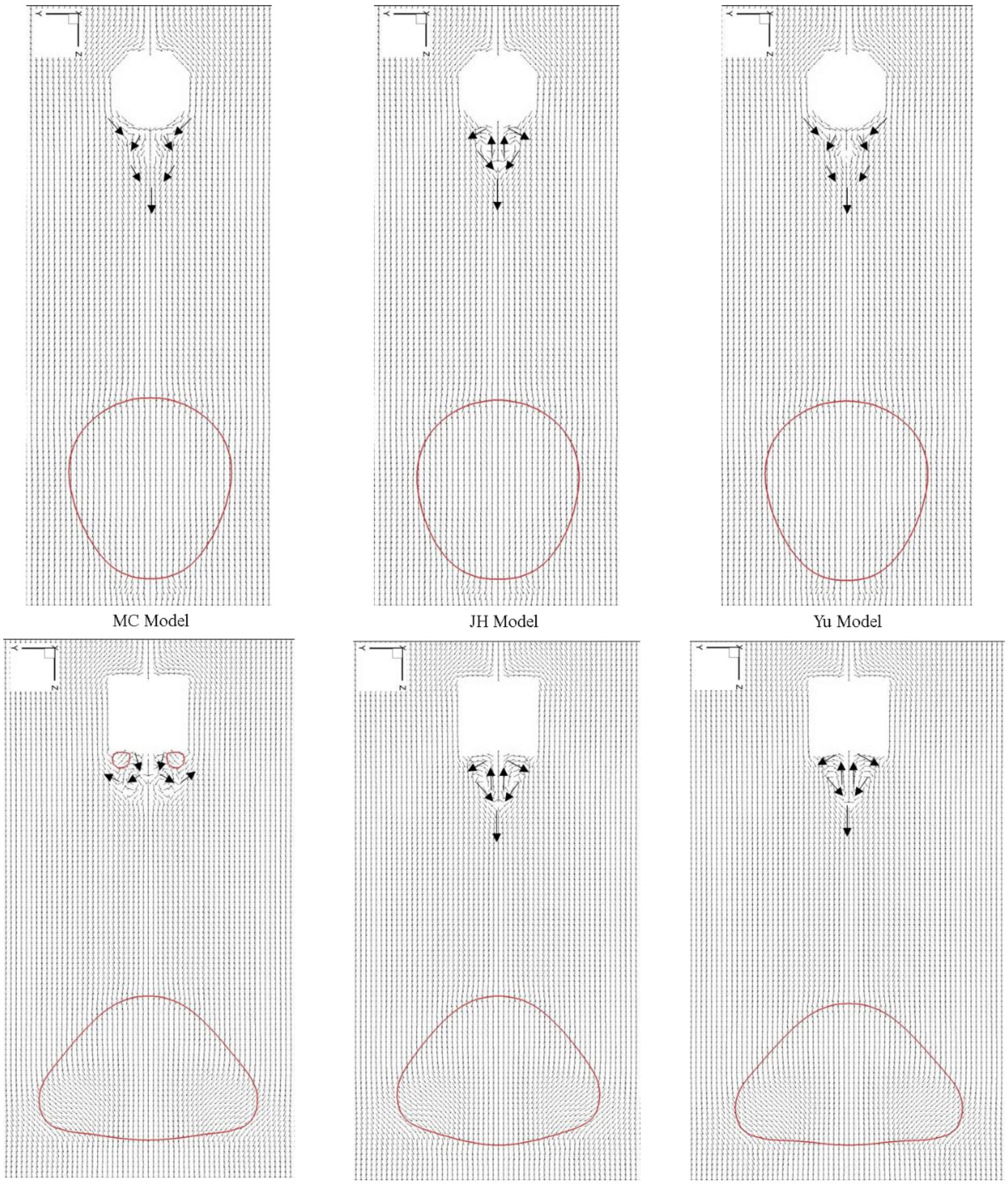

Fig. 4.19 Droplet dynamics as the non-wetting droplet ($\theta = 118^{\circ}$) impacts the obstacles for the different pseudo-potential based wetting models at lattice time = 1400. The figure shows the interface profile and the velocity vector in the plane *x*=40. Arrows are included to show the general direction of the velocity vectors.

The droplet totally detaches from the octagonal obstacle and begins to become spherical at a faster rate than the droplet through the square obstacle (Fig. 4.15 and 4.19). The two satellite droplets in the MC model also change their surfaces to approach a spherical shape. Recirculating region begins to develop on the downstream surface of the square obstruction in all models. Only a little recirculating region was observed in the JH model for the octagonal obstruction. We did not observe any recirculating region for the other models in the octagonal obstruction case (Fig. 4.19).

Taken together, when a wetting droplet (in a non-wetting carrier fluid) interacts with the obstacles, we observe more wetting in the upstream surface of the octagonal obstacle at the initial stage because of the different flow fields around the obstacle due to different geometric configurations. Subsequently, a thinner recirculating region develops in the droplet on the downstream surface of the octagonal prism compared to the square prism. This is because more wetting on the downstream surface of the square obstacle increases surface tension forces on the droplet. Hence, a thicker recirculating region is observed in the square obstacle. The thinner recirculating region in the droplet for the octagonal obstruction promotes earlier onset of necking in the droplet and formation of daughter droplets. Among the different PPBW models, we observed slower onset of necking in JH and Yu models. Consistent with our observations in the attached droplet case, we suggest that there will be greater unphysical density variation in the non-wetting carrier fluid for MC model near the downstream surface of the obstacle. This will reduce the non-wetting ability of the carrier fluid and the wetting ability of the droplet. As a result, thinner recirculating region develops and an earlier onset of necking. Similar pattern was observed in the square obstacle but daughter droplets were only formed in MC model. We also observed droplet dynamic behavior like the ones described above in the non-wetting droplet (in a wetting carrier fluid) for the two obstacle configurations. However, MC model results were slightly different from the other PPBW models in the square prism case. Our results are generally consistent with the observations in the simulations study in (Pasandideh-Fard et al., 2001) and experimental results in (Hung et al., 2002) even though the experiment considered an array of droplet impacting a wire.

4.6 Conclusion

In this paper we evaluated the performance of different pseudo-potential-based wetting models for multicomponent multiphase (MCMP) lattice Boltzmann method, including: MC model (1996) , JH model (2011) and Yu model (2015) . Because pseudo-potential MCMP lattice Boltzmann method is not strictly incompressible (Hou et al., 1997) (some dissolved components are still present in the main component), unphysical density variations are often introduced near the solid nodes by these different wetting models. We have studied the influence of this density variation on the dynamic behavior of an attached wetting or non-wetting droplet and a free wetting or non-wetting droplet moving past obstacles under the influence of gravity. The numerical results indicate that the MC model suffers from excessive unphysical wetting, specifically in the cases where the carrier fluid is non-wetting and the droplet is wetting. Consequently, there is an increase in surface tension forces between the droplet (or carrier fluid) and the solid surface which results in; (a) reduced slip velocity for the non-wetting droplet and early onset of small droplet pinch off in the case of a sliding attached droplet (b) early onset of necking and break up of droplet to create daughter droplets in the case of a wetting droplet past solid obstacles.

We hope that these side-by-side comparisons of different PPBW models in this section provide the framework for the choice of PPBW models for droplet-based numerical studies that involves fluid-solid interactions and contributes to better designs and optimization of droplet microfluidics.

4.7 References

Benzi R, Biferale L, Sbragaglia M, Succi S, Toschi F (2006) Mesoscopic modeling of a two-phase flow in the presence of boundaries: The contact angle Physical Review E 74:021509

Chen Y, Kang Q, Cai Q, Wang M, Zhang D (2015) Lattice Boltzmann Simulation of Particle Motion in Binary Immiscible Fluids Communications in Computational Physics 18:757-786

Gambosi TI (1994) Kinetic theory of gases Cambridge atmospheric and space science series

Hou S, Shan X, Zou Q, Doolen GD, Soll WE (1997) Evaluation of Two Lattice Boltzmann Models for Multiphase Flows Journal of Computational Physics 138:695-713 doi:http://dx.doi.org/10.1006/jcph.1997.5839

Hung LS, Yao SC (2002) Dripping phenomena of water droplets impacted on horizontal wire screens International Journal of Multiphase Flow 28:93-104 doi:http://dx.doi.org/10.1016/S0301-9322(01)00061-1

Jansen F, Harting J (2011) From bijels to Pickering emulsions: A lattice Boltzmann study Physical Review E 83:046707

Kang Q, Zhang D, Chen S (2005) Displacement of a three-dimensional immiscible droplet in a duct Journal of Fluid Mechanics 545:41-66

Martys NS, Chen H (1996) Simulation of multicomponent fluids in complex three-dimensional geometries by the lattice Boltzmann method Physical Review E 53:743-750

Pan C, Hilpert M, Miller CT (2004) Lattice-Boltzmann simulation of two-phase flow in porous media Water Resources Research 40:n/a-n/a doi:10.1029/2003WR002120

Pasandideh-Fard M, Bussmann M, Chandra S (2001) SIMULATING DROPLET IMPACT ON A SUBSTRATE OF ARBITRARY SHAPE 11:397-414 doi:10.1615/AtomizSpr.v11.i4.60

Sbragaglia M, Benzi R, Biferale L, Succi S, Toschi F (2006) Surface Roughness-Hydrophobicity Coupling in Microchannel and Nanochannel Flows Physical Review Letters 97:204503

5. CHAPTER FIVE: INCORPORATING THE FORCING TERM

5.1 Multi-Scale Analysis of BGK LBM with Forcing Term

In chapter four, we discussed the performance of different pseudo-potential wetting schemes in the context of multicomponent multiphase lattice Boltzmann (BGK) models. However, we identified some areas of improvements in the study. First, the LBM-BGK scheme was chosen for simplicity and does not represent the state-of-the-art approach for solving this class of problems. Secondly, we incorporated the general body force via the velocity shift method proposed by Shan and Chen (Shan and Chen, 1993). In the limit of vanishing space and time step, this method is known to introduce addition terms into the hydrodynamics equations. Finally, the density ratio was set to unity as the focus of the study was the fluid-solid interaction on the ideal wall. In subsequent chapters, we extend the investigations to large-density ratio applications. For this reasons, we review existing schemes available for incorporating the general body force into the LBM-BGK model and in later chapters address other areas of improvement.

We start from the simple and popular BGK approximation of the discrete Boltzmann equation without a forcing term given as

$$f_\alpha(\boldsymbol{x} + \boldsymbol{\xi}_\alpha \delta_t, t + \delta_t) - f_\alpha(\boldsymbol{x}, t) = -\frac{1}{\tau}\left[f_\alpha(\boldsymbol{x}, t) - f_\alpha^{(eq)}(\boldsymbol{x}, t)\right] \tag{5.1}$$

where the macroscopic fluid density ρ and velocity $\mathbf{u}$ can be obtained from the first and second moments of the density distribution function as follows

$$\rho = \sum\nolimits_\alpha f_\alpha \tag{5.2}$$

$$\rho\mathbf{u} = \sum\nolimits_{\alpha} \xi_\alpha f_\alpha \tag{5.3}$$

In addition, the equilibrium particle distribution function is given as f_α^{eq} (Guo et al., 2002)

$$f_\alpha^{eq} = \omega_\alpha \rho \left[1 + \frac{\mathbf{u} \cdot \boldsymbol{\xi}_\alpha}{c_s^2} + \frac{\mathbf{uu} : (\boldsymbol{\xi}_\alpha \boldsymbol{\xi}_\alpha - c_s^2 \boldsymbol{I})}{2c_s^4}\right] \tag{5.4}$$

In general, Eq. (5.1) can be modified to account for the physics of a general body force by introducing a forcing term as shown below

$$f_\alpha(\boldsymbol{x} + \boldsymbol{\xi}_\alpha \delta_t) - f_\alpha(\boldsymbol{x}, t) = -\frac{1}{\tau}\left[f_\alpha(\boldsymbol{x}, t) - f_\alpha^{(eq)}(\boldsymbol{x}, t)\right] + \delta_t F_\alpha \tag{5.5}$$

The velocity used in the equilibrium distribution can now be redefined as

$$\rho\mathbf{u} = \sum\nolimits_{\alpha} \xi_\alpha f_\alpha + m\boldsymbol{F}\delta t \tag{5.6}$$

where m is a constant to be determined for the different forcing schemes (Guo et al. 2002, Li et al., 2012)

As was previously discussed by Ladd et al (2001), the forcing term can be written in a power series in the particle velocity $\boldsymbol{\xi}_\alpha$. Here we adopt the form in Guo et al. (2002)

$$F_\alpha = \omega_\alpha \left[A + \frac{\mathbf{B} \cdot \boldsymbol{\xi}_\alpha}{c_s^2} + \frac{\mathbf{C} : (\boldsymbol{\xi}_\alpha \boldsymbol{\xi}_\alpha - c_s^2 \mathbf{I})}{2c_s^4}\right] \tag{5.7}$$

where A, **B** and **C** are functions of **F** that is to be determined so that the moments of **F** are consistent with the hydrodynamic equations.

Taking the zero, first and second velocity moments of the forcing term in Eq. (5.7) yields the following equations

$$\sum_{\alpha} \mathrm{F}_{\alpha} = A \tag{5.8}$$

$$\sum_{\alpha} \boldsymbol{\xi}_{\alpha} \mathrm{F}_{\alpha} = \mathbf{B} \tag{5.9}$$

$$\sum_{\alpha} \boldsymbol{\xi}_{\alpha} \boldsymbol{\xi}_{\alpha} F_{\alpha} = c_s^2 A \mathbf{I} + \frac{1}{2} [\mathbf{C} + \mathbf{C}^{\mathrm{T}}] \tag{5.10}$$

The macroscopic dynamic equations can be recovered for the lattice Boltzmann equation with the forcing term in Eq. (5.5) through the Chapman-Enskog multi-scale analysis described below. We start here with the following expansion

$$f_{\alpha} = f_{\alpha}^{(0)} + \epsilon f_{\alpha}^{(1)} + \epsilon^2 f_{\alpha}^{(2)} + \cdots \tag{5.11}$$

$$\frac{\partial}{\partial t} = \epsilon \frac{\partial}{\partial t_1} + \epsilon^2 \frac{\partial}{\partial t_2} \tag{5.12}$$

$$\frac{\partial}{\partial \boldsymbol{x}} = \epsilon \frac{\partial}{\partial \boldsymbol{x}_1} \tag{5.13}$$

$$\boldsymbol{F} = \epsilon \boldsymbol{F}_1, \qquad A = \epsilon A_1, \qquad \boldsymbol{B} = \epsilon \boldsymbol{B}_1, \qquad \boldsymbol{C} = \epsilon \boldsymbol{C}_1 \tag{5.14}$$

where ϵ is the expansion parameter that is proportional to the ratio of the lattice space to the characteristic length and $f_{\alpha}^{(0)} = f_{\alpha}^{(\mathrm{eq})}$ is the equilibrium distribution function.

Next, we expand $f_{\alpha}(\boldsymbol{x} + \boldsymbol{\xi}_{\alpha}\delta_t, t + \delta_t)$ about $\boldsymbol{x}$ and t as shown below

$$\begin{aligned} & f_\alpha(\boldsymbol{x} + \boldsymbol{\xi}_\alpha \delta_t, t + \delta_t) \\ & \quad = f_\alpha(\boldsymbol{x}, t) + \frac{\partial f_\alpha}{\partial t}\delta_t + \frac{\partial f_\alpha}{\partial \boldsymbol{x}}\boldsymbol{\xi}_\alpha \delta_t \\ & \quad + \frac{1}{2}\,{\delta_t}^2 \left[\frac{\partial^2 f_\alpha}{\partial t^2} + 2\frac{\partial^2 f_\alpha}{\partial t \partial \boldsymbol{x}}\boldsymbol{\xi}_\alpha + \frac{\partial^2 f_\alpha}{\partial \boldsymbol{x}^2}\boldsymbol{\xi}_\alpha \boldsymbol{\xi}_\alpha\right] \\ & \quad + O\left({\delta_t}^3\right) \end{aligned} \tag{5.15}$$

we now introduce the scaling in Eqs. (5.12) and (5.13) into Eq. (5.15)

$$\begin{aligned} & f_\alpha(\boldsymbol{x} + \boldsymbol{\xi}_\alpha \delta_t, t + \delta_t) \\ & \quad = f_\alpha(\boldsymbol{x}, t) + \epsilon\frac{\partial f_\alpha}{\partial t_1}\delta_t + \epsilon^2\frac{\partial f_\alpha}{\partial t_2}\delta t + \epsilon\frac{\partial f_\alpha}{\partial \boldsymbol{x}_1}\boldsymbol{\xi}_\alpha \delta_t \\ & \quad + \frac{1}{2}\,{\delta_t}^2 \left[\epsilon^2\frac{\partial^2 f_\alpha}{\partial t_1^2} + \epsilon^4\frac{\partial^2 f_\alpha}{\partial t_1^2} + 2\epsilon^2\frac{\partial^2 f_\alpha}{\partial t_1 \partial \boldsymbol{x}_1}\boldsymbol{\xi}_\alpha\right. \\ & \quad \left. + 2\epsilon^4\frac{\partial^2 f_\alpha}{\partial t_2 \partial \boldsymbol{x}_1}\boldsymbol{\xi}_\alpha + \epsilon^2\frac{\partial^2 f_\alpha}{\partial \boldsymbol{x}_1^2}\boldsymbol{\xi}_\alpha \boldsymbol{\xi}_\alpha\right] + O\left({\delta_t}^3\right) \\ & \quad + O(\epsilon^3) \end{aligned} \tag{5.16}$$

Keeping terms with ϵ^2 we obtain

$$\begin{aligned} & f_\alpha(\boldsymbol{x} + \boldsymbol{\xi}_\alpha \delta_t, t + \delta_t) \\ & \quad = f_\alpha(\boldsymbol{x}, t) + \epsilon\frac{\partial f_\alpha}{\partial t_1}\delta_t + \epsilon^2\frac{\partial f_\alpha}{\partial t_2}\delta_t + \epsilon\frac{\partial f_\alpha}{\partial \boldsymbol{x}_1}\boldsymbol{\xi}_\alpha \delta_t \\ & \quad + \frac{1}{2}\,{\delta_t}^2 \left[\epsilon^2\frac{\partial^2 f_\alpha}{\partial t_1^2} + 2\epsilon^2\frac{\partial^2 f_\alpha}{\partial t_1 \partial \boldsymbol{x}_1}\boldsymbol{\xi}_\alpha\right. \\ & \quad \left. + \epsilon^2\frac{\partial^2 f_\alpha}{\partial \boldsymbol{x}_1^2}\boldsymbol{\xi}_\alpha \boldsymbol{\xi}_\alpha\right] + O\left({\delta_t}^3\right) + O(\epsilon^3) \end{aligned} \tag{5.17}$$

Substituting in the transport Eq. (5.5),

$$\begin{aligned} &\epsilon \frac{\partial f_\alpha}{\partial t_1}\delta_t + \epsilon^2 \frac{\partial f_\alpha}{\partial t_2}\delta_t + \epsilon \frac{\partial f_\alpha}{\partial \boldsymbol{x}_1}\boldsymbol{\xi}_\alpha \delta_t \\ &\quad + \frac{1}{2}\,{\delta_t}^2 \left[\epsilon^2 \frac{\partial^2 f_\alpha}{\partial t_1^2} + 2\epsilon^2 \frac{\partial^2 f_\alpha}{\partial t_1 \partial \boldsymbol{x}_1}\boldsymbol{\xi}_\alpha \right. \\ &\quad \left. + \epsilon^2 \frac{\partial^2 f_\alpha}{\partial \boldsymbol{x}_1^2}\boldsymbol{\xi}_\alpha \boldsymbol{\xi}_\alpha \right] + O\left({\delta_t}^3\right) + O(\epsilon^3) \\ &\quad = -\frac{1}{\tau}\left[f_\alpha(\boldsymbol{x},t) - f_\alpha^{(eq)}(\boldsymbol{x},t)\right] + \delta_t \epsilon {F_1}_\alpha \end{aligned} \tag{5.18}$$

Next we apply the expansion $f_\alpha = f_\alpha^{(0)} + \epsilon f_\alpha^{(1)} + \epsilon^2 f_\alpha^{(2)} + \cdots$ with the result:

$$\begin{aligned} &\left[\epsilon \frac{\partial f_\alpha^{(0)}}{\partial t_1} + \epsilon^2 \frac{\partial f_\alpha^{(1)}}{\partial t_1} + \cdots \right]\delta_t + \left[\epsilon^2 \frac{\partial f_\alpha^{(0)}}{\partial t_2} + \right]\delta_t \\ &\quad + \left[\epsilon \frac{\partial f_\alpha^{(0)}}{\partial \boldsymbol{x}_1} + \epsilon^2 \frac{\partial f_\alpha^{(1)}}{\partial \boldsymbol{x}_1} + \cdots \right]\boldsymbol{\xi}_\alpha \delta_t \\ &\quad + \frac{1}{2}\,{\delta_t}^2 \left[\epsilon^2 \frac{\partial^2 f_\alpha^{(0)}}{\partial t_1^2} + \cdots \right] \\ &\quad + \frac{1}{2}{\delta_t}^2 \left[2\epsilon^2 \frac{\partial^2 f_\alpha^{(0)}}{\partial t_1 \partial \boldsymbol{x}_1} + \cdots \right]\boldsymbol{\xi}_\alpha \\ &\quad + \frac{1}{2}\,{\delta_t}^2 \left[\epsilon^2 \frac{\partial^2 f_\alpha^{(0)}}{\partial \boldsymbol{x}_1^2} + \cdots \right]\boldsymbol{\xi}_\alpha \boldsymbol{\xi}_\alpha + O\left({\delta_t}^3\right) + O(\epsilon^3) \\ &\quad = -\frac{1}{\tau \delta_t}\left[\epsilon f_\alpha^{(1)} + \epsilon^2 f_\alpha^{(2)} + \cdots \right]\delta t + \delta_t \epsilon {F_1}_\alpha \end{aligned} \tag{5.19}$$

Equating terms of the same order of ϵ we obtain

$$O(\epsilon^0) \ : \qquad f_\alpha^{(0)} = f_\alpha^{(eq)} \tag{5.20}$$

$$O(\epsilon^1) \ : \qquad \frac{\partial f_\alpha^{(0)}}{\partial t_1} + \boldsymbol{\xi}_\alpha \frac{\partial f_\alpha^{(0)}}{\partial \boldsymbol{x}_1} = -\frac{1}{\tau\delta_t} f_\alpha^{(1)} + F_{1\alpha} \tag{5.21}$$

$$\begin{aligned} O(\epsilon^2) \ : \qquad & \frac{\partial f_\alpha^{(0)}}{\partial t_2} + \frac{\partial f_\alpha^{(0)}}{\partial t_1} + \boldsymbol{\xi}_\alpha \frac{\partial f_\alpha^{(1)}}{\partial \boldsymbol{x}_1} \\ & + \frac{1}{2}\,\delta_t \left[\frac{\partial^2 f_\alpha^{(0)}}{\partial t_1^2} + 2\boldsymbol{\xi}_\alpha \frac{\partial^2 f_\alpha^{(0)}}{\partial t_1 \partial \boldsymbol{x}_1} \right. \\ & \left. + \boldsymbol{\xi}_\alpha \boldsymbol{\xi}_\alpha \frac{\partial^2 f_\alpha^{(0)}}{\partial \boldsymbol{x}_1^2} \right] + O\left(\delta_t{}^2\right) \\ & + O(\epsilon^3) = -\frac{1}{\tau\delta_t} f_\alpha^{(2)} \end{aligned} \tag{5.22}$$

One can use Eq. (5.21) to simplify the term $\boldsymbol{\xi}_\alpha \frac{\partial f_\alpha^{(1)}}{\partial \boldsymbol{x}_1}$ in Eq.(5.22)

$$\begin{aligned} & \frac{\partial f_\alpha^{(0)}}{\partial t_2} + \left(1 - \frac{1}{2\tau}\right) \left[\frac{\partial f_\alpha^{(1)}}{\partial t_1} + \boldsymbol{\xi}_\alpha \frac{\partial f_\alpha^{(1)}}{\partial \boldsymbol{x}_1} \right] \\ & \qquad = -\frac{1}{\tau\delta_t} f_\alpha^{(2)} - \frac{\delta t}{2} \left[\frac{\partial F_{1\alpha}}{\partial t_1} + \boldsymbol{\xi}_\alpha \frac{\partial F_{1\alpha}}{\partial \boldsymbol{x}_1} \right] \end{aligned} \tag{5.23}$$

To obtain the macroscopic equations we take the zero, first and second velocity moments of Eqs. (5.21) and (5.23). By first taking the zeroth velocity moment of equation (5.21) we obtain the macroscopic equations on the scale $t_1 = \epsilon t$ and $\boldsymbol{x}_1 = \epsilon \boldsymbol{x}$

$$\sum_{\alpha}\left(\frac{\partial f_{\alpha}^{(0)}}{\partial t_1}+\boldsymbol{\xi}_{\alpha}\frac{\partial f_{\alpha}^{(0)}}{\partial \boldsymbol{x}_1}\right)=\sum_{\alpha}\left(-\frac{1}{\tau\delta_t}f_{\alpha}^{(1)}+F_{1\alpha}\right) \tag{5.24}$$

$$\begin{aligned}\frac{\partial}{\partial t_1}\left(\sum_{\alpha}f_{\alpha}^{(0)}\right)+\frac{\partial}{\partial \boldsymbol{x}_1}\left(\sum_{\alpha}\boldsymbol{\xi}_{\alpha}f_{\alpha}^{(0)}\right)\\ = -\frac{1}{\tau\delta_t}\left(\sum_{\alpha}f_{\alpha}^{(1)}\right)+\sum_{\alpha}F_{1\alpha}\end{aligned} \tag{5.25}$$

Using the fact that $\rho = \sum_{\alpha} f_{\alpha} = \sum_{\alpha} f_{\alpha}^{(0)}$ and $\rho\mathbf{u} = \sum_{\alpha}\boldsymbol{\xi}_{\alpha}f_{\alpha}^{(0)} = \sum_{\alpha}\boldsymbol{\xi}_{\alpha}f_{\alpha}$ we obtain

$$\frac{\partial\rho}{\partial t_1}+\frac{\partial(\rho\boldsymbol{u}^{*})}{\partial \boldsymbol{x}_1}= A_1 \tag{5.26}$$

Eq. (5.26) allows for source term in the continuity equation. Taking the first order velocity moment of equation (5.21) yields:

$$\sum_{\alpha}\boldsymbol{\xi}_{\alpha}\left(\frac{\partial f_{\alpha}^{(0)}}{\partial t_1}+\boldsymbol{\xi}_{\alpha}\frac{\partial f_{\alpha}^{(0)}}{\partial \boldsymbol{x}_1}\right)=\sum_{\alpha}\boldsymbol{\xi}_{\alpha}\left(-\frac{1}{\tau\delta_t}f_{\alpha}^{(1)}+F_{1\alpha}\right) \tag{5.27}$$

$$\begin{aligned}\frac{\partial}{\partial t_1}\left(\sum_{\alpha}\boldsymbol{\xi}_{\alpha}f_{\alpha}^{(0)}\right)+\frac{\partial}{\partial \boldsymbol{x}_1}\left(\sum_{\alpha}\boldsymbol{\xi}_{\alpha}\boldsymbol{\xi}_{\alpha}f_{\alpha}^{(0)}\right)\\ = -\frac{1}{\tau\delta_t}\left(\sum_{\alpha}\boldsymbol{\xi}_{\alpha}f_{\alpha}^{(1)}\right)+\sum_{\alpha}\boldsymbol{\xi}_{\alpha}F_{1\alpha}\end{aligned} \tag{5.28}$$

$$\frac{\partial(p\mathbf{u})}{\partial t_1}+\frac{\partial\prod^{(0)}}{\partial \boldsymbol{x}_1}= \boldsymbol{B}_1+\frac{m}{\tau}\boldsymbol{F}_1 \tag{5.29}$$

Now let $\boldsymbol{B}_1 = n\boldsymbol{F}_1$. Eq. (5.29) becomes

$$\frac{\partial(p\mathbf{u})}{\partial t_1} + \frac{\partial \prod^{(0)}}{\partial \boldsymbol{x}_1} = \left(n + \frac{m}{\tau}\right)\boldsymbol{F}_1 \tag{5.30}$$

As before, we used the fact that $\rho\mathbf{u} = \sum_\alpha \boldsymbol{\xi}_\alpha f_\alpha^{(0)} = \sum_\alpha \boldsymbol{\xi}_\alpha f_\alpha$ and define

$$\prod\nolimits_{ij}^{(0)} = \sum\nolimits_\alpha \boldsymbol{\xi}_{\alpha i}\boldsymbol{\xi}_{\alpha j} f_\alpha^{(0)} = c_s^2 \rho \delta_{ij} + \rho \mathrm{u}_i \mathrm{u}_j \tag{5.31}$$

Similarly, we take the zero and first order moments of Eq. (5.23) to obtain the macroscopic equation on the $t_2 = \epsilon^2 t$. Zero order velocity moment yields:

$$\begin{aligned}\sum\nolimits_\alpha \left(\frac{\partial f_\alpha^{(0)}}{\partial t_2} + \left(1 - \frac{1}{2\tau}\right)\left[\frac{\partial f_\alpha^{(1)}}{\partial t_1} + \boldsymbol{\xi}_\alpha \frac{\partial f_\alpha^{(1)}}{\partial \boldsymbol{x}_1}\right]\right)\\ = \sum\nolimits_\alpha \left(-\frac{1}{\tau\delta_t} f_\alpha^{(2)} - \frac{\delta_t}{2}\left[\frac{\partial F_{1\alpha}}{\partial t_1} + \boldsymbol{\xi}_\alpha \frac{\partial F_{1\alpha}}{\partial \boldsymbol{x}_1}\right]\right)\end{aligned} \tag{5.32}$$

$$\begin{aligned}\frac{\partial}{\partial t_2}\left(\sum\nolimits_\alpha f_\alpha^{(0)}\right) + \left(1 - \frac{1}{2\tau}\right)\frac{\partial}{\partial t_1}\left(\sum\nolimits_\alpha f_\alpha^{(1)}\right)\\ + \left(1 - \frac{1}{2\tau}\right)\frac{\partial}{\partial \boldsymbol{x}_1}\left(\sum\nolimits_\alpha \boldsymbol{\xi}_\alpha f_\alpha^{(1)}\right)\\ = -\frac{1}{\tau\delta_t}\left(\sum\nolimits_\alpha f_\alpha^{(2)}\right) - \frac{\delta_t}{2}\frac{\partial}{\partial t_1}\left(\sum\nolimits_\alpha F_{1\alpha}\right)\\ - \frac{\delta_t}{2}\frac{\partial}{\partial \boldsymbol{x}_1}\left(\sum\nolimits_\alpha \boldsymbol{\xi}_\alpha F_{1\alpha}\right)\end{aligned} \tag{5.33}$$

$$\frac{\partial \rho}{\partial t_2} = \delta_t\left(m - \frac{1}{2}\right)\frac{\partial \boldsymbol{F}_1}{\partial \boldsymbol{x}_1} \tag{5.34}$$

Next, the first order moment,

$$\sum\nolimits_{\alpha} \boldsymbol{\xi}_{\alpha} \left(\frac{\partial f_{\alpha}^{(0)}}{\partial t_2} + \left(1 - \frac{1}{2\tau}\right) \left[\frac{\partial f_{\alpha}^{(1)}}{\partial t_1} + \boldsymbol{\xi}_{\alpha} \frac{\partial f_{\alpha}^{(1)}}{\partial \boldsymbol{x}_1} \right] \right) \\ = \sum\nolimits_{\alpha} \boldsymbol{\xi}_{\alpha} \left(- \frac{1}{\tau \delta_t} f_{\alpha}^{(2)} - \frac{\delta_t}{2} \left[\frac{\partial F_{1,\alpha}}{\partial t_1} + \boldsymbol{\xi}_{\alpha} \frac{\partial F_{1\alpha}}{\partial \boldsymbol{x}_1} \right] \right) \tag{5.35}$$

$$\frac{\partial}{\partial t_2} \left(\sum\nolimits_{\alpha} \boldsymbol{\xi}_{\alpha} f_{\alpha}^{(0)} \right) + \left(1 - \frac{1}{2\tau}\right) \frac{\partial}{\partial t_1} \left(\sum\nolimits_{\alpha} \boldsymbol{\xi}_{\alpha} f_{\alpha}^{(1)} \right) \\ + \left(1 - \frac{1}{2\tau}\right) \frac{\partial}{\partial \boldsymbol{x}_1} \left(\sum\nolimits_{\alpha} \boldsymbol{\xi}_{\alpha} \boldsymbol{\xi}_{\alpha} f_{\alpha}^{(1)} \right) \\ = - \frac{1}{\tau \delta_t} \left(\sum\nolimits_{\alpha} \boldsymbol{\xi}_{\alpha} f_{\alpha}^{(2)} \right) - \frac{\delta_t}{2} \frac{\partial}{\partial t_1} \left(\sum\nolimits_{\alpha} \boldsymbol{\xi}_{\alpha} F_{1\alpha} \right) \\ - \frac{\delta_t}{2} \frac{\partial}{\partial \boldsymbol{x}_1} \left(\sum\nolimits_{\alpha} \boldsymbol{\xi}_{\alpha} \boldsymbol{\xi}_{\alpha} F_{1\alpha} \right) \tag{5.36}$$

$$\frac{\partial (\rho \boldsymbol{u}^*)}{\partial t_2} = \delta t \left(m - \frac{1}{2} \right) \frac{\partial \boldsymbol{F}_1}{\partial t_1} \\ + \frac{\partial}{\partial \boldsymbol{x}_1} \left(\left(1 - \frac{1}{2\tau}\right) \Pi^{(1)} + \frac{\delta_t}{4} (\boldsymbol{C}_1 + \boldsymbol{C}_1^{\boldsymbol{T}}) \right) \tag{5.37}$$

where we have defined the first-order momentum flux as:

$$\Pi_{ij}^{(1)} = \sum\nolimits_{\alpha} \boldsymbol{\xi}_{\alpha i} \boldsymbol{\xi}_{\alpha j} f_{\alpha}^{(1)} \\ = -\tau \delta_t \left[\left(\mathrm{u}_i F_{1_j} + \mathrm{u}_j F_{1_i} \right) + c_s^2 \rho \left(\frac{\partial \mathrm{u}_i}{\partial x_{1_j}} + \frac{\partial \mathrm{u}_j}{\partial x_{1_i}} \right) \\ - \frac{1}{2} \left(C_{1_{ij}} + C_{1_{ji}} \right) \right] \tag{5.38}$$

Taken together, we obtain the momentum equation on the $t_2 = \epsilon^2 t$ time scale as;

$$\begin{aligned}\frac{\partial(\rho \mathrm{u}_i)}{\partial t_2} = {} & \delta_t\left(m - \frac{1}{2}\right)\frac{\partial F_{1_i}}{\partial t_1} \\ & + \frac{\partial}{\partial x_j}\left(\nu\rho\left(\frac{\partial \mathrm{u}_i}{\partial x_{1_j}} + \frac{\partial \mathrm{u}_j}{\partial x_{1_i}}\right)\right. \\ & + \delta t\left[\left(\tau - \frac{1}{2}\right)\left(\mathrm{u}_i F_{1_j} + \mathrm{u}_j F_{1_i}\right)\right. \\ & \left.\left. - \frac{\tau}{2}\left(C_{1_{ij}} + C_{1_{ji}}\right)\right]\right)\end{aligned} \tag{5.39}$$

$$\nu = \left(\tau - \frac{1}{2}\right)c_s^2\delta_t \tag{5.40}$$

At this point, we believe that a few comments about the multi-scale analysis above is in order. First we observe additional contributions to the viscous stress due to discrete effects and the presence of the body force Eq. (5.38). In addition, we notice the presence of addition spatial and temporal derivatives terms in Eqs. (5.34) and (5.37). These extra terms will influence the changes in the density and momentum. Consequently, Guo et al. (2002) proposed that to match the correct Navier-Stokes equation the velocity needs to be defined in a way so that the effect of the forcing term is included. Furthermore, the forcing sceme should be defined to cancel out the contributions of the force term to the momentum flux equation. In the next section, we provide brief description of existing methods of incorporating forcing term.

5.2 Review of Existing Methods of Incorporating the Forcing Term

5.2.1 He Method:

The forcing scheme proposed by He et al., (1997) takes the form

$$m = 0;\ \ A = 0;\ \ \mathbf{B} = \mathbf{F} \quad and \quad \mathbf{C} = \mathbf{0} \tag{5.41}$$

$$\mathrm{F}_\alpha = \frac{\omega_\alpha \mathbf{F} \cdot \boldsymbol{\xi}_\alpha}{c_s^2} \tag{5.42}$$

$$\rho\bar{\mathbf{v}} = \rho\mathbf{v} = \rho\mathbf{u} = \sum\nolimits_{\boldsymbol{\alpha}} \boldsymbol{\xi}_\alpha f_\alpha \tag{5.43}$$

Substituting in Eqs. (5.30), (5.34), (5.39) and combining the results on the t_1 and t_2 time scale we obtain the following macroscopic equations

$$\frac{\partial\rho}{\partial t} + \frac{\partial(\rho\bar{\mathbf{v}})}{\partial\boldsymbol{x}} = -\frac{\delta t}{2}\frac{\partial\mathbf{F}}{\partial\boldsymbol{x}} \tag{5.44}$$

$$\begin{aligned}\frac{\partial(\rho\bar{\mathbf{v}})}{\partial t} + \frac{\partial(\rho\bar{\mathbf{v}}\bar{\mathbf{v}})}{\partial\boldsymbol{x}} &\\ = -\frac{\partial(c_s^2\rho)}{\partial x} + \nu\frac{\partial}{\partial x}\left[\rho\left(\frac{\partial\bar{\mathbf{v}}}{\partial\boldsymbol{x}} + \left(\frac{\partial\bar{\mathbf{v}}}{\partial\boldsymbol{x}}\right)^T\right)\right] + \mathbf{F} &\\ - \frac{\delta t}{2}\epsilon\frac{\partial\mathbf{F}}{\partial t_1} + \left(\tau - \frac{1}{2}\right)\delta t\frac{\partial}{\partial\boldsymbol{x}}(\bar{\mathbf{v}}\mathbf{F} + \bar{\mathbf{v}}\mathbf{F}^{\mathrm{T}})&\end{aligned} \tag{5.45}$$

The first problem with this forcing scheme is that to match the Navier-Stokes equation the spatial and temporal changes of body force should only vary slightly. This implies that **F** should be a constant force. Hence, this method is mainly used for applications that involve constant body force. Despite this consideration, the last term in Eq. (5.45) may not be negligible even though **F** is a nonzero constant because of the velocity gradient.

5.2.2 Luo Method:

In the forcing scheme proposed independently by (Luo, 1998) and Marty et al. (1998), the representation of the force is derived from the kinetic equations and it takes the following form

$$m = 0; \;\; A = 0; \;\; \mathbf{B} = \mathbf{F} \quad and \quad \mathbf{C} = 2\mathbf{F}\mathbf{v} \tag{5.46}$$

Such that the forcing term is

$$\mathrm{F}_\alpha = \omega_\alpha \left[\frac{(\boldsymbol{\xi}_\alpha - \mathbf{v})}{c_s^2} + \frac{(\boldsymbol{\xi}_\alpha \cdot \mathbf{v})\boldsymbol{\xi}_\alpha}{c_s^4} \right] \cdot \mathbf{F} \tag{5.47}$$

where the fluid velocity $\bar{\mathbf{v}}$, velocity used in the equilibrium density function $\mathbf{u}$ and the velocity used in the forcing term $\mathbf{v}$ are all equal

$$\rho\bar{\mathbf{v}} = \rho\mathbf{v} = \rho\mathbf{u} = \sum\nolimits_{\boldsymbol{\alpha}} \boldsymbol{\xi}_\alpha f_\alpha \tag{5.48}$$

As before, the macroscopic equations obtained by combining the results on the t_1 and t_2 time scales can be given as

$$\frac{\partial \rho}{\partial t} + \frac{\partial(\rho\bar{\mathbf{v}})}{\partial \boldsymbol{x}} = -\frac{\delta t}{2}\frac{\partial \mathbf{F}}{\partial \boldsymbol{x}} \tag{5.49}$$

$$\frac{\partial(\rho\bar{\mathbf{v}})}{\partial t}+\frac{\partial(\rho\bar{\mathbf{v}}\bar{\mathbf{v}})}{\partial \boldsymbol{x}} = -\frac{\partial(c_s^2\rho)}{\partial \boldsymbol{x}}+\mathbf{F}+\nu\frac{\partial}{\partial \boldsymbol{x}}\left[\rho\left(\frac{\partial\bar{\mathbf{v}}}{\partial \boldsymbol{x}}+\left(\frac{\partial\bar{\mathbf{v}}}{\partial \boldsymbol{x}}\right)^T\right)\right] - \frac{\delta t}{2}\epsilon\frac{\partial\mathbf{F}}{\partial t_1}+\frac{\delta t}{2}\frac{\partial}{\partial \boldsymbol{x}}(\bar{\mathbf{v}}\mathbf{F}+\bar{\mathbf{v}}\mathbf{F}^{\mathrm{T}}) \qquad (5.50)$$

Although this method considered the contribution of the forcing term to the momentum flux, it however offered little to no improvements to the previous method. The additional terms that are present in the previous term are not eliminated in this method. Therefore, this method suffers from limitations like those found in the previous method.

To address the limitations in the methods described so far, Ladd and Verberg (2001) proposed a new method that modifies the forcing term in Eq. (5.47). In this method, the forcing term is expanded in a power series in the particle velocity. This resulted in the redefinition of **C** in Eq. (5.46) as shown below

$$m=0;\; A=0;\; \mathbf{B}=\mathbf{F}\quad and\quad \mathbf{C}=\left(\tau-\frac{1}{2}\right)(\mathbf{vF}+\mathbf{vF}^{\mathrm{T}}) \qquad (5.51)$$

Accordingly, the forcing term becomes

$$\mathrm{F}_\alpha=\omega_\alpha\left(1-\frac{1}{2\tau}\right)\left[\frac{(\boldsymbol{\xi}_\alpha-\mathbf{v})}{c_s^2}+\frac{(\boldsymbol{\xi}_\alpha\cdot\mathbf{v})\boldsymbol{\xi}_\alpha}{c_s^4}\right]\cdot\mathbf{F} \qquad (5.52)$$

and the corresponding macroscopic equations are

$$\frac{\partial\rho}{\partial t}+\frac{\partial(\rho\bar{\mathbf{v}})}{\partial \boldsymbol{x}}=-\frac{\delta t}{2}\frac{\partial\mathbf{F}}{\partial \boldsymbol{x}} \qquad (5.53)$$

$$\frac{\partial(\rho\bar{\mathbf{v}})}{\partial t}+\frac{\partial(\rho\bar{\mathbf{v}}\bar{\mathbf{v}})}{\partial \boldsymbol{x}} = -\frac{\partial(c_s^2\rho)}{\partial \boldsymbol{x}}+\mathbf{F}+\nu\frac{\partial}{\partial \boldsymbol{x}}\left[\rho\left(\frac{\partial\bar{\mathbf{v}}}{\partial \boldsymbol{x}}+\left(\frac{\partial\bar{\mathbf{v}}}{\partial \boldsymbol{x}}\right)^T\right)\right] - \frac{\delta t}{2}\epsilon\frac{\partial \mathbf{F}}{\partial t_1} \tag{5.54}$$

As can be seen in Eq. (5.54), the contribution to the momentum flux by the additional term $(\bar{\mathbf{v}}\mathbf{F}+\bar{\mathbf{v}}\mathbf{F}^{\mathrm{T}})$ vanishes. Meanwhile, the influence on the density due to spatial variation of the force (Eq. 5.53) and momentum flux due to temporal variation of the force are not eliminated. As before, if **F** is constant, Eqs. (5.53) and (5.54) will be identical to the Navier-Stokes equation.

Another version of the forcing term proposed by Ladd and Verberg (2001) required the redefinition of the fluid velocity to account for the effect of the spatial variation of the force on density of the fluid in Eq. (5.53).

$$\rho\bar{\mathbf{v}} = \sum_{\boldsymbol{\alpha}}\boldsymbol{\xi}_\alpha f_\alpha + \frac{\delta t}{2}\mathbf{F} \tag{5.55}$$

Here, the velocity used in the computation of the equilibrium distribution function and the forcing term are unchanged from the earlier formulation.

$$\rho\mathbf{v} = \rho\mathbf{u} = \sum_{\boldsymbol{\alpha}}\boldsymbol{\xi}_\alpha f_\alpha \tag{5.56}$$

This yields the following macroscopic equation

$$\frac{\partial \rho}{\partial t} + \frac{\partial (\rho \bar{\mathbf{v}})}{\partial \boldsymbol{x}} = 0 \tag{5.57}$$

$$\begin{aligned}\frac{\partial (\rho \bar{\mathbf{v}})}{\partial t} + \frac{\partial (\rho \bar{\mathbf{v}} \bar{\mathbf{v}})}{\partial \boldsymbol{x}} \\ = -\frac{\partial (c_s^2 \rho)}{\partial \boldsymbol{x}} + \nu \frac{\partial}{\partial \boldsymbol{x}} \left[\rho \left(\frac{\partial \bar{\mathbf{v}}}{\partial \boldsymbol{x}} + \left(\frac{\partial \bar{\mathbf{v}}}{\partial \boldsymbol{x}} \right)^T \right) \right] + \mathbf{F} \\ - \frac{\delta t}{2} \epsilon^2 \frac{\partial \mathbf{F}}{\partial t_2} - \frac{3(\delta t)^2}{4} \frac{\partial}{\partial \boldsymbol{x}} \left(\frac{\mathbf{FF}}{\rho} \right) \\ - \frac{\delta t}{2} \nu \frac{\partial}{\partial \boldsymbol{x}} \left[\left(\frac{\partial \mathbf{F}}{\partial \boldsymbol{x}} + \left(\frac{\partial \mathbf{F}}{\partial \boldsymbol{x}} \right)^T \right) \right]\end{aligned} \tag{5.58}$$

Although the continuity equation is obtained without any additional term, more additional terms were introduced into the momentum flux equation. First, the term $\frac{\delta t}{2} \epsilon^2 \frac{\partial \mathbf{F}}{\partial t_2}$. This term may be considered negligible since ϵ^2 and δt are small. Secondly, the terms $\frac{\partial}{\partial x} \left(\frac{\mathbf{FF}}{\boldsymbol{\rho}} \right)$ and $\frac{\delta t}{2} \nu \frac{\partial}{\partial x} \left[\left(\frac{\partial \mathbf{F}}{\partial x} + \left(\frac{\partial \mathbf{F}}{\partial x} \right)^T \right) \right]$ will clearly introduce some errors in the momentum flux equation.

5.2.3 Shan and Chen Method:

This method is referred to as the velocity shift method. The force is incorporated into the model by shifting the velocity in the equilibrium distribution function. Recently, following the theoretical comparative analysis by Huang et al. (2011), Li et al. (2012) expressed this scheme in a compact form that is like the general form of forcing scheme previously discussed. Note that in the general form the shifted velocity is now absorbed into the forcing term in Eq. (5.59). Thus, the Shan and Chen method takes the from

$$m = 0; \;\; A = 0; \;\; \mathbf{B} = \mathbf{F} \quad and \quad \mathbf{C} = \left(\mathbf{vF} + \mathbf{vF}^{\mathrm{T}}\right) \tag{5.59}$$

with the forcing term,

$$\mathrm{F}_\alpha = \omega_\alpha \left[\frac{(\boldsymbol{\xi}_\alpha - \mathbf{v})}{c_s^2} + \frac{(\boldsymbol{\xi}_\alpha \cdot \mathbf{v})\boldsymbol{\xi}_\alpha}{c_s^4}\right] \cdot \mathbf{F} \tag{5.60}$$

where the velocity used in the equilibrium distribution function is given as

$$\rho\mathbf{u} = \sum\nolimits_{\boldsymbol{\alpha}} \boldsymbol{\xi}_\alpha f_\alpha \tag{5.61}$$

and the shifted velocity used in the forcing term as

$$\rho\mathbf{v} = \sum\nolimits_{\boldsymbol{\alpha}} \boldsymbol{\xi}_\alpha f_\alpha + \tau \frac{\delta t}{2} \mathbf{F} \tag{5.62}$$

The fluid velocity is now defined as

$$\rho\bar{\mathbf{v}} = \sum\nolimits_{\boldsymbol{\alpha}} \boldsymbol{\xi}_\alpha f_\alpha + \frac{\delta t}{2} \mathbf{F} \tag{5.63}$$

The macroscopic equation recovered from this method can be expressed as

$$\frac{\partial \rho}{\partial t} + \frac{\partial(\rho\mathbf{u})}{\partial \boldsymbol{x}} = -\frac{\delta t}{2}\frac{\partial \mathbf{F}}{\partial \boldsymbol{x}} \tag{5.64}$$

$$\frac{\partial(\rho\mathbf{u})}{\partial t} + \frac{\partial(\rho\mathbf{u})}{\partial\boldsymbol{x}} = -\frac{\partial(c_s^2\rho)}{\partial\boldsymbol{x}} + \mathbf{F} - \epsilon\frac{\delta t}{2}\frac{\partial\mathbf{F}}{\partial t_1} + \nu\frac{\partial}{\partial\boldsymbol{x}}\left[\rho\left(\frac{\partial\mathbf{u}}{\partial\boldsymbol{x}} + \left(\frac{\partial\mathbf{u}}{\partial\boldsymbol{x}}\right)^T\right)\right] - \delta t\frac{\partial}{\partial\boldsymbol{x}}\left[\frac{1}{2}(\mathbf{uF} + \mathbf{uF}^{\mathrm{T}}) - \tau^2\frac{\mathbf{FF}}{\rho}\right] \tag{5.65}$$

From the equations, above, we can see that the Shan and Chen model does not recover the correct fluid flow macroscopic equations in the macroscopic limit. Various studies have demonstrated theoretically and numerically the problems associated with this method (Huang et al., 2011; Sun et al., 2012). However, Li et al., (2012) demonstrated that the coefficient of the term $\frac{\partial}{\partial x}\left(\frac{\mathbf{FF}}{\rho}\right)$ in Eq. (5.63) is associated with the numerical stability of this method.

5.2.4 Exact Difference Method:

In the same study by Li et al., (2012), the exact-difference-method developed by Kupershtokh et al., (2009) was also reformulated in the compact general form of the forcing scheme. For the exact-difference-method, the force term is the difference of the equilibrium distribution function corresponding to the mass velocity after and before the action of the body force. After transforming to the general forcing term form, the resulting equations are like the ones derived for the Shan and Chen method. However, the definition of the fluid velocity and velocity used in the forcing term are identical. Thus, the macroscopic equations recovered is slightly different from the ones in the Shan and Chen method and determined as

$$m = 0;\ \ A = 0;\ \ \mathbf{B} = \mathbf{F} \quad and \quad \mathbf{C} = \ (\mathbf{Fv} + \ \mathbf{vF}) \tag{5.66}$$

The forcing is also chosen as

$$\mathrm{F}_\alpha = \omega_\alpha \left[\frac{(\boldsymbol{\xi}_\alpha - \mathbf{v})}{c_s^2} + \frac{(\boldsymbol{\xi}_\alpha \cdot \mathbf{v})\boldsymbol{\xi}_\alpha}{c_s^4} \right] \cdot \mathbf{F} \tag{5.67}$$

Velocity used in the equilibrium distribution function is

$$\rho\mathbf{u} = \sum\nolimits_{\boldsymbol{\alpha}} \boldsymbol{\xi}_\alpha f_\alpha \tag{5.68}$$

also, the fluid velocity and the velocity used in the forcing term is set to

$$\rho\bar{\mathbf{v}} = \rho\mathbf{v} = \ \sum\nolimits_{\boldsymbol{\alpha}} \boldsymbol{\xi}_\alpha f_\alpha + \ \frac{\delta t}{2}\mathbf{F} \tag{5.69}$$

Therefore, we obtain the following macroscopic equations

$$\frac{\partial \rho}{\partial t} + \ \frac{\partial (\rho \mathbf{u})}{\partial \boldsymbol{x}} = -\frac{\delta t}{2}\frac{\partial \mathbf{F}}{\partial \boldsymbol{x}} \tag{5.70}$$

$$\begin{aligned} \frac{\partial (\rho\mathbf{u})}{\partial t} + \ \frac{\partial (\rho\mathbf{uu})}{\partial \boldsymbol{x}} & \\ &= \ - \ \frac{\partial (c_s^2 \rho)}{\partial \boldsymbol{x}} + \ \mathbf{F} - \ \epsilon \frac{\delta t}{2}\frac{\partial \mathbf{F}}{\partial t_1} \\ &+ \ \nu \frac{\partial}{\partial \boldsymbol{x}}\left[\rho\left(\frac{\partial \mathbf{u}}{\partial \boldsymbol{x}} + \left(\frac{\partial \mathbf{u}}{\partial \boldsymbol{x}}\right)^T\right)\right] \\ &- \ \delta t \frac{\partial}{\partial \boldsymbol{x}}\left[\frac{1}{2}(\mathbf{uF} + \ \mathbf{uF}^{\mathrm{T}}) - \ \tau\delta t \frac{\mathbf{FF}}{\rho}\right] \end{aligned} \tag{5.71}$$

5.2.5 Buick and Greated Method:

Next, we consider the method introduced by Buick and Greated (2000). In this work, the fluid velocity is the same as the ones used in equilibrium distribution and forcing term. This velocity is defined to address the problem of spatial and temporal variation variations of the body force and it takes the following form

$$m = \frac{1}{2}; \;\; \mathrm{A} = 0; \;\; \mathbf{B} = \left(1 - \frac{1}{2\tau}\right)\mathbf{F} \quad and \quad \mathbf{C} = 0 \tag{5.72}$$

Note here that $\mathbf{C} = 0$. This in a way makes the formulation like the popular method proposed by He et al., (1997) described earlier except for the discrete effects are accounted for and the velocities redefined.

$$\rho\bar{\mathbf{v}} = \rho\mathbf{v} = \rho\mathbf{u} = \sum\nolimits_{\boldsymbol{\alpha}} \boldsymbol{\xi}_\alpha f_\alpha + \frac{\delta t}{2}\mathbf{F} \tag{5.73}$$

$$\mathrm{F}_\alpha = \omega_\alpha \left(1 - \frac{1}{2\tau}\right)\frac{\boldsymbol{\xi}_\alpha \cdot \mathbf{F}}{c_s^2} \tag{5.74}$$

The resulting macroscopic equations are

$$\frac{\partial\rho}{\partial t} + \frac{\partial(\rho\bar{\mathbf{v}})}{\partial\boldsymbol{x}} = 0 \tag{5.75}$$

$$\frac{\partial(\rho\bar{\mathbf{v}})}{\partial t}+\frac{\partial(\rho\bar{\mathbf{v}}\bar{\mathbf{v}})}{\partial \boldsymbol{x}} = -\frac{\partial(c_s^2\rho)}{\partial \boldsymbol{x}}+\mathbf{F}+\nu\frac{\partial}{\partial \boldsymbol{x}}\left[\rho\left(\frac{\partial\bar{\mathbf{v}}}{\partial \boldsymbol{x}}+\left(\frac{\partial\bar{\mathbf{v}}}{\partial \boldsymbol{x}}\right)^T\right)\right] + \left(\tau-\frac{1}{2}\right)\delta t\frac{\partial}{\partial \boldsymbol{x}}(\bar{\mathbf{v}}\mathbf{F}+\bar{\mathbf{v}}\mathbf{F}^{\mathrm{T}}) \tag{5.76}$$

Despite the changes made to the velocities and the **B** term in Eq. (5.72), the correct hydrodynamic equations are still not recovered. We notice the presence of an additional term given as $\left(\tau-\frac{1}{2}\right)\delta t\frac{\partial}{\partial \boldsymbol{x}}(\bar{\mathbf{v}}\mathbf{F}+\bar{\mathbf{v}}\mathbf{F}^{\mathrm{T}})$. This term contains velocity gradients and may not vanish even in applications that involve constant body force.

5.2.6 Guo Method:

Finally, we provide a brief description of the method proposed by Guo et al. (2002). Per this method, the forcing term can be defined so that the contribution of the body force to the momentum flux cancels out. In addition, the velocity is redefined to include the effect of the external force in the continuity equation. In keeping with these facts, the method takes the following form

$$m=\frac{1}{2};\ A=0;\ \mathbf{B}=\left(1-\frac{1}{2\tau}\right)\mathbf{F}\quad and\quad \boldsymbol{C} = \left(1-\frac{1}{2\tau}\right)(\mathbf{vF}+\mathbf{vF}^{\mathrm{T}}) \tag{5.77}$$

$$\rho\bar{\mathbf{v}}=\rho\mathbf{v}=\rho\mathbf{u}=\sum\nolimits_{\boldsymbol{\alpha}}\boldsymbol{\xi}_\alpha f_\alpha+\frac{\delta t}{2}\mathbf{F} \tag{5.78}$$

with the forcing term given by

$$\mathrm{F}_{\alpha} = \omega_{\alpha}\left(1 - \frac{1}{2\tau}\right)\left[\frac{(\boldsymbol{\xi}_{\alpha} - \mathbf{v})}{c_s^2} + \frac{(\boldsymbol{\xi}_{\alpha} \cdot \mathbf{v})\boldsymbol{\xi}_{\alpha}}{c_s^4}\right] \cdot \mathbf{F} \tag{5.79}$$

and the corresponding macroscopic equation taking the form

$$\frac{\partial \rho}{\partial t} + \frac{\partial(\rho\bar{\mathbf{v}})}{\partial \boldsymbol{x}} = 0 \tag{5.80}$$

$$\frac{\partial(\rho\bar{\mathbf{v}})}{\partial t} + \frac{\partial(\rho\bar{\mathbf{v}}\bar{\mathbf{v}})}{\partial \boldsymbol{x}} = -\frac{\partial(c_s^2\rho)}{\partial \boldsymbol{x}} + \mathbf{F} + \nu\frac{\partial}{\partial \boldsymbol{x}}\left[\rho\left(\frac{\partial\bar{\mathbf{v}}}{\partial \boldsymbol{x}} + \left(\frac{\partial\bar{\mathbf{v}}}{\partial \boldsymbol{x}}\right)^{T}\right)\right] \tag{5.81}$$

We can see from the equations above that the Navier-Stokes equation is clearly recovered by this method.

The different forcing schemes described in this chapter provide insights into the effect of forcing scheme on recovering consistent hydrodynamic equations. In addition, the choice of forcing scheme is very important for numerical stability. Details of the performance of the forcing methods mentioned in this section can be found in Huang et al. (2011), Sun et al. (2012) and Li et al. (2012).

5.3 References

Buick JM, Greated CA (2000) Gravity in a lattice Boltzmann model Physical Review E 61:5307-5320

Guo Z, Zheng C, Shi B (2002) Discrete lattice effects on the forcing term in the lattice Boltzmann method Physical Review E 65:046308

He X, Zou Q, Luo L-S, Dembo M (1997) Analytic solutions of simple flows and analysis of nonslip boundary conditions for the lattice Boltzmann BGK model Journal of Statistical Physics 87:115-136 doi:10.1007/BF02181482

Huang H, Krafczyk M, Lu X (2011) Forcing term in single-phase and Shan-Chen-type multiphase lattice Boltzmann models Physical Review E 84:046710

Kupershtokh AL, Medvedev DA, Karpov DI (2009) On equations of state in a lattice Boltzmann method Computers & Mathematics with Applications 58:965-974 doi:http://dx.doi.org/10.1016/j.camwa.2009.02.024

Ladd AJC, Verberg R (2001) Lattice-Boltzmann Simulations of Particle-Fluid Suspensions Journal of Statistical Physics 104:1191-1251 doi:10.1023/A:1010414013942

Li Q, Luo KH, Li XJ (2012) Forcing scheme in pseudopotential lattice Boltzmann model for multiphase flows Physical Review E 86:016709

Luo L-S (1998) Unified Theory of Lattice Boltzmann Models for Nonideal Gases Physical Review Letters 81:1618-1621

Martys NS, Shan X, Chen H (1998) Evaluation of the external force term in the discrete Boltzmann equation Physical Review E 58:6855-6857

Shan X, Chen H (1993) Lattice Boltzmann model for simulating flows with multiple phases and components Physical Review E 47:1815-1819

Sun K, Wang T, Jia M, Xiao G (2012) Evaluation of force implementation in pseudopotential-based multiphase lattice Boltzmann models Physica A: Statistical Mechanics and its Applications 391:3895-3907 doi:http://dx.doi.org/10.1016/j.physa.2012.03.008

6. CHAPTER SIX: IMPROVEMENTS TO THE SINGLE COMPONENT MULTIPHASE LATTICE BOLTZMANN METHOD

The performance of different pseudo-potential forcing schemes was investigated in recent studies by Huang et al. (2011) and Sun et al. (2012). In these studies, they discovered that the original Shan and Chen (SC) multiphase model yields inaccurate surface tension for different density ratio and relaxation times. Furthermore, it was also found that both the SC scheme and exact difference scheme (EDM) (Kupershtokh et al., 2009) produce relaxation time dependent coexistence curve. Li et al., (2012), through numerical analysis, discussed the physics behind the phenomenon that different forcing schemes exhibit different numerical performance and made a case that mechanical stability condition is dependent on the forcing scheme. In addition, the theoretical analysis in this studies revealed that the additional terms in the SC and EDM schemes is the reason for the relaxation time dependent coexistence curves (Huang et al., 2011). Based on these findings, an improved forcing scheme that can achieve thermodynamic consistency was developed by modifying the Guo et al., (2002) forcing scheme. This improved forcing scheme was later extended to simulate multiphase flows at large density ratio and relatively high Reynolds number via a multi-relaxation-time collision operator (Li et al., 2013). In this section, we provide details of the improvements to the pseudo-potential single component multiphase (SCMP) models, particularly with a focus on incorporating the appropriate equation of states to achieve large density ratio and thermodynamic consistency.

6.1 Correction to Ideal Equation of State

In dense gas the mean free path is comparable with molecular dimensions. Therefore, additional mechanisms for momentum and energy transfer must be considered (Nourgaliev et al., 2003). Many intermolecular potential can be approximated by the Lennard-Jones potential (Rowlinson, 1982; Koplik and Banavar, 1995). However, in cases where the particles are located on fixed points on the lattice the modelization of the short-range molecular attractions needs to be handled with care (Sbragaglia and Shan, 2011). Hence, Shan and Chen (1994) proposed to adopt a pairwise interparticle potential that embeds the role of exclusion volume directly (effective mass). This pseudopotential may also be viewed as a generalized density (effect of the pseudopotential is heuristically explained by the fact that density is implicitly a measure of the average distance between two particles), obeying the properties of going to zero in the limit $\rho \rightarrow 0$ and saturating to a constant value at large density. This feature of approaching a constant density at large density prevent mass collapse of the phase with high density due to attractive interactions and thus increase the numerical stability (Sbragaglia et al., 2006). Although, the pseudopotential $\psi(\rho)$ have always been given based on phenomenological considerations, its form can also be derived in comparison with a free energy approach in other to guarantee the thermodynamic consistency of the theory. Interested reader can find details of this derivation in (Sbragaglia and Shan, 2011). Next, we present the corrections to the ideal equation of state for pseudo-potential interaction force.

The interaction force experienced by the particles at x_i from the particles at x_i' can be written as

$$\mathbf{F} = -\mathrm{G}(|\boldsymbol{x} - \boldsymbol{x}'|)\psi(\boldsymbol{x})\psi(\boldsymbol{x}') \tag{6.1}$$

This force is formulated in such a way that the following constraints are satisfied (Shan, 2008):

a) Interactions should satisfy Newton's third law and conserve momentum globally

b) Interactions should be along the vector between the two interacting lattice sites

where G is a constant of proportionality that represents the overall interaction strength on the nonideal interactions.

Now when the sites that interacts with the particles on x_i are limited to *N*-neighbors, not necessarily the nearest neighbors, the total force exerted on particles at x_i is therefore given by summing over all x_i'. Given limited links that are defined as $\xi_{i\alpha}$ (does not necessarily have to be the same as those involved in the lattice Boltzmann dynamic) and requiring that the interactions be isotropic (i.e. $|x_i - x_i'| = |\xi_{i\alpha}|$ provide the same interaction strength $\mathrm{G}(|x_i - x_i'|)$ is a function of $|\xi_{i\alpha}|$) we obtain:

$$\mathrm{F}_i = -\mathrm{G}\psi(\boldsymbol{x})\sum_{\alpha} w(|\xi_{i\alpha}|^2)\psi(\boldsymbol{x} + \boldsymbol{x}')\xi_{i\alpha} \tag{6.2}$$

where $w(|\xi_{i\alpha}|^2)$ is the normalized weighting factor.

To obtain the hydrodynamic consequences of this interaction at the continuum limit, let the lattice scale approach zero $\xi_{i\alpha} \rightarrow 0$. Now expand, $\psi(x_i + x_i')$ around x_i via the Taylor's expansion

$$\begin{aligned}\mathrm{F}_i = -\mathrm{G}\psi(x_i)\Big(\mathbb{L}_{ij}^{(2)}\partial_j\psi + \frac{1}{3!}\mathbb{L}_{ijkl}^{(4)}\partial_{jkl}\psi + \frac{1}{5!}\mathbb{L}_{ijklpq}^{(6)}\partial_{jklpq}\psi \\ + \frac{1}{7!}\mathbb{L}_{ijklpqmn}^{(8)}\partial_{jklpqmn}\psi + \cdots\Big)\end{aligned} \tag{6.3}$$

where we have defined

$$\mathbb{L}_{i_1 i_2 i_3 \cdots i_n}^{(n)} = \sum_{\alpha} w(|\boldsymbol{\xi}_\alpha|^2)(\boldsymbol{\xi}_\alpha)_{i_1} \cdots (\boldsymbol{\xi}_\alpha)_{i_n} \tag{6.4}$$

Since $\psi(\rho)$ is a function of density, the interaction force F_i is a function of the gradient and higher derivatives of the density field Eq. (6.3). Therefore, if the density distribution is axially symmetric the density gradient should only have radial components and for the interaction force F_i to be perfectly aligned with the density gradient all tensors $\mathbb{L}_{i_1 i_2 i_3 \cdots i_n}^{(n)}$ must be fully isotropic (Shan, 2008). Taking the form

$$\begin{cases}\mathbb{L}^{(2n+1)} & 0 \\ \mathbb{L}_{i_1 i_2 i_3 \cdots i_{2n}}^{(\mathbf{2}n)} & e_{(2n)} c^{(2n)} \Delta_{i_1 i_2 i_3 \cdots i_n}^{(2n)}\end{cases} \tag{6.5}$$

Where $e_{(2n)}$ are arbitrary scalar constant, $c^{(2n)}$ is the lattice constant and $\Delta_{i_1 i_2 i_3 \cdots i_n}^{(2n)}$ is the $2n$-ranked fully symmetric tensor given by the recurrence relation (Wolfram, 1986)

$$\begin{cases}\Delta_{ij}^{(2)} & = \delta_{ij} \\ \Delta_{ijkl}^{(4)} & = \delta_{ij}\delta_{kl} + \delta_{ik}\delta_{jl} + \delta_{il}\delta_{jk} \\ \Delta_{i_1 i_2 i_3 \cdots i_n}^{2n} & = \sum_{j=2}^{2n} \delta_{i_1 i_2} \Delta_{i_2 i_3 \cdots i_{j-1} i_{j+1} \cdots i_{2n}}^{n}\end{cases} \tag{6.6}$$

Given that it is impossible to have all $\mathbb{L}^{(n)}$ isotropic, the problem now is how to optimize weights $w(|\boldsymbol{\xi}_\alpha|^2)$ to maximize the isotropy of $\mathbb{L}^{(n)}$. More details of this optimization procedure are provided in (Sbragaglia et al. 2007)

For example, let us consider a two-dimensional square lattice, if the nearest-neighbor sites are used, only the tensor up to the fourth order can be made isotropic. As an extension, if the next level of neighbors is included, tensors up to the eight order can be made isotropic. For the two cases, the coefficients e_2 and e_4 are given by the weights (Shan, 2008)

$$e_2 = 2w(1) + 4w(2) + 8w(4) + 20w(5) + 16w(8) + \ldots \tag{6.7}$$

$$e_4 = \frac{1}{2}w(1) + 2w(2) + 8w(4) + 25w(5) + 32w(8) + \ldots \tag{6.8}$$

For the force F_i to be a good approximation to the gradient of the density gradient, $\mathbb{L}^{(n)}$ must be a unit tensor. Therefore, the weights are normalized such that $e_2 = 1$. For the standard D2Q9 lattice the weights are given as

$$\begin{gathered} w(1) = \frac{1}{3}, \qquad w(2) = \frac{1}{12}, \qquad w(|\boldsymbol{\xi}_\alpha|^2) = 0 \text{ for } |\boldsymbol{\xi}_\alpha|^2 > 2, \\ e_4 = \frac{1}{3} \end{gathered} \tag{6.9}$$

Once the form of the pseudopotential force and the appropriate weights have been determined, a correction to the ideal-state equation induced by the pseudopotential to obtain the correct form of the pressure tensor and ensure mechanical stability condition is satisfied at the interface is in order.

In continuum, the pressure tensor P_{ij}^{c} can be defined as follows (Benzi et al., 2006; Sbragalia 2007; Li et al., 2013):

$$\partial_j P_{ij}^{c} = \partial_j (c_s^2 \rho)\delta_{ij} - F_i \tag{6.10}$$

Subsequently, the leading terms of the interaction force F_i can be obtained from the Taylor expansion in Eq. (6.3)

$$F_i = -Gc^2 \left[e_2 \psi \boldsymbol{\nabla} \psi + \frac{e_4 c^2}{2} \psi \boldsymbol{\nabla}(\nabla^2 \psi) + \ \dots \right] \tag{6.11}$$

Which can be further simplified as shown below

$$\begin{aligned} F_i &= -Gc^2 \left[e_2 \psi \boldsymbol{\nabla} \psi + \frac{e_4 c^2}{2} \psi \boldsymbol{\nabla}(\nabla^2 \psi) + \ \dots \right] \\ &= -\frac{Gc^2 e_2}{2} \boldsymbol{\nabla} \psi^2 - \frac{Gc^4 e_4}{2} [\boldsymbol{\nabla}(\psi \nabla^2 \psi) - \nabla^2 \psi \boldsymbol{\nabla} \psi] + \ \dots \\ &= -\frac{Gc^2 e_2}{2} \boldsymbol{\nabla} \psi^2 - \frac{Gc^4 e_4}{2} \boldsymbol{\nabla}(\psi \nabla^2 \psi) \\ &\quad + \frac{Gc^4 e_4}{2} \left[\boldsymbol{\nabla} \cdot (\boldsymbol{\nabla} \psi \boldsymbol{\nabla} \psi) - \frac{1}{2} \boldsymbol{\nabla} |\boldsymbol{\nabla} \psi|^2 \right] + \ \dots \end{aligned} \tag{6.12}$$

To obtain the continuum form of the pressure tensor P_{ij}, Eq. (6.12) can be substituted in Eq. (6.10)

$$\begin{aligned} P_{ij}^{c} = &\left(c_s^2 \rho + \frac{Gc^2 e_2}{2} \psi^2 + \frac{Gc^4 e_4}{4} |\boldsymbol{\nabla} \psi|^2 + \frac{Gc^4 e_4}{2} \psi \nabla^2 \psi \right) \delta_{ij} \\ &- \frac{Gc^4 e_4}{2} \boldsymbol{\nabla} \psi \boldsymbol{\nabla} \psi + O(\partial^4) \end{aligned} \tag{6.13}$$

It is instructive to note that, there is always a degree of arbitrariness in the derivation above because there exists a sort of gauge invariance in the definition of the pressure tensor (Rowlinson, 1982). In addition, the derivation involves imposing the constraint in Eq. (6.10) while the Taylor expansion of the force field is verified up to second order. Consequently, the integration of approximate force field may not guarantee exact mechanical balance. Therefore, Shan (2008) outlined a general approach, using the discrete form of the pressure tensor, that can guarantee exact mechanical balance. Next, we provide brief detail of Shan (2008) approach.

To derive the discrete form of the pressure tensor, consider an infinitesimal surface dA_j, then take the differential force dF_i as the interaction force through dA_j. Since the interaction pressure tensor can be defined as the momentum transfer rate through an area of surface, P_{ij} can be defined as:

$$-P_{ij}dA_j = dF_i \tag{6.14}$$

That is, given an infinitesimal surface element dA_j and taking the differential force dF_i as the interaction force acting across dA_j. The P_{ij} can be defined as the momentum transfer rate through the surface dA_j

Integrating over a closed volume

$$-\oint P_{ij}dA_j = \int F_i d\Omega \tag{6.15}$$

And applying the gauss integration theorem be obtain

$$-\sum P_{ij}A_j = \sum F_i \tag{6.16}$$

Now the discrete form of the pressure tensor can be expressed as (Shan, 2008; Sbragaglia and Shan, 2011)

$$P_{ij} = c_s^2 \rho \delta_{ij} + \frac{G}{2} \psi(\boldsymbol{x}) \sum_{\alpha} w(|\xi_{i\alpha}|^2) \psi(\boldsymbol{x} + \boldsymbol{x}') \xi_{i\alpha} \xi_{j\alpha} \tag{6.17}$$

In other to calculate the density profile and the surface tension, we considered Eq. (6.17) and its generalization (Shan, 2008) and apply it to the case of nearest-neighbor interaction. Applying Taylor expansion to Eq. (6.17) yields

$$P_{ij} = \left(c_s^2 \rho + \frac{Gc^2}{2} \psi^2 + \frac{Gc^4}{12} \psi \nabla^2 \psi \right) \delta_{ij} + \frac{Gc^4}{6} \psi \boldsymbol{\nabla\nabla} \psi \tag{6.18}$$

Now for a flat interface and let us suppose that the interface develops along the x-direction in a two-phase equilibrium system. The condition for mechanical stability implies that the normal component remain constant and equal to the bulk pressure P_0 (Shan and Chen 1994; Shan, 2008). Hence, the normal pressure tensor can be written as

$$P_o = P_{xx} = c_s^2 \rho + \frac{Gc^2}{2} \psi^2 + \frac{Gc^4}{12} \left(\alpha \left(\frac{d\psi}{dx} \right)^2 + \beta \psi \frac{d^2 \psi}{dx^2} \right) \tag{6.19}$$

where $\alpha = 1 - 3e_4$ and $\beta = 1 + 6e_4$. For the case of nearest-neighbor $e_4 = {}^1\!/_3$

Using the relation

$$\frac{1}{2} \frac{d}{d\psi} \left(\frac{d\psi}{dx} \right)^2 = \frac{d^2 \psi}{dx^2} \tag{6.20}$$

And making the change of variable $\varphi = \left(\frac{d\psi}{dx} \right)^2$

$$\alpha \varphi + \frac{\beta}{2} \psi \frac{d\varphi}{d\psi} = \frac{\beta}{2} \psi^{1+\varepsilon} \frac{d(\psi^{-\varepsilon} \varphi)}{d\psi} = \frac{\beta}{2} \frac{\psi^{1+\varepsilon}}{\psi'} \frac{d}{d\rho} \left[\frac{\psi'^2}{\psi^{\varepsilon}} \left(\frac{d\rho}{dx} \right)^2 \right] \tag{6.21}$$

With $\varepsilon = -{}^{2\alpha}/_{\beta}$ and $\psi' = \frac{d\psi}{d\rho}$

one can rewrite the mechanical equilibrium as an ordinary differential equation as

$$P_0 = c_s^2\rho + \frac{Gc^2}{2}\psi^2 + \frac{Gc^4\beta}{24}\,\frac{\psi^{1+\varepsilon}}{\psi'}\frac{d}{d\rho}\left[\frac{\psi'^2}{\psi^\varepsilon}\left(\frac{d\rho}{dn}\right)^2\right] \tag{6.22}$$

Eq. (6.22) can be rearranged as

$$\left(P_0 - c_s^2\rho - \frac{Gc^2}{2}\psi^2\right)\frac{24}{Gc^4\beta}\frac{\psi'}{\psi^{1+\varepsilon}} = \frac{d}{d\rho}\left[\frac{\psi'^2}{\psi^\varepsilon}\left(\frac{d\rho}{dn}\right)^2\right] \tag{6.23}$$

Integrating yields

$$\frac{24}{Gc^4\beta}\int_{\rho_g}^{\rho_l}\left(P_0 - c_s^2\rho - \frac{Gc^2}{2}\psi^2\right)\frac{\psi'}{\psi^{1+\varepsilon}}d\rho = \int_{\rho_g}^{\rho_l} d\left[\frac{\psi'^2}{\psi^\varepsilon}\left(\frac{d\rho}{dn}\right)^2\right] \tag{6.24}$$

$$\frac{24}{Gc^4\beta}\int_{\rho_g}^{\rho_l}\left(P_0 - c_s^2\rho - \frac{Gc^2}{2}\psi^2\right)\frac{\psi'}{\psi^{1+\varepsilon}}d\rho = \frac{\psi'^2}{\psi^\varepsilon}\left(\frac{d\rho}{dn}\right)^2\Bigg|_{\rho_g}^{\rho_l} \tag{6.25}$$

The equation of state in both phases can be expressed as

$$P_0(\rho_l) = c_s^2\rho_l + \frac{Gc^2}{2}\psi(\rho_l)^2\,, \qquad P_0(\rho_g) = c_s^2\rho_g + \frac{Gc^2}{2}\psi(\rho_g)^2 \tag{6.26}$$

Therefore $\left(\frac{d\rho}{dn}\right) = 0$ in each single-phase region and

$$\frac{\psi'^2}{\psi^\varepsilon}\left(\frac{d\rho}{dn}\right)^2\Bigg|_{\rho_g}^{\rho_l} = 0 \tag{6.27}$$

Finally, we obtain the relation below for the mechanical stability condition

$$\int_{\rho_g}^{\rho_l}\left(P_0 - c_s^2\rho - \frac{Gc^2}{2}\psi^2\right)\frac{\psi'}{\psi^{1+\varepsilon}}d\rho = 0 \tag{6.28}$$

The combination of the Eq. (6.28) and the conditions in Eq. (6.26) can be used to solve for P_0, ρ_l and ρ_g via numerical integration to arbitrary precision.

The surface tension can be defined as the integral along the coordinate normal to the interface of the mismatch between the normal and transverse components of the pressure tensor (Rowlinson, 1982).

$$\begin{aligned}\sigma = \int_{-\infty}^{\infty}(P_0 - P_T)dx &= \int_{-\infty}^{\infty}(P_{xx} - yy)dx \\ &= \frac{e_4Gc^4}{2}\int_{-\infty}^{\infty}|\partial_x\psi|^2dx\end{aligned} \tag{6.29}$$

To be consistent with the thermodynamic equation of state (Eq. 6.26), Yuan and Schaefer (2006) redefined the pseudopotential function as

$$\psi = \sqrt{\frac{2(P_0 - \rho c_s^2)}{Gc^2}} \tag{6.30}$$

With this definition of the pseudopotential function, different EOS can be incorporated into the pseudopotential model. We will use the Carnahan-Starling (Carnahan and Starling 1970a) equation of state (CS-EOS) shown below in our single component multiphase (SCMP) simulations.

$$p = \rho RT\,\frac{1 + {}^{b\rho}/_{4} + \left({}^{b\rho}/_{4}\right)^2 - \left({}^{b\rho}/_{4}\right)^3}{\left(1 - {}^{b\rho}/_{4}\right)^3} - a\rho^2 \tag{6.31}$$

where $a = 0.4963(RT_c)^2/P_c$, $b = 0.1873RT_c/P_c$. Here we set $a = 1$ and $b = 4$

Therefore, the critical temperature and pressure are $T_c = 0.094$ and $P_c = 0.0044$ repsecitvely. Next, we verify if the SCMP LB model with CS-EOS described above can reproduce the correct liquid and vapor densities corresponding to different temperatures as given by the Maxwell construction. In this study, we used the Exact-Difference-Method (EDM) Kupershtokh et al., (2009) scheme described in chapter five to incorporate the forcing term as shown below

$$\mathrm{F}_\alpha = f_\alpha^{eq}(\rho, \mathbf{u} + \Delta\mathbf{u}) - f_\alpha^{eq}(\rho, \mathbf{u}) \tag{6.32}$$

where $\mathbf{u} = {\sum_\alpha f_\alpha \boldsymbol{\xi}_\alpha}/{\rho}$ and $\Delta\mathbf{u} = {\mathbf{F}\delta_t}/{\rho}$

F in this case is the total force acting on a fluid particle in multiphase flow and it is given as:

$$\mathbf{F} = \boldsymbol{F}_f + \boldsymbol{F}_s + \boldsymbol{F}_e \tag{6.33}$$

Also, the actual fluid velocity for EDM scheme is defined as

$$\bar{\mathbf{v}} = \mathbf{u} + {\delta_t \mathbf{F}}/{2\rho}$$

We considered the case of a flat surface with the computational domain given as $\mathrm{N}_x \times \mathrm{N}_y \times \mathrm{N}_z = 101 \times 201 \times 101$. Periodic boundary condition was set for all boundaries and the region $0 \leq y \leq 100$ is filled with gas while the rest is filled with liquid. The density field was initialized as

$$\rho(y) = \rho_g + \frac{\rho_l - \rho_g}{2} \times \left[\tanh\left(\frac{2(y-100)}{W}\right)\right] \tag{6.34}$$

where W is the initial interface thickness and it is chosen as 5 lattice units. We compared our results to the ones in Huang et al. (2011) and observe good agreement (Table 6.1).

Table 6.1. Density ratios obtained for CS-EOS at different temperatures $\tau = 0.6$

T/Tc	ρ_l / ρ_g	ρ_l / ρ_g **Huang et al., (2011)**	ρ_l / ρ_g **Analytical**
0.95	0.2098/0.06576	0.2099/0.06583	0.2097/0.06553
0.90	0.2473/0.04368	0.2475/0.04380	0.2471/0.04299
0.85	0.2783/0.02997	0.2786/0.02912	0.2781/0.02781
0.80	0.3061/0.01838	0.3065/0.01854	0.3060/0.01674

6.2 Proposed Pseudo-Potential-Based Fluid-Solid Interaction

Near a solid node, there exist an adhesion force $\boldsymbol{F}_s$ between the fluid and the solid. There are generally two classes of implementations of this adhesion force, namely: density-based interaction (Martys and Chen 1996) and pseudopotential-based interaction (Raiskinmaki et al., 2002). In a recent study, Li et al., (2014) compared these different methods and proposed a modified pseuodopotential-based method that is defined as:

$$\boldsymbol{F}_s = -G_w \psi(x) \sum_{\alpha} w(|\xi_\alpha|^2) S(\boldsymbol{x} + \boldsymbol{\xi}_\alpha) \boldsymbol{\xi}_\alpha \tag{6.35}$$

where G_w is the absorption parameter, $S(\boldsymbol{x} + \boldsymbol{\xi}_\alpha) = \phi(x) s(\boldsymbol{x} + \boldsymbol{\xi}_\alpha)$ is the switch function. Note that $s(\boldsymbol{x} + \boldsymbol{\xi}_\alpha)$ is equal to 0 or 1 for a fluid or solid phase respectively. In Li et al. (2014), the choice of $\phi(x)$ is $\phi(x) = \psi(x)$ where $\psi(x)$ is the effective mass at the boundary fluid node. Here we propose another modified model that introduces a virtual effective mass on the solid boundary node as follows:

$$S(\boldsymbol{x}+\ \boldsymbol{\xi}_{\alpha}) = \ \phi(x+\ \boldsymbol{\xi}_{\alpha})s(\boldsymbol{x}+\ \boldsymbol{\xi}_{\alpha}) \tag{6.36}$$

such that $\phi(x+\ \boldsymbol{e}_{\alpha})$ is equal to 0 for a fluid node and $\phi(x+\ \boldsymbol{e}_{\alpha}) =$ $\psi_{virutal}\left(\rho_{virtual}^{avg}(\boldsymbol{x}_s)\right)$ for a solid node and $\rho_{virtual}^{avg}(\boldsymbol{x}_s) = \frac{1}{N_f}\sum_{\alpha_f}\rho\left(\boldsymbol{x}_s+\ \boldsymbol{\xi}_{\alpha_f}\right)$

where $\boldsymbol{x}_s$ is the site of the solid node, N_f is the number of fluid nodes that directly connect to the solid node side and α_f are all indices α for which $\boldsymbol{x}_s+\ \boldsymbol{\xi}_{\alpha}$ is a boundary fluid node.

We then evaluated the proposed model for pseudo-potential based adhesion interaction force against the model proposed in (Li et al., 2014) in terms of density variation near the wall. In this simulation, we adopted a $\mathrm{N}_x \times \mathrm{N}_y \times \mathrm{N}_z = 101 \times 201\times 101$ lattice. No-slip boundary conditions were applied in all three directions and no body force was applied. The initial density field was initialized as shown in Eq. (6.34).

The parameter G_w is adjusted to simulate identical contact angles in both models. From Fig. 6.1, our result shows no deviation in the profile of the density variation near the boundary fluid node for the liquid phase. However, in the vapor phase, we noticed some variation in the magnitude of the vapor density. Our proposed model produced a lower vapor density. In our proposed model the ratio of the liquid density to the vapor density is (0.3057/0.0182) while in the Li et al. (2014) model the ratio is (0.3057/0.0193). Therefore, in the next chapter we used the model proposed in Eq. 6.36

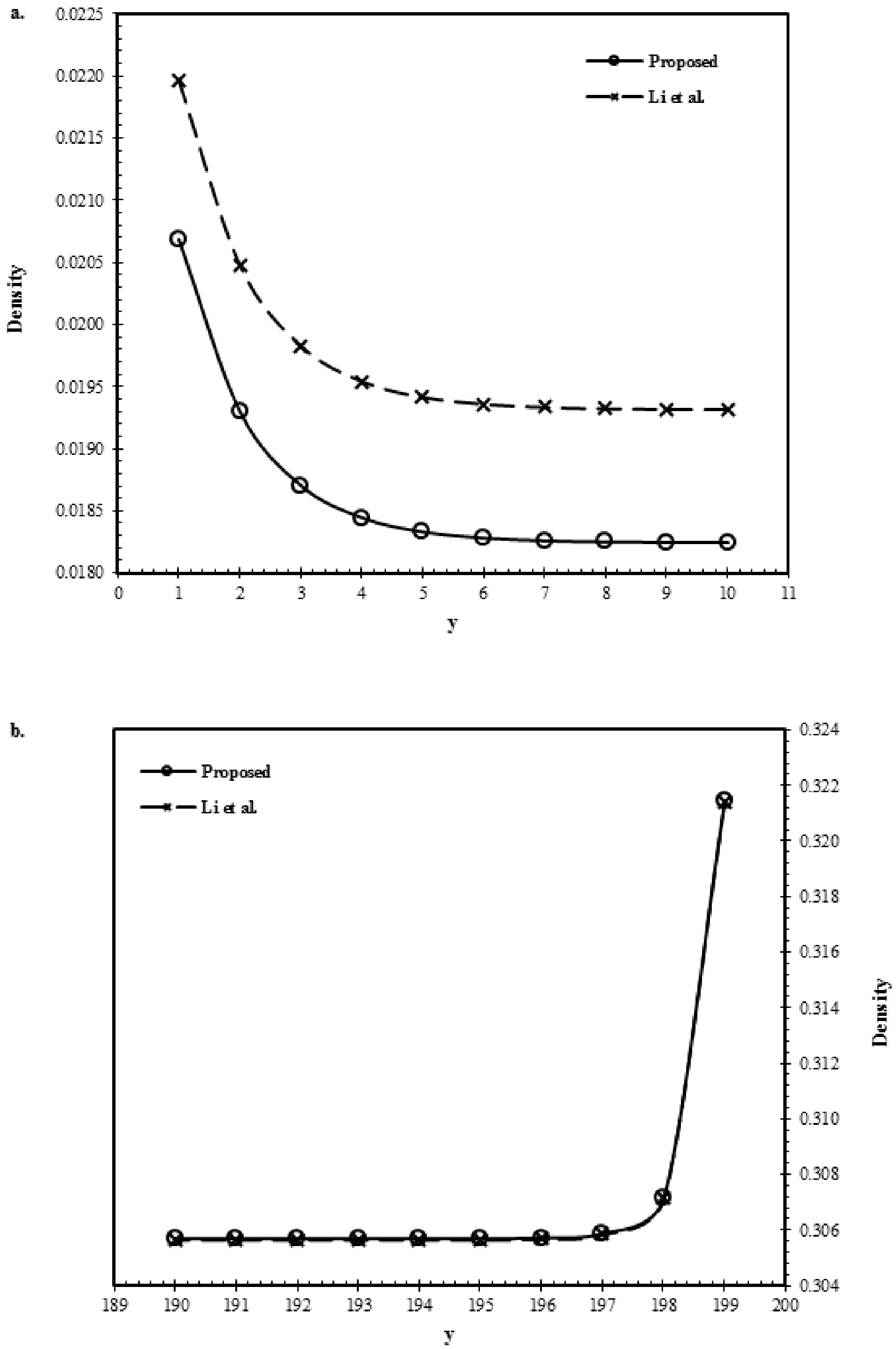

Fig. 6.1 Comparison of density variation on the fluid boundary node for our proposed model and Li et al. (2014). (a) Vapor phase (b) Liquid phase

6.3 Multi-Relaxation Lattice Boltzmann Equation

In the preceding section, we presented corrections to the ideal equations of state for nonideal fluids. In addition, we also presented a detailed derivation of the mechanical stability condition and Yuan-Schaefer (2006) scheme for incorporating different equations of state. We ended the section by verifying that C-S EOS can be used to simulate different density ratios and proposing a modified scheme for incorporating fluid-solid interaction force. Here, 15-velocity three-dimensional MRT model is adopted and we present the Chapman-Enskog multiscale analysis for the model (Xu et al., 2015).

The discrete velocity set for the three-dimensional, fifteen-velocity (D3Q15) model is given as

$$\begin{aligned}\boldsymbol{\xi_\alpha} &= \left\{|\xi_x\rangle, \left|\xi_y\right\rangle, |\xi_z\rangle, \right\} \\ &= c\begin{bmatrix} 0 & 1 & -1 & 0 & 0 & 0 & 0 & 1 & -1 & 1 & -1 & 1 & -1 & 1 & -1 \\ 0 & 0 & 0 & 1 & -1 & 0 & 0 & 1 & 1 & -1 & -1 & 1 & 1 & -1 & -1 \\ 0 & 0 & 0 & 0 & 0 & 1 & -1 & 1 & 1 & 1 & 1 & -1 & -1 & -1 & -1 \end{bmatrix}\end{aligned} \tag{6.37}$$

We consider, in a concise vector form, the evolution equation with a source term that incorporates molecular interaction that can model interfacial dynamics such as phase segregation and surface tension,

$$\begin{aligned}&|f(\boldsymbol{x} + \boldsymbol{\xi}_\alpha \delta_t, t + \delta_t)\rangle - |f(\boldsymbol{x}, t)\rangle \\ &\qquad = -\boldsymbol{\Lambda}\left(|f(\boldsymbol{x}, t)\rangle - |f^{eq}(\boldsymbol{x}, t)\rangle\right) + \delta_t \left(\mathbf{I} - \frac{1}{2}\boldsymbol{\Lambda}\right)|\mathrm{F}\rangle\end{aligned} \tag{6.38}$$

where we have used the Dirac notation of bra ket $|\cdot\rangle$ vectors to denote column vector. In addition,

$|f(\boldsymbol{x}+\boldsymbol{\xi}_{\alpha}\delta_t, t+\delta_t)\rangle = [f(\boldsymbol{x}+\boldsymbol{\xi}_0\delta_t, t+\delta_t), f(\boldsymbol{x}+\boldsymbol{\xi}_1\delta_t, t+\delta_t),$ $\dots, f(\boldsymbol{x}+\boldsymbol{\xi}_{14}\delta_t, t+\delta_t)]^{\mathrm{T}}$ is the vector of the state after advection

$|f(\boldsymbol{x},t)\rangle = [f_0(\boldsymbol{x},t), f_1(\boldsymbol{x},t), \dots, f_{14}(\boldsymbol{x},t)]^{\mathrm{T}}$ is vector of the distribution function of velocity $\boldsymbol{\xi}_{\alpha}$ at location $\boldsymbol{x}$ and time t.

$|f^{eq}(\boldsymbol{x},t)\rangle = [{f_0}^{eq}(\boldsymbol{x},t), {f_1}^{eq}(\boldsymbol{x},t), \dots, {f_{14}}^{eq}(\boldsymbol{x},t)]^{\mathrm{T}}$ is the vector of the equilibrium distribution function and $\boldsymbol{\Lambda}$ is the collision matrix.

The left-hand side and right-hand side of Eq. (6.37) represents the streaming and collision steps of the evolution of the lattice Boltzmann equation. Here the collision is accomplished through a generalized relaxation process such that the distribution function can approach the local equilibrium values at characteristic relaxation time scales given by a collision matrix (Premnath and Abraham, 2007). It is noteworthy that the LBGK model is a special case in which the collision matrix is a diagonal matrix with elements $1/\tau$ where τ is the dimensionless relaxation matrix (He et al. 1998).

The equilibrium distribution function can be obtained from a Taylor series expansion of the Maxwell-Boltzmann distribution in terms of fluid velocity $\mathbf{u}$ (He et al., 1997) and it is given by

$$f_{\alpha}^{eq} = \omega_{\alpha}\rho\left[1 + \frac{\mathbf{u}\cdot\boldsymbol{\xi}_{\alpha}}{c_s^2} + \frac{\mathbf{uu}\colon(\boldsymbol{\xi}_{\alpha}\boldsymbol{\xi}_{\alpha} - c_s^2\boldsymbol{I})}{2c_s^4}\right] \tag{6.39}$$

The source term F_{α} is used to model interfacial dynamics and it is defined as (Premnath and Abraham, 2007)

$$\mathrm{F}_{\alpha} = \omega_{\alpha}\left[\frac{(\boldsymbol{\xi}_{\alpha} - \mathbf{v})}{c_s^2} + \frac{(\boldsymbol{\xi}_{\alpha}\cdot\mathbf{v})}{2c_s^4}\boldsymbol{\xi}_{\alpha}\right]\cdot\mathbf{F} \tag{6.40}$$

Next, we will use the generalized lattice Boltzmann model introduced by (D'Humieres, 1992). In this approach, the collision step will be executed in moment space that is constructed from the distribution function through a transform matrix. This transform matrix comprises of linearly independent set of vectors (details will be provided later in this chapter). The choice of performing the collision in moment space is predicated on the understanding, from kinetic theory, that physical processes in fluids can be approximately described by interaction among modes of the collision operator and that these modes are related to the moments. For example, the hydrodynamic modes are linear combinations of mass and momenta moments (Lallemand and Luo, 2000). Hence, moment representation provides a convenient way of incorporating the physics into the lattice Boltzmann equation. Below we rewrite the evolution equation in moment space.

$$\begin{aligned} &|f(\boldsymbol{x}+\boldsymbol{\xi}_\alpha \delta_t, t+\delta_t)\rangle - |f(\boldsymbol{x},t)\rangle \\ &\qquad = -\mathbf{M}^{-1}\Big[\widehat{\boldsymbol{\Lambda}}\left(\left|\hat{f}(\boldsymbol{x},t)\right\rangle - \left|\hat{f}^{eq}(\boldsymbol{x},t)\right\rangle\right) \\ &\qquad + \delta_t\left(\mathbf{I}-\frac{1}{2}\widehat{\boldsymbol{\Lambda}}\right)\left|\hat{\mathrm{F}}\right\rangle\Big] \end{aligned} \tag{6.41}$$

In the above equation, the advection and collision steps are executed in the velocity and moment space respectively. This is done so that the time scales of the various processes can be controlled independently since all the modes of the collision operator are orthogonal. The transform matrix $\mathbf{M}$ comprises of linearly independent set of vectors that is used to transform a vector in the vector space spanned by the discrete velocities into a vector in the vector space spanned by the velocity moments of the discrete distribution function per the following linear mapping

$$\left|\hat{f}\right\rangle = \mathbf{M}|f\rangle \text{ and } |f\rangle = \mathbf{M}^{-1}\left|\hat{f}\right\rangle \tag{6.42}$$

Considering that our desire is to reduce the collision matrix to the appropriate diagonal form shown below,

$$\widehat{\mathbf{\Lambda}} = diag\left[S_\rho, S_e, S_\epsilon, S_j, S_q, S_j, S_q, S_j, S_q, S_\nu, S_\nu, S_\nu, S_\nu, S_\nu, S_{xyz}\right] \tag{6.43}$$

an orthogonal transform matrix can be constructed to comprise of normalized orthogonal dual basis set (D'Humieres, 1992). This basis set can be obtained by applying the Gram-Schmidt orthogonaliztion procedure to the monomials of the Cartesian components of the discrete velocities. Details of this procedure can be found in (Lallemand and Luo, 2003). We provide the results for the components of the corresponding 15 orthogonal basis column vectors for the 3D cubic lattice with 15 discrete velocities below

$$|\rho\rangle_\alpha = |\boldsymbol{\xi}_\alpha|^0 \tag{6.44a}$$

$$|e\rangle_\alpha = |\boldsymbol{\xi}_\alpha|^2 - 2 \tag{6.44b}$$

$$|\epsilon\rangle_\alpha = \frac{1}{2}(15|\boldsymbol{\xi}_\alpha|^4 - 55|\boldsymbol{\xi}_\alpha|^2 + 32) \tag{6.44c}$$

$$|j_x\rangle_\alpha = \xi_{\alpha x} \tag{6.44d}$$

$$|q_x\rangle_\alpha = \frac{1}{2}(5|\boldsymbol{\xi}_\alpha|^2 - 13)\xi_{\alpha x} \tag{6.44e}$$

$$\left|j_y\right\rangle_\alpha = \xi_{\alpha y} \tag{6.44f}$$

$$\left|q_y\right\rangle_\alpha = \frac{1}{2}(5|\boldsymbol{\xi}_\alpha|^2 - 13)\xi_{\alpha y} \tag{6.44g}$$

$$|j_z\rangle_\alpha = \xi_{\alpha z} \tag{6.44h}$$

$$|q_z\rangle_\alpha = \frac{1}{2}(5|\boldsymbol{\xi}_\alpha|^2 - 13)\xi_{\alpha z} \tag{6.44i}$$

$$|p_{xx}\rangle_\alpha = 3{\xi_{\alpha x}}^2 - |\boldsymbol{\xi}_\alpha|^2 \tag{6.44j}$$

$$|p_{ww}\rangle_\alpha = {\xi_{\alpha y}}^2 - {\xi_{\alpha z}}^2 \tag{6.44k}$$

$$|p_{xy}\rangle_\alpha = \xi_{\alpha x}\xi_{\alpha y} \tag{6.44l}$$

$$|p_{yz}\rangle_\alpha = \xi_{\alpha y}\xi_{\alpha z} \tag{6.44m}$$

$$|p_{zx}\rangle_\alpha = \xi_{\alpha z}\xi_{\alpha x} \tag{6.44n}$$

$$|m_{xyz}\rangle_\alpha = \xi_{\alpha x}\xi_{\alpha y}\xi_{\alpha z} \tag{6.44o}$$

The above components of the orthogonal basis column vectors form the transform matrix. Each basis vector has an explicit physical significance related to the moments of f_α in the discrete velocity space. For example, $|\rho\rangle$ is the mode related to the density; $|e\rangle$ is the mode related to the kinetic energy; $|\epsilon\rangle$ is the mode related to the kinetic energy square; $|j_x\rangle$, $|j_y\rangle$, $|j_z\rangle$ are the modes related to the x, y, z components of the momentum respectively; $|q_x\rangle$, $|q_y\rangle$, $|q_z\rangle$ are the modes related to the x, y, z components of the energy flux; $|p_{xx}\rangle$, $|p_{ww}\rangle$, $|p_{xy}\rangle$, $|p_{yz}\rangle$, $|p_{zx}\rangle$ are the modes corresponding to the diagonal and off-diagonal components of the symmetric traceless viscous stress tensor; and finally $|m_{xyz}\rangle$ the mode related anti-symmetric third-order moment.

For the case where $c = 1$ (i.e. unit lattice and time step), the simplified form of the transform matrix is given a

$$\mathbf{M} =$$

$$\begin{bmatrix}
1 & 1 & 1 & 1 & 1 & 1 & 1 & 1 & 1 & 1 & 1 & 1 & 1 & 1 & 1 \\
-2 & -1 & -1 & -1 & -1 & -1 & -1 & 1 & 1 & 1 & 1 & 1 & 1 & 1 & 1 \\
16 & -4 & -4 & -4 & -4 & -4 & -4 & 1 & 1 & 1 & 1 & 1 & 1 & 1 & 1 \\
0 & 1 & -1 & 0 & 0 & 0 & 0 & 1 & -1 & 1 & -1 & 1 & -1 & 1 & -1 \\
0 & -4 & 4 & 0 & 0 & 0 & 0 & 1 & -1 & 1 & -1 & 1 & -1 & 1 & -1 \\
0 & 0 & 0 & 1 & -1 & 0 & 0 & 1 & 1 & -1 & -1 & 1 & 1 & -1 & -1 \\
0 & 0 & 0 & -4 & 4 & 0 & 0 & 1 & 1 & -1 & -1 & 1 & 1 & -1 & -1 \\
0 & 0 & 0 & 0 & 0 & 1 & -1 & 1 & 1 & 1 & 1 & -1 & -1 & -1 & -1 \\
0 & 0 & 0 & 0 & 0 & -4 & 4 & 1 & 1 & 1 & 1 & -1 & -1 & -1 & -1 \\
0 & 2 & 2 & -1 & -1 & -1 & -1 & 0 & 0 & 0 & 0 & 0 & 0 & 0 & 0 \\
0 & 0 & 0 & 1 & 1 & -1 & -1 & 0 & 0 & 0 & 0 & 0 & 0 & 0 & 0 \\
0 & 0 & 0 & 0 & 0 & 0 & 0 & 1 & -1 & -1 & 1 & 1 & -1 & -1 & 1 \\
0 & 0 & 0 & 0 & 0 & 0 & 0 & 1 & 1 & -1 & -1 & -1 & -1 & 1 & 1 \\
0 & 0 & 0 & 0 & 0 & 0 & 0 & 1 & -1 & 1 & -1 & -1 & 1 & -1 & 1 \\
0 & 0 & 0 & 0 & 0 & 0 & 0 & 1 & -1 & -1 & 1 & -1 & 1 & 1 & -1
\end{bmatrix} \tag{6.45}$$

The main challenge in using lattice Boltzmann equation to simulate isotropic fluid is how to make the flow independent of the symmetry of the underlying lattice structure (Luo and Lellamand, 2000). Although the collision process does not change the conserved modes, however, the non-conserved modes are affected and they in turn causes changes in the fluxes of some of the conserved modes (Lellemand and Luo, 2003). Hence, to obtain the equilibrium functions that are equivalent to the Taylor series expansion of the Maxwell-Boltzmann equilibrium distribution function in velocity space, we need to obtain the values of the coupling parameters for these non-conserved modes that will optimize the isotropy and the Gallilean invariance of the model. Details of this process are described in (Lellemand and Luo, 2000). In what follows, we provide a summary of this process. Firstly, we assumed that the non-conserved moments relax linearly towards the equilibrium values that are functions of the conserved moments. We provide the relaxation equation for the non-conserved moments below (Lellenad and Luo, 2003)

$$e^{*} = e - s_{e}\left[e - e^{(eq)}\right] \tag{6.46a}$$

$$\epsilon^{*} = \epsilon - s_{\epsilon}\left[\epsilon - \epsilon^{(eq)}\right] \tag{6.46b}$$

$$q_x^{*} = q_x - s_q\left[q_x - {q_x}^{(eq)}\right] \tag{6.46c}$$

$$q_y^{*} = q_y - s_q\left[q_y - {q_y}^{(eq)}\right] \tag{6.46d}$$

$$q_z^{*} = q_z - s_q\left[q_z - {q_z}^{(eq)}\right] \tag{6.46e}$$

$$p_{xx}^{*} = p_{xx} - s_v\left[p_{xx} - {p_{xx}}^{(eq)}\right] \tag{6.46f}$$

$$p_{ww}^{*} = p_{ww} - s_v\left[p_{ww} - {p_{ww}}^{(eq)}\right] \tag{6.46g}$$

$$p_{xy}^{*} = p_{xy} - s_v\left[p_{xy} - {p_{xy}}^{(eq)}\right] \tag{6.46h}$$

$$p_{yz}^{*} = p_{yz} - s_v\left[p_{yz} - {p_{yz}}^{(eq)}\right] \tag{6.46i}$$

$$p_{xz}^{*} = p_{xz} - s_v\left[p_{xz} - {p_{xz}}^{(eq)}\right] \tag{6.46j}$$

Note that the quantities with and without superscript * represent the post and pre-collision values, respectively. Furthermore, the form of the equilibrium values of the non-conserved modes need to be chosen based on the corresponding moments obtained from transform matrix and the equilibrium distribution function in velocity space. However, this values should satisfy the symmetry of the problem. Hence, the optimal values of the coupling parameters are obtained via the mode analysis of the dispersion equation (Lellemand and Luo, 2000). The non-conserved moments obtained from the linear analysis are as follows

$$e^{eq} = -1 + |\mathbf{u}| \tag{6.47a}$$

$$\epsilon^{eq} = 1 - 5|\mathbf{u}| \tag{6.47b}$$

$$q_x^{eq} = -\frac{7}{3}u_x \tag{6.47c}$$

$$q_y^{eq} = -\frac{7}{3}u_y \tag{6.47d}$$

$$q_z^{eq} = -\frac{7}{3}u_z \tag{6.47e}$$

$$3p_{xx}^{eq} = 2u_x^2 - u_y^2 - u_z^2 \tag{6.47f}$$

$$p_{ww}^{eq} = u_y^2 - u_z^2 \tag{6.47g}$$

$$p_{xy}^{eq} = u_x u_y \tag{6.47h}$$

$$p_{yz}^{eq} = u_y u_z \tag{6.47i}$$

$$p_{xz}^{eq} = u_x u_z \tag{6.47j}$$

$$m_{xyz}^{eq} = 0 \tag{6.47k}$$

where the kinematic viscosity ν and the bulk viscosity ζ of the model are

$$\nu = \frac{1}{3}\left(\frac{1}{s_\nu} - \frac{1}{2}\right)\delta_t \tag{6.48}$$

$$\zeta = \frac{2}{9}\left(\frac{1}{s_e} - \frac{1}{2}\right)\delta_t \tag{6.49}$$

6.3.1 Improved Forcing Term

Recall the general forcing scheme,

$$\mathrm{F}_{\alpha} = \omega_{\alpha}\left[\frac{\mathbf{B}\cdot\boldsymbol{\xi}_{\boldsymbol{\alpha}}}{c_s^2} + \frac{\mathbf{C}\colon(\boldsymbol{\xi}_{\boldsymbol{\alpha}}\boldsymbol{\xi}_{\boldsymbol{\alpha}} - c_s^2\mathbf{I})}{2c_s^4}\right] \tag{6.50}$$

$$\mathbf{B} = B_e\mathbf{F}, \qquad \mathbf{C} = C_e(\mathbf{vF} + \mathbf{vF}^{\mathrm{T}}), \quad C_e = B_e = \left(1 - \frac{1}{2\tau}\right) \tag{6.51}$$

Recovered macroscopic equation is of the form,

$$\frac{\partial\rho}{\partial t} + \frac{\partial(\rho\mathbf{u})}{\partial\boldsymbol{x}} = \delta t\left(m - \frac{1}{2}\right)\frac{\partial\mathbf{F}}{\partial\boldsymbol{x}} \tag{6.52}$$

$$\begin{aligned}\frac{\partial(\rho\mathbf{u})}{\partial t} + \frac{\partial(\rho\mathbf{uu})}{\partial\boldsymbol{x}} \\ &= -\frac{\partial(c_s^2\rho)}{\partial\boldsymbol{x}} + \boldsymbol{F} - \epsilon\delta_t\left(m - \frac{1}{2}\right)\frac{\partial\mathbf{F}}{\partial t_1} \\ &+ \frac{\partial}{\partial\boldsymbol{x}}\left[\rho\nu\left(\frac{\partial\mathbf{u}}{\partial\boldsymbol{x}} + \left(\frac{\partial\mathbf{u}}{\partial\boldsymbol{x}}\right)^T\right)\right] \\ &- \delta t\frac{\partial}{\partial\boldsymbol{x}}\left[\left(\tau - \frac{1}{2}\right)(\mathbf{uF} + \mathbf{uF}^{\mathbf{T}}) - \tau C_e(\mathbf{vF} + \mathbf{vF}^{\mathrm{T}})\right]\end{aligned} \tag{6.53}$$

where, $\mathbf{u} = \sum_{\alpha} f_{\alpha}\boldsymbol{e}_{\boldsymbol{\alpha}} + m\delta_t\mathbf{F}$ is the velocity used in the equilibrium function and $\mathbf{v}$ is the velocity used in the forcing term.

For Guo et al. (2002) from chapter 5, Eq. (5.78), the velocities used in the equilibrium function $\mathbf{u}$, the forcing term $\mathbf{v}$ and overall fluid velocity $\bar{\mathbf{v}}$ are identical and it is given as

$$\bar{\mathbf{v}} = \mathbf{v} = \mathbf{u} = \sum_{\alpha} f_{\alpha} \boldsymbol{e}_{\boldsymbol{\alpha}} + \frac{1}{2}\delta_t \mathbf{F}$$

$$C_e = B_e = \left(1 - \frac{1}{2\tau}\right) \tag{6.54}$$

This model correctly recovers the Navier-Stokes equation without any additional term yields,

$$\frac{\partial \rho}{\partial t} + \frac{\partial(\rho\mathbf{u})}{\partial \boldsymbol{x}} = 0 \tag{6.55}$$

$$\frac{\partial(\rho\mathbf{u})}{\partial t} + \frac{\partial(\rho\mathbf{uu})}{\partial \boldsymbol{x}} = -\frac{\partial(c_s^2\rho)}{\partial \boldsymbol{x}} + \mathbf{F} + \frac{\partial}{\partial \boldsymbol{x}}\left[\rho\nu\left(\frac{\partial \mathbf{u}}{\partial \boldsymbol{x}} + \left(\frac{\partial \mathbf{u}}{\partial \boldsymbol{x}}\right)^T\right)\right] \tag{6.56}$$

To resolve the problem of thermodynamic inconsistency. Li et al. (2012) proposed an improved version of Guo method. According to the mechanical stability condition of the pseudopotential model presented earlier in this chapter shown below,

$$\int_{\rho_g}^{\rho_l} \left(P_0 - c_s^2\rho - \frac{Gc^2}{2}\psi^2\right)\frac{\psi'}{\psi^{1+\varepsilon}}\,d\rho = 0 \tag{6.57}$$

when the Yuan and Schaffer (2006) kind of pseudopotential is used, there is an opportunity to approximately achieve thermodynamic consistency by adjusting the parameter $\varepsilon = -{}^{2\alpha}/_{\beta}$. However, because the value of the parameter ε is fixed once the form of the interaction force and the corresponding weights are chosen we will need another tuning parameter. On the other hand, according to the definition of the normal pressor tensor for a flat surface in Eq. (6.19) ε can be tuned by making the coefficient before the term $\left(\frac{d\psi}{dn}\right)^2$ adjustable. Interestingly, $\left(\frac{d\psi}{dn}\right)^2$ is related to the following two terms in the pressure tensor; $\boldsymbol{\nabla}\psi\boldsymbol{\nabla}\psi$ and $|\boldsymbol{\nabla}\psi|^2\mathbf{I}$. Therefore, the coefficient of $\left(\frac{d\psi}{dn}\right)^2$ can be made adjustable by introducing a tuning constant that will modify either of the two terms above while maintaining the overall form of the pressure tensor.

Recently, (Li et al., 2012) presented an improved forcing scheme within the BGK framework. In this work, theoretical and numerical analyses were first performed on the Shan and Chen model (1993) and the exact difference method (Kupershtokh et al. 2009) forcing schemes different. These analyses revealed the relationship between the coefficients before the extra term $-\frac{\partial}{\partial \boldsymbol{x}}\left(\frac{\mathbf{FF}}{\rho}\right)$ (Chapter 5, Eqs. (5.64) and (5.70)) and numerical performance of these schemes. Noting that the additional term is the divergence of a tensor and can be given by the term

$$-\frac{\partial}{\partial \boldsymbol{x}}\left(\frac{\mathbf{FF}}{\rho}\right) = -G^2c^4\frac{\partial}{\partial \boldsymbol{x}}\left(\frac{\psi^2}{\rho}\boldsymbol{\nabla}\psi\boldsymbol{\nabla}\psi\right) + O(\partial^5) \qquad (6.58)$$

Li et al., (2012) adjusted the parameter ε by modifying the coefficient of the term $\boldsymbol{\nabla}\psi\boldsymbol{\nabla}\psi$ in the pressure tensor while maintaining the overall form of the pressure tensor. In a later work (Li et al., 2013), utilized the MRT collision operator to derived a corresponding forcing scheme in moment space. Xu et al., (2015) later extended the forcing scheme to a 3D model. Below we briefly introduce the 3D MRT pseudopotential lattice Boltzmann model with the improved forcing scheme.

Starting from Guo et al., (2002) forcing scheme, Li et al. (2012) introduced an improved velocity that is a slight modification of the velocity in Guo model given by

$$\bar{\mathbf{v}} = \mathbf{v} = \mathbf{u} = \sum_{\alpha} f_{\alpha}\boldsymbol{e_{\alpha}} + \frac{1}{2}\left(\frac{\delta_t}{\rho} + \frac{2\sigma}{(\nu\psi^2)}\right)\mathbf{F}$$

$$C_e = B_e = \left(1 - \frac{1}{2\tau}\right) \tag{6.59}$$

Performing the Chapmans-Enskog multi-scale analysis, we obtain the following hydrodynamic equations

$$\frac{\partial\rho}{\partial t} + \frac{\partial(\rho\mathbf{u})}{\partial\boldsymbol{x}} = 0 \tag{6.60}$$

$$\begin{aligned}\frac{\partial(\rho\mathbf{u})}{\partial t} + \frac{\partial(\rho\mathbf{uu})}{\partial\boldsymbol{x}} \\ &= -\frac{\partial(c_s^2\rho)}{\partial\boldsymbol{x}} + \mathbf{F} + \frac{\partial}{\partial\boldsymbol{x}}\left[\rho\nu\left(\frac{\partial\mathbf{u}}{\partial\boldsymbol{x}} + \left(\frac{\partial\mathbf{u}}{\partial\boldsymbol{x}}\right)^T\right)\right] \\ &- \delta_t\frac{\partial}{\partial\boldsymbol{x}}\left(2\sigma\frac{\mathbf{FF}}{\psi^2}\right)\end{aligned} \tag{6.61}$$

By noting that the addition term $\frac{\partial}{\partial\boldsymbol{x}}\left(2\sigma\frac{\mathbf{FF}}{\psi^2}\right)$ is the divergence of a tensor it can therefore be absorbed into the normal pressure tensor. Through Taylor expansion of the pseuo-potential force as defined in Eq. (6.2) we obtain the leading terms of the interaction force. Subsequently, the leading term of the interaction force can be used to determine the simplified form of the addition term in Eq. (6.61) as,

$$-\frac{\partial}{\partial\boldsymbol{x}}\left(2\sigma\frac{\mathbf{FF}}{\psi^2}\right) = -2G^2c^4\sigma\frac{\partial}{\partial\boldsymbol{x}}(\nabla\psi\nabla\psi) + O(\partial^5) \tag{6.62}$$

Meanwhile, the pressure tensor of the model can now be redefined as:

$$\mathbf{P} = \mathbf{P}_{\mathrm{original}} + \ 2G^2c^4\sigma(\boldsymbol{\nabla}\psi\boldsymbol{\nabla}\psi) \tag{6.63}$$

where $\varepsilon = \ -2\,(\alpha + 24\delta_t G\sigma)/\beta$ is now in equation (6.21). Note that although the coefficient of the term $\boldsymbol{\nabla}\psi\boldsymbol{\nabla}\psi$ is altered, however the nature of the pressure tensor remains the same (Eq. 6.13).

Next, we determine the macroscopic equations for the MRT 3D lattice Boltzmann model with the improved forcing scheme. We perform the Chapman-Enskog multi-scale analysis in moment space.

$$f_\alpha(\boldsymbol{x} + \boldsymbol{\xi}_\alpha\delta_t, t + \delta_t) = \sum_{n=0} \varepsilon^n(\partial_t + \boldsymbol{\xi}_\alpha \cdot \boldsymbol{\nabla})^n f_\alpha(\boldsymbol{x}, t) \tag{6.64}$$

$$f_\alpha = \sum_{n=0} \varepsilon^n f_\alpha^{(n)} \tag{6.65}$$

$$\partial_t = \sum_{n=1} \varepsilon^n \partial_{t_n}^{(n)} \tag{6.66}$$

Applying the above expansions to the lattice Boltzmann equation. We obtain the following relationship for the zeroth; first and second-order expansion in ε

$$\mathrm{O}(\varepsilon^0): \qquad f_\alpha^{(0)} = f_\alpha^{eq} \tag{6.67}$$

$$\mathrm{O}(\varepsilon^1): \qquad \left(\partial_{t_1} + \boldsymbol{\xi}_\alpha \cdot \boldsymbol{\nabla}\right) f_\alpha^{(0)} = -\sum_\beta \boldsymbol{\Lambda} f_\beta^{(1)} + \sum_\beta \left(\mathbf{I} - \frac{\boldsymbol{\Lambda}}{2}\right) F_\beta \tag{6.68}$$

$$\text{O}(\varepsilon^2): \quad \begin{aligned} &\partial_{t_2} f_\alpha^{(0)} + \left(\partial_{t_1} + \boldsymbol{\xi}_\alpha \cdot \boldsymbol{\nabla}\right) \sum_\beta \left(\mathbf{I} - \frac{\boldsymbol{\Lambda}}{2}\right) f_\beta^{(1)} \\ &+ \frac{\delta_t}{2} \left(\partial_{t_1} + \boldsymbol{\xi}_\alpha \cdot \boldsymbol{\nabla}\right) \sum_\beta \left(\mathbf{I} - \frac{\boldsymbol{\Lambda}}{2}\right) F_\beta \\ &= -\sum\nolimits_\beta \boldsymbol{\Lambda} f_\beta^{(2)} \end{aligned} \tag{6.69}$$

Next, we multiplied Eqs. (6.67) - (6.69) by the transform matrix to transform the equations into moment space.

$$\text{O}(\varepsilon^0): \quad \hat{\boldsymbol{f}}^{(0)} = \hat{\boldsymbol{f}}^{(eq)} \tag{6.70}$$

$$\text{O}(\varepsilon^1): \quad \left(\partial_{t_1} + \hat{\mathbf{E}} \cdot \boldsymbol{\nabla}\right) \hat{\boldsymbol{f}}^{(0)} = -\hat{\boldsymbol{\Lambda}} \hat{\boldsymbol{f}}^{(1)} + \left(\mathbf{I} - \frac{1}{2} \hat{\boldsymbol{\Lambda}}\right) \hat{\mathbf{F}} \tag{6.71}$$

$$\text{O}(\varepsilon^2): \quad \begin{aligned} &\partial_{t_2} \hat{\boldsymbol{f}}^{(0)} + \left(\partial_{t_1} + \hat{\mathbf{E}} \cdot \boldsymbol{\nabla}\right) \left(\mathbf{I} - \frac{1}{2} \hat{\Lambda}\right) \hat{\boldsymbol{f}}^{(1)} \\ &+ \frac{\delta_t}{2} \left(\partial_{t_1} + \hat{\mathbf{E}} \cdot \boldsymbol{\nabla}\right) \left(\mathbf{I} - \frac{1}{2} \hat{\Lambda}\right) \hat{\mathbf{F}} \\ &= -\frac{\hat{\boldsymbol{\Lambda}}}{\delta_t} \hat{\boldsymbol{f}}^{(2)} \end{aligned} \tag{6.72}$$

where $\hat{\mathbf{E}} = \mathbf{M} \boldsymbol{\xi}_\alpha \mathbf{M}^{-1}$,

$$\hat{\mathbf{F}} = \mathbf{MF} = \begin{bmatrix} 0 \\ \mathbf{2v} \cdot \mathbf{F} + \dfrac{6\sigma|\mathbf{F}|^2}{\psi^2 \delta_t (s_e^{-1} - 0.5)} \\ -10\mathbf{v} \cdot \mathbf{F} \\ F_x \\ -\dfrac{\mathbf{7}}{\mathbf{3}} F_x \\ F_y \\ -\dfrac{\mathbf{7}}{\mathbf{3}} F_y \\ F_z \\ -\dfrac{\mathbf{7}}{\mathbf{3}} F_z \\ 4v_x F_x - 2v_y F_y - 2v_z F_z \\ 2v_y F_y - 2u_z F_z \\ v_x F_y + v_y F_x \\ v_y F_z + v_z F_y \\ v_x F_z + v_z F_x \\ 0 \end{bmatrix} \tag{6.73}$$

and

$$\hat{\boldsymbol{f}}^{(1)} = \left|\hat{f}^{(1)}\right\rangle = [0, e^{(1)}, \epsilon^{(1)}, \frac{\delta_t}{2}\mathrm{F}_x, q_x^{(1)},$$

$$\frac{\delta_t}{2}\mathrm{F}_y, q_y^{(1)}, \frac{\delta_t}{2}\mathrm{F}_z, q_z^{(1)}, 3p_{xx}^{(1)}, p_{ww}^{(1)}, p_{xy}^{(1)}, p_{yz}^{(1)}, p_{xz}^{(1)}, m_{xzy}^{(1)}]^{\mathrm{T}}$$

We can now obtain the components of the first-order equations in moment space by substituting Eq. (6.68), in Eq. (6.66) as

$$\partial_{t_1}\rho + \partial_x(\rho u_x) + \partial_y(\rho u_y) + \partial_z(\rho u_z) = 0 \tag{6.74a}$$

$$\partial_{t_1}\left(\rho(-1 + |\mathbf{u}|^2)\right) - \frac{1}{3}\left(\partial_x(\rho u_x) + \partial_y(\rho u_y) + \partial_z(\rho u_z)\right)$$
$$= -\frac{s_e}{\delta_t}e^{(1)} + \left(1 - \frac{1}{2}s_e\right)\left(2\mathbf{v} \cdot \mathbf{F} + \frac{6\sigma|\mathbf{F}|^2}{\psi^2 \delta_t (s_e^{-1} - 0.5)}\right) \tag{6.74b}$$

$$\partial_{t_1}\big(\rho(1-5|\mathbf{u}|^2)\big) - \frac{7}{3}\left(\partial_x(\rho u_x) + \partial_y(\rho u_y) + \partial_z(\rho u_z)\right) = -\frac{s_\epsilon}{\delta_t}\epsilon^{(1)} + \left(1-\frac{1}{2}s_\epsilon\right)(10\mathbf{v}\cdot\mathbf{F}) \tag{6.74c}$$

$$\partial_{t_1}(\rho u_x) + \partial_x(c_s^2\rho + \rho {u_x}^2) + \partial_y(\rho u_x u_y) + \partial_z(\rho u_x u_z) = -\frac{1}{2}s_j F_x + \left(1-\frac{1}{2}s_j\right)F_x \tag{6.74d}$$

$$\partial_{t_1}\left(-\frac{7}{3}\rho u_x\right) + \partial_x\left(-\frac{7}{9}\rho + \frac{1}{3}\rho\big(-7{u_x}^2 + 5{u_y}^2 + 5{u_z}^2\big)\right) + \partial_y(\rho u_x u_y) + \partial_z(\rho u_x u_z) = -\frac{s_q}{\delta_t}q_x^{(1)} - \frac{7}{3}\left(1-\frac{1}{2}s_j\right)F_x \tag{6.74e}$$

$$\partial_{t_1}(\rho u_y) + \partial_x(\rho u_x u_y) + \partial_y(c_s^2\rho + \rho {u_y}^2) + \partial_z(\rho u_y u_z) = -\frac{1}{2}s_j F_y + \left(1-\frac{1}{2}s_j\right)F_y \tag{6.74f}$$

$$\partial_{t_1}\left(-\frac{7}{3}\rho u_y\right) + \partial_x(\rho u_x u_y) + \partial_y\left(-\frac{7}{9}\rho + \frac{1}{3}\rho\big(-5{u_x}^2 - 7{u_y}^2 + 5{u_z}^2\big)\right) + \partial_z(\rho u_y u_z) = -\frac{s_q}{\delta_t}q_y^{(1)} - \frac{7}{3}\left(1-\frac{1}{2}s_j\right)F_y \tag{6.74g}$$

$$\partial_{t_1}(\rho u_z) + \partial_x(\rho u_x u_y) + \partial_y(\rho u_y u_z) + \partial_z(c_s^2\rho + \rho {u_z}^2) = -\frac{1}{2}s_j F_z + \left(1-\frac{1}{2}s_j\right)F_z \tag{6.74h}$$

$$\begin{aligned}\partial_{t_1}\left(-\frac{7}{3}\rho u_z\right) &+ \partial_x\left(\rho u_x u_y\right) + \partial_y\left(\rho u_y u_z\right)\\ &+ \partial_z\left(-\frac{7}{9}\rho + \frac{1}{3}\rho\left(5{u_x}^2 + 5{u_y}^2 - 7{u_z}^2\right)\right)\\ &= -\frac{s_q}{\delta_t} q_z^{(1)} - \frac{7}{3}\left(1 - \frac{1}{2}s_j\right)F_z\end{aligned} \tag{6.74i}$$

$$\begin{aligned}\partial_{t_1}\left(\rho\left(2u_x^2 - u_y^2 - u_z^2\right)\right) &+ \frac{2}{3}\left(\partial_x(2\rho u_x) + \partial_y\left(\rho u_y\right) + \partial_z(\rho u_z)\right)\\ &= -3\frac{s_\nu}{\delta_t}P_{xx}^{(1)} + \left(1 - \frac{1}{2}s_\nu\right)\left(4v_xF_x - 2v_yF_y - 2v_zF_z\right)\end{aligned} \tag{6.74j}$$

$$\begin{aligned}\partial_{t_1}\left(\rho\left(u_y^2 - u_z^2\right)\right) &+ \frac{2}{3}\left(\partial_y\left(\rho u_y\right) - \partial_z(\rho u_z)\right)\\ &= -\frac{s_\nu}{\delta_t}P_{ww}^{(1)} + \left(1 - \frac{1}{2}s_\nu\right)\left(2v_yF_y - 2v_zF_z\right)\end{aligned} \tag{6.74k}$$

$$\begin{aligned}\partial_{t_1}\left(\rho u_x u_y\right) &+ \frac{1}{3}\left(\partial_x\left(\rho u_y\right) + \partial_y(\rho u_x)\right)\\ &= -\frac{s_\nu}{\delta_t}P_{xy}^{(1)} + \left(1 - \frac{1}{2}s_\nu\right)\left(2v_xF_y - 2v_yF_x\right)\end{aligned} \tag{6.74l}$$

$$\begin{aligned}\partial_{t_1}\left(\rho u_y u_z\right) &+ \frac{1}{3}\left(\partial_y(\rho u_z) + \partial_z\left(\rho u_y\right)\right)\\ &= -\frac{s_\nu}{\delta_t}P_{yz}^{(1)} + \left(1 - \frac{1}{2}s_\nu\right)\left(2v_yF_z - 2v_zF_y\right)\end{aligned} \tag{6.74m}$$

$$\begin{aligned}\partial_{t_1}(\rho u_x u_z) &+ \frac{1}{3}\left(\partial_x(\rho u_z) + \partial_z(\rho u_x)\right)\\ &= -\frac{s_\nu}{\delta_t}P_{zx}^{(1)} + \left(1 - \frac{1}{2}s_\nu\right)(2v_xF_z - 2v_zF_x)\end{aligned} \tag{6.74n}$$

$$\partial_x\left(\rho u_y u_z\right) + \partial_y(\rho u_x u_z) + \partial_z\left(\rho u_x u_y\right) = -\frac{s_{xyz}}{\delta_t}m_{xyz}^{(1)} \tag{6.74o}$$

Similarly, for the components of the second-order equations in moment space, we are interested only in the dynamical equations of the conserved moments. Hence, we present only the second-order equations of the conserved moments below

$$\partial_{t_2}\rho = 0 \tag{6.75}$$

$$\begin{aligned}
\partial_{t_2}(\rho u_x) - \frac{\delta_t}{2}\partial_{t_1}\left[\left(1-\frac{s_j}{2}\right)F_x\right] + \partial_x\left[\left(1-\frac{s_e}{2}\right)\frac{1}{3}e^{(1)} + \left(1-\frac{s_v}{2}\right)P_{xx}^{(1)}\right]& \\
+ \partial_y\left[\left(1-\frac{s_v}{2}\right)P_{xx}^{(1)}\right] + \partial_z\left[\left(1-\frac{s_v}{2}\right)P_{xz}^{(1)}\right]& \\
+ \frac{\delta_t}{2}\partial_{t_1}\left[\left(1-\frac{s_j}{2}\right)F_x\right]& \\
+ \frac{\delta_t}{2}\partial_x\left[\frac{2}{3}\left(1-\frac{s_e}{2}\right)\left(v_xF_x + v_yF_y + v_zF_z\right)\right.& \\
+ \frac{2}{3}\left(1-\frac{s_v}{2}\right)\left(2v_xF_x - v_yF_y - v_zF_z\right)& \\
\left.+ \frac{1}{3}\left(1-\frac{s_e}{2}\right)\left(\frac{6\sigma|\mathbf{F}|^2}{\psi^2\delta_t(s_e^{-1}-0.5)}\right)\right]& \\
+ \frac{\delta_t}{2}\partial_y\left[\left(1-\frac{s_v}{2}\right)\left(v_xF_y + v_yF_x\right)\right]& \\
+ \frac{\delta_t}{2}\partial_y\left[\left(1-\frac{s_v}{2}\right)\left(v_xF_z + v_zF_x\right)\right] = 0&
\end{aligned} \tag{6.76}$$

$$
\begin{aligned}
&\partial_{t_2}(\rho u_y) - \frac{\delta_t}{2}\partial_{t_1}\Big[\Big(1-\frac{s_j}{2}\Big)F_y\Big] \\
&\quad + \partial_x\Big[\Big(1-\frac{s_\nu}{2}\Big)P_{xy}^{(1)}\Big] + \partial_y\Big[\Big(1-\frac{s_e}{2}\Big)\frac{1}{3}e^{(1)} \\
&\quad + \Big(1-\frac{s_\nu}{2}\Big)\frac{1}{2}P_{ww}^{(1)} - \Big(1-\frac{s_\nu}{2}\Big)\frac{1}{2}P_{xx}^{(1)}\Big] \\
&\quad + \partial_z\Big[\Big(1-\frac{s_\nu}{2}\Big)P_{yz}^{(1)}\Big] + \frac{\delta_t}{2}\partial_{t_1}\Big[\Big(1-\frac{s_j}{2}\Big)F_y\Big] \\
&\quad + \frac{\delta_t}{2}\partial_x\Big[\Big(1-\frac{s_\nu}{2}\Big)(v_xF_y + v_yF_x)\Big] \qquad (6.77) \\
&\quad + \frac{\delta_t}{2}\partial_y\Bigg[\Big(1-\frac{s_\nu}{2}\Big)\frac{2}{3}(-v_xF_x + 2v_yF_y - v_zF_z) \\
&\quad + \frac{2}{3}\Big(1-\frac{s_\nu}{2}\Big)(v_xF_x + v_yF_y + v_zF_z) \\
&\quad + \frac{1}{3}\Big(1-\frac{s_e}{2}\Big)\left(\frac{6\sigma|\mathbf{F}|^2}{\psi^2\delta_t(s_e^{-1}-0.5)}\right)\Bigg] \\
&\quad + \frac{\delta_t}{2}\partial_z\Big[\Big(1-\frac{s_\nu}{2}\Big)P_{yz}^{(1)}\Big] = 0
\end{aligned}
$$

$$
\begin{aligned}
&\partial_{t_2}(\rho u_z) - \frac{\delta_t}{2}\partial_{t_1}\left[\left(1-\frac{s_j}{2}\right)F_z\right] \\
&\qquad + \partial_x\left[\left(1-\frac{s_v}{2}\right)P_{xz}^{(1)}\right] + \partial_y\left[\left(1-\frac{s_v}{2}\right)P_{yz}^{(1)}\right] \\
&\qquad + \partial_z\Bigg[\left(1-\frac{s_e}{2}\right)\frac{1}{3}e^{(1)} - \left(1-\frac{s_v}{2}\right)\frac{1}{2}P_{ww}^{(1)} \\
&\qquad - \left(1-\frac{s_v}{2}\right)\frac{1}{2}P_{xx}^{(1)}\Bigg] + \frac{\delta_t}{2}\partial_{t_1}\left[\left(1-\frac{s_j}{2}\right)F_z\right] \\
&\qquad + \frac{\delta_t}{2}\partial_x\left[\left(1-\frac{s_v}{2}\right)\left(v_xF_z + v_zF_x\right)\right] \\
&\qquad + \frac{\delta_t}{2}\partial_y\left[\left(1-\frac{s_v}{2}\right)\left(v_yF_z + v_zF_y\right)\right] \\
&\qquad + \frac{\delta_t}{2}\partial_z\Bigg[\left(1-\frac{s_v}{2}\right)\frac{2}{3}\left(v_xF_x + v_yF_y + v_zF_z\right) \\
&\qquad - \frac{2}{3}\left(1-\frac{s_v}{2}\right)\left(v_xF_x + v_yF_y - 2v_zF_z\right) \\
&\qquad + \frac{1}{3}\left(1-\frac{s_e}{2}\right)\left(\frac{6\sigma|\mathbf{F}|^2}{\psi^2\delta_t(s_e^{-1}-0.5)}\right)\Bigg] = 0
\end{aligned} \tag{6.78}
$$

$e^{(1)}$, $\epsilon^{(1)}$,$P_{xx}^{(1)}$, $P_{ww}^{(1)}$, $P_{xy}^{(1)}$, $P_{yz}^{(1)}$, $P_{xz}^{(1)}$ are unknown. In other to evaluate these unknowns, we rearranged Eqs. (6.74b) - (6.74o) and use the continuity and momentum equations Eqs. (6.74a), (6.74d), (6.74f), (6.74h) to simplify the resulting expression. Neglecting terms of $O(Ma^3)$ and higher, we derive the following equations:

$$
\begin{aligned}
-s_e e^{(1)} = {}& 2c_s^2\rho\delta_t\left(\partial_x u_x + \partial_y u_y + \partial_z u_z\right) \\
&+ s_e\delta_t\left(v_xF_x + v_yF_y + v_zF_z\right) - \frac{6\sigma\left({F_x}^2 + {F_y}^2 + {F_z}^2\right)s_e}{\psi^2}
\end{aligned} \tag{6.79}
$$

$$-3s_v P_{xx}^{(1)} = 2c_s^2\rho\delta_t\left(2\partial_x u_x - \partial_y u_y - \partial_z u_z\right) \\ + s_v\delta_t\left(2v_x F_x - v_y F_y - v_z F_z\right) \tag{6.80}$$

$$-s_v P_{ww}^{(1)} = 2c_s^2\rho\delta_t\left(\partial_y u_y - \partial_z u_z\right) + s_v\delta_t\left(v_y F_y - v_z F_z\right) \tag{6.81}$$

$$-s_v P_{xy}^{(1)} = c_s^2\rho\delta_t\left(\partial_x u_y + \partial_y u_x\right) + \frac{s_v\delta_t}{2}\left(v_x F_y - v_y F_x\right) \tag{6.82}$$

$$-s_v P_{yz}^{(1)} = c_s^2\rho\delta_t\left(\partial_y u_z + \partial_z u_y\right) + \frac{s_v\delta_t}{2}\left(v_y F_z - v_z F_y\right) \tag{6.83}$$

$$-s_v P_{xz}^{(1)} = c_s^2\rho\delta_t(\partial_x u_z + \partial_z u_x) + \frac{s_v\delta_t}{2}(v_x F_z - v_z F_x) \tag{6.84}$$

Now we substitute Eqs. (6.79) - (6.84) into Eqs. (6.76) - (6.78) to determine the second-order hydrodynamic equations in ϵ as

$$\partial_{t_2}\rho = 0 \tag{6.85}$$

$$\begin{aligned}\partial_{t_2}(\rho u_x) = \partial_x\Bigg[&\rho\zeta\left(\partial_x u_x + \partial_y u_y + \partial_z u_z\right)\\ &+\frac{2}{3}\rho\nu\left(2\partial_x u_x - \partial_y u_y - \partial_z u_z\right) + \frac{2\sigma|\mathbf{F}|^2}{\psi^2}\Bigg]\\ &+ \partial_y\left[\rho\nu\left(\partial_x u_y + \partial_y u_x\right)\right] + \partial_z\left[\rho\nu(\partial_x u_z + \partial_z u_x)\right]\end{aligned} \tag{6.86}$$

$$\begin{aligned}\partial_{t_2}(\rho u_y) = \partial_x&\left[\rho\nu\left(\partial_x u_y + \partial_y u_x\right)\right]\\ &+ \partial_y\Bigg[\rho\zeta\left(\partial_x u_x + \partial_y u_y + \partial_z u_z\right)\\ &+\frac{2}{3}\rho\nu\left(-\partial_x u_x + 2\partial_y u_y - \partial_z u_z\right) - \frac{2\sigma|\mathbf{F}|^2}{\psi^2}\Bigg]\\ &+ \partial_z\left[\rho\nu\left(\partial_y u_z + \partial_z u_y\right)\right]\end{aligned} \tag{6.87}$$

$$\begin{aligned}\partial_{t_2}(\rho u_z) = \partial_x&\left[\rho\nu(\partial_x u_z + \partial_z u_x)\right] + \partial_y\left[\rho\nu\left(\partial_y u_z + \partial_z u_y\right)\right]\\ &+ \partial_z\Bigg[\rho\zeta\left(\partial_x u_x + \partial_y u_y + \partial_z u_z\right)\\ &-\frac{2}{3}\rho\nu\left(\partial_x u_x + \partial_y u_y - 2\partial_z u_z\right) - \frac{2\sigma|\mathbf{F}|^2}{\psi^2}\Bigg]\end{aligned} \tag{6.88}$$

where the kinematic viscosity ν and bulk viscosity ζ are given by

$$\nu = \frac{1}{3}\left(\frac{1}{s_\nu} - \frac{1}{2}\right)\delta_t \tag{6.89}$$

$$\zeta = \frac{2}{9}\left(\frac{1}{s_e} - \frac{1}{2}\right)\delta_t \tag{6.90}$$

Combining the results from Eq. (6.85) - Eq. (6.88) and Eq. (6.74), using $\partial_t = \partial_{t_1} + \epsilon\partial_{t_2}$ and substituting for pseudopotential force (Eq. 6.2) we obtain the macroscopic dynamical equation for the conserved moments.

$$\frac{\partial \rho}{\partial \mathrm{t}} + \boldsymbol{\nabla} \cdot (\rho \bar{\mathbf{v}}) = 0 \tag{6.91}$$

$$\begin{aligned} \frac{\partial(\rho\bar{\mathbf{v}})}{\partial \mathrm{t}} + \boldsymbol{\nabla} \cdot (\rho\bar{\mathbf{v}}\bar{\mathbf{v}}) \\ &= -\boldsymbol{\nabla} \cdot (\rho c_s^2 - 2\mathrm{G}^2 c^4 \sigma |\nabla\psi|^2)\mathbf{I} + \boldsymbol{\nabla} \cdot \boldsymbol{\Pi} + \mathbf{F} \\ &+ \frac{\mathrm{G}c^4}{6}\psi\boldsymbol{\nabla}\boldsymbol{\nabla}\psi \end{aligned} \tag{6.92}$$

$$\boldsymbol{\Pi} = \rho\nu[\nabla\mathbf{v} + (\nabla\mathbf{v})^{\mathrm{T}}] + \rho\left(\zeta - \frac{2}{3}\right)(\nabla \cdot \mathbf{v})\mathbf{I} \tag{6.93}$$

Such that the hydrodynamic variables can be given as

$$\rho = \sum\nolimits_{\alpha} f_{\alpha} \tag{6.94}$$

$$\rho\bar{\mathbf{v}} = \rho\mathbf{v} = \rho\mathbf{u} = \sum_{\alpha} f_{\alpha}\boldsymbol{e_{\alpha}} + \frac{1}{2}\delta_t\mathbf{F} \tag{6.95}$$

6.4 References

Benzi R, Biferale L, Sbragaglia M, Succi S, Toschi F (2006) Mesoscopic modeling of a two-phase flow in the presence of boundaries: The contact angle Physical Review E 74:021509

Guo Z, Zheng C, Shi B (2002) Discrete lattice effects on the forcing term in the lattice Boltzmann method Physical Review E 65:046308

He X, Shan X, Doolen GD (1998) Discrete Boltzmann equation model for nonideal gases Physical Review E 57:R13-R16

He X, Zou Q, Luo L-S, Dembo M (1997) Analytic solutions of simple flows and analysis of nonslip boundary conditions for the lattice Boltzmann BGK model Journal of Statistical Physics 87:115-136 doi:10.1007/BF02181482

Huang H, Krafczyk M, Lu X (2011) Forcing term in single-phase and Shan-Chen-type multiphase lattice Boltzmann models Physical Review E 84:046710

Koplik J, Banavar JR (1995) Continuum Deductions from Molecular Hydrodynamics Annual Review of Fluid Mechanics 27:257-292 doi:10.1146/annurev.fl.27.010195.001353

Kupershtokh AL, Medvedev DA, Karpov DI (2009) On equations of state in a lattice Boltzmann method Computers & Mathematics with Applications 58:965-974 doi:http://dx.doi.org/10.1016/j.camwa.2009.02.024

Lallemand P, Luo L-S (2000) Theory of the lattice Boltzmann method: Dispersion, dissipation, isotropy, Galilean invariance, and stability Physical Review E 61:6546-6562

Lallemand P, Luo L-S (2003) Theory of the lattice Boltzmann method: Acoustic and thermal properties in two and three dimensions Physical Review E 68:036706

Li Q, Luo KH, Li XJ (2012) Forcing scheme in pseudopotential lattice Boltzmann model for multiphase flows Physical Review E 86:016709

Li Q, Luo KH, Li XJ (2013) Lattice Boltzmann modeling of multiphase flows at large density ratio with an improved pseudopotential model Physical Review E 87:053301

Nourgaliev RR, Dinh TN, Theofanous TG, Joseph D (2003) The lattice Boltzmann equation method: theoretical interpretation, numerics and implications International Journal of Multiphase Flow 29:117-169 doi:http://doi.org/10.1016/S0301-9322(02)00108-8

Premnath KN, Abraham J (2007) Three-dimensional multi-relaxation time (MRT) lattice-Boltzmann models for multiphase flow Journal of Computational Physics 224:539-559 doi:http://dx.doi.org/10.1016/j.jcp.2006.10.023

Qian YH, Humières DD, Lallemand P (1992) Lattice BGK Models for Navier-Stokes Equation EPL (Europhysics Letters) 17:479

Rowlinson J. S. and Widom B., (1982) Molecular Theory of Capillarity. Clarendon, Oxford.

Sbragaglia M, Benzi R, Biferale L, Succi S, Sugiyama K, Toschi F (2007) Generalized lattice Boltzmann method with multirange pseudopotential Physical Review E 75:026702

Sbragaglia M, Benzi R, Biferale L, Succi S, Toschi F (2006) Surface Roughness-Hydrophobicity Coupling in Microchannel and Nanochannel Flows Physical Review Letters 97:204503

Sbragaglia M, Shan X (2011) Consistent pseudopotential interactions in lattice Boltzmann models Physical Review E 84:036703

Shan X (2008) Pressure tensor calculation in a class of nonideal gas lattice Boltzmann models Physical Review E 77:066702

Shan X, Chen H (1994) Simulation of nonideal gases and liquid-gas phase transitions by the lattice Boltzmann equation Physical Review E 49:2941-2948

Sun K, Wang T, Jia M, Xiao G (2012) Evaluation of force implementation in pseudopotential-based multiphase lattice Boltzmann models Physica A: Statistical Mechanics and its Applications 391:3895-3907 doi:http://dx.doi.org/10.1016/j.physa.2012.03.008

Xu A, Zhao TS, An L, Shi L (2015) A three-dimensional pseudo-potential-based lattice Boltzmann model for multiphase flows with large density ratio and variable surface tension International Journal of Heat and Fluid Flow 56:261-271 doi:http://dx.doi.org/10.1016/j.ijheatfluidflow.2015.08.001

Yuan P, Schaefer L (2006) Equations of state in a lattice Boltzmann model Physics of Fluids 18:042101 doi:doi:http://dx.doi.org/10.1063/1.2187070

7. CHAPTER SEVEN: INVESTIGATION OF AUTOMATIC DROPLET TRANSPORTATION ON WEDGE-SHAPED PATTERNED WETTABILITY GRADIENT SURFACES USING LATTICE BOLTZMANN METHOD

7.1 Abstract

We present a numerical investigation of the effect of different droplet-surface parameters on the automatic motion of a droplet on a wedge-shaped patterned microchannel surface by using a single component multiphase pseudo-potential-based lattice Boltzmann method. We studied the droplet dynamic behavior as a function of the wedge-surface relative wettability, pattern wedge angle, initial droplet position and gravitational acceleration. Our numerical results suggested that the average velocity of the droplet increases with increase in the wedge-surface relative wettability and wedge angle because of larger driving forces. As expected, for the cases in this paper, the results show that the average droplet velocity up an incline decreases as the angle of inclination increases. Also, we demonstrated that there exists a critical droplet volume below which gravitational effects on droplet dynamics become negligible. In general, our results are consistent with available test data in open literature as well as numerical studies using techniques other than lattice Boltzmann. More importantly, our findings suggest that there exits an interplay between the capillary and inertial forces in the droplet which could be the subject of future investigation.

7.2 Introduction

In this chapter, we investigated the effects of different droplet parameters on the automatic motion of the droplet in a microchannel numerically. This will include the effects of wedge-surface relative wettability, pattern wedge angle, the initial droplet position, and gravitational acceleration on the droplet dynamic behavior. Here we use the pseudopotential based single component multiphase Lattice Boltzmann method (SCMP LBM) due to its simplicity and computational efficiency. The fluid interaction force was incorporated via the improved forcing scheme proposed by Li et al., (2013). This forcing scheme offers an alternative approach to achieving thermodynamic consistency and simulation of large density ratio. In addition, we employed Yuan and Schaefer method (2006) to incorporate the Carnahan-Starling non-ideal equation of state (CS-EOS) (Carnahan and Starling, 1970a, b).

7.3 Numerical Method

For the D3Q15 model, the discrete velocity $\boldsymbol{\xi}_{\boldsymbol{\alpha}}$ is given as (D'Humières et al., 2002)

$$[\boldsymbol{e}_0, \boldsymbol{e}_1, \boldsymbol{e}_2, \boldsymbol{e}_3, \boldsymbol{e}_4, \boldsymbol{e}_5, \boldsymbol{e}_6, \boldsymbol{e}_7, \boldsymbol{e}_8, \boldsymbol{e}_9, \boldsymbol{e}_{10}, \boldsymbol{e}_{11}, \boldsymbol{e}_{12}, \boldsymbol{e}_{13}, \boldsymbol{e}_{14}] = c\begin{bmatrix} 0 & 1 & -1 & 0 & 0 & 0 & 0 & 1 & -1 & 1 & -1 & 1 & -1 & 1 & -1 \\ 0 & 0 & 0 & 1 & -1 & 0 & 0 & 1 & 1 & -1 & -1 & 1 & 1 & -1 & -1 \\ 0 & 0 & 0 & 0 & 0 & 1 & -1 & 1 & 1 & 1 & 1 & -1 & -1 & -1 & -1 \end{bmatrix} \tag{7.1}$$

where the lattice velocity $c = {}^{\delta_x}/_{\delta_t}$ and sound speed $c_s = {}^{c}/_{\sqrt{3}}$ and the weight factors ω_α are given by $\omega_0 = {}^{2}/_{9}$, $\omega_{1-6} = {}^{1}/_{9}$, and $\omega_{7-14} = {}^{1}/_{72}$. We define one lattice unit δ_x as 1 l.u., one time unit δ_t as 1 t.u. and one unit mass as 1 m.u. (Huang et al., 2011).

Also, based on the original pseudopotential LB model proposed by Shan and Chen (Shan and Chen 1993; Shan and Chen 1994), the fluid-fluid interaction force that produces phase segregation can be defined via a pseudopotential (an effective mass) which is a function of the local fluid density. For a single component multiphase flow, the interaction force has the following form (Shan 2008):

$$\mathbf{F}_f = -G\psi(x)\sum_{\alpha} w(|\xi_\alpha|^2)\psi(\boldsymbol{x} + \boldsymbol{\xi}_\alpha)\boldsymbol{\xi}_\alpha \tag{7.2}$$

where $\psi(x)$ is the effective mass, G is the interaction strength and $w(|\xi_\alpha|^2)$ are the weights. For the nearest-neighbor molecular interactions on D3Q15 lattice, the weights $w(|\xi_\alpha|^2)$ are $w(1) = {}^{1}/_{3}$ and $w(3) = {}^{1}/_{24}$.

Next, we used the adhesion force $\boldsymbol{F}_s$ proposed in chapter 6. Details of the force is shown below.

$$\boldsymbol{F}_s = -G_w\psi(x)\sum_{\alpha} w(|\xi_\alpha|^2)S(\boldsymbol{x} + \boldsymbol{\xi}_\alpha)\boldsymbol{\xi}_\alpha \tag{7.3}$$

where G_w is the absorption parameter, $S(\boldsymbol{x} + \boldsymbol{\xi}_\alpha) = \phi(x)s(\boldsymbol{x} + \boldsymbol{\xi}_\alpha)$ is the switch function. Note that $s(\boldsymbol{x} + \boldsymbol{\xi}_\alpha)$ is equal to 0 or 1 for a fluid or solid phase respectively. For

$$S(\boldsymbol{x} + \boldsymbol{\xi}_\alpha) = \phi(x + \boldsymbol{\xi}_\alpha)s(\boldsymbol{x} + \boldsymbol{\xi}_\alpha) \tag{7.4}$$

such that $\phi(x + \boldsymbol{e}_{\alpha})$ is equal to 0 for a fluid node and $\phi(x + \boldsymbol{e}_{\alpha}) =$

$\psi_{virutal}\left(\rho_{virtual}^{avg}(\boldsymbol{x}_s)\right)$

for a solid node and $\rho_{virtual}^{avg}(\boldsymbol{x}_s) = \frac{1}{N_f}\sum_{\alpha_f}\rho\left(\boldsymbol{x}_s + \boldsymbol{\xi}_{\alpha_f}\right)$

where $\boldsymbol{x}_s$ is the site of the solid node, N_f is the number of fluid nodes that directly connect to the solid node side and α_f are all indices α for which $\boldsymbol{x}_s + \boldsymbol{\xi}_{\alpha}$ is a boundary fluid node.

For cases in which the effect of gravitational force was considered, external force $\boldsymbol{F}_e = \rho\boldsymbol{g}$ is applied uniformly over the entire domain. Where, ρ is the density at current node and $\boldsymbol{g}$ is the body force per unit mass. Therefore, the total force **F** acting on a fluid particle in the multiphase flow can be given as:

$$\mathbf{F} = \boldsymbol{F}_f + \boldsymbol{F}_s + \boldsymbol{F}_e \tag{7.5}$$

Meanwhile, different equation of states (EOS) can be incorporated into the pseudopotential model via Yuan and Schafer method (Yuan and Schaefer, 2006) shown below

$$\psi = \sqrt{\frac{2(p - \rho c_s^2)}{Gc^2}} \tag{7.6}$$

On the other hand, in thermodynamic theory, the Maxwell construction requires that $\int_{v_g}^{v_l} p\, dV = p_0(v_l - v_g)$. This together with Eq. (7.2) yields,

$$\int_{\rho_g}^{\rho_l}\left(p_0 - \rho c_s^2 + \frac{Gc^2}{2}\psi^2\right)\frac{1}{\rho^2}\, d\rho = 0 \tag{7.7}$$

We can therefore achieve thermodynamic consistency approximately by adjusting the density profile from the mechanical stability condition in Eq. (6.28) in chapter 6 via σ (i.e. tune ε) to match the profile in Eq. (7.6) (Li et al., 2012, 2013).

In our single component multiphase (SCMP) simulations, we will use the Carnahan-Starling (Carnahan and Starling 1970a) equation of state (CS-EOS).

$$p = \rho RT \frac{1 + {}^{b\rho}/_{4} + \left({}^{b\rho}/_{4}\right)^2 - \left({}^{b\rho}/_{4}\right)^3}{\left(1 - {}^{b\rho}/_{4}\right)^3} - a\rho^2 \qquad (7.8)$$

where $a = 0.4963(RT_c)^2/P_c$, $b = 0.1873RT_c/P_c$. Here we set $a = 0.25$ and $b = 4$. Therefore, the critical temperature and pressure are $T_c = 0.0236$ and $P_c = 0.0011$ repsecitvely.

7.4 Simulation results and discussion

In this section, we first check if the multiphase LB model with CS-EOS described in the previous section can reproduce the correct liquid and vapor densities corresponding to different temperatures as given by the Maxwell construction (see Table 7.1). Then, we validated the model with Laplace’s law by simulating droplets with different radii. Finally, numerical simulations were conducted on passive droplet displacement in a microchannel. Since multiphase LB model is a diffused interface method, we considered the location of the interface as the point where the density is $= \frac{\rho_l + \rho_g}{2}$. Our results are provided in lattice units unless otherwise specified.

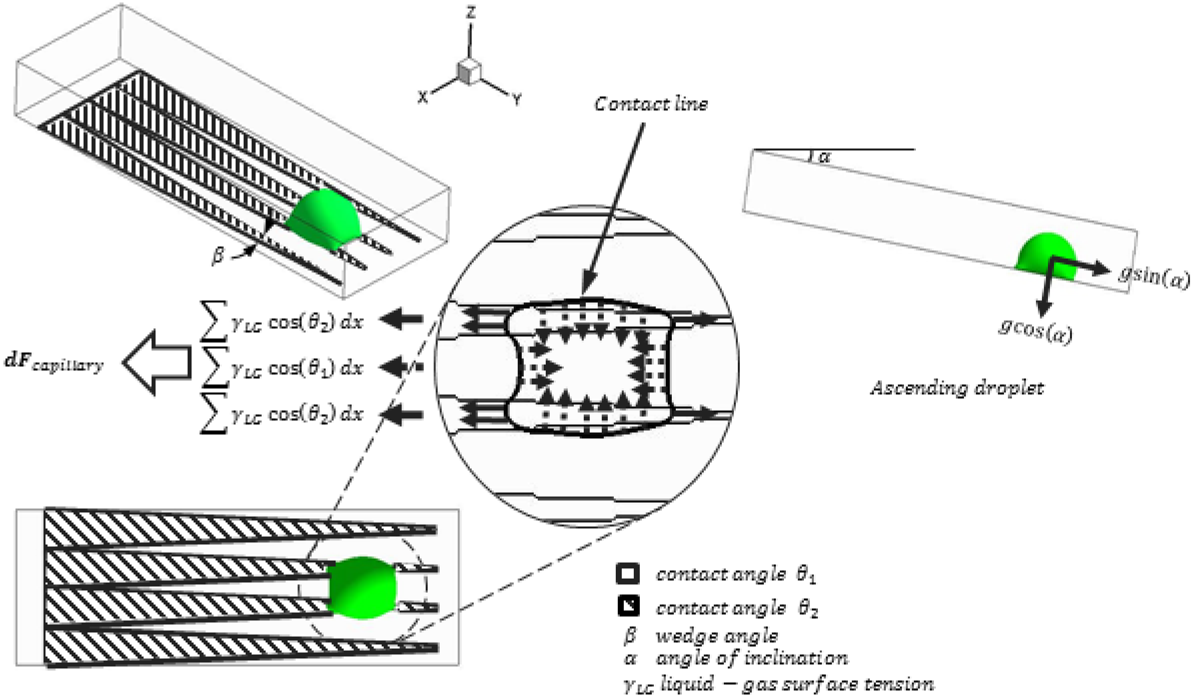

Fig. 7.1 Schematic diagram shows wedge-shaped tracks on a microchannel surface, different angles of inclinations, wedge-surface parameters and actuating force

7.4.1 Evaluation of thermodynamic consistency at low temperatures

In other to numerical evaluate whether the improved forcing scheme described above is consistent with Maxwell construction (Sukop and Thorne, 2007) at low temperatures, we conducted numerical simulations for the problem of a stationary spherical droplet with a radius of R= 30 l.u. In the simulation, we adopted a 121 x 121 x 121 lattice and use the CS-EOS with G= -1. Furthermore, periodic boundary conditions were applied in all three directions and the density field was initialized as shown below (Huang et al., 2011):

$$\rho(x,y,z) = \frac{\rho_l + \rho_g}{2} + \frac{\rho_l - \rho_g}{2} \times \left[\tanh\left(\frac{2\left(\sqrt{(r-R)}\right)}{W}\right)\right] \tag{7.9}$$

where $r = \sqrt{(x - x_0)^2 + (y - y_0)^2 + (z - z_0)^2}$, (x_0, y_0, z_0) is the center of the computational domain, W is the initial interface thickness and R is the radius of the droplet.

We set the relaxation times in equation 12 as $S_\rho = S_j = 1.0$, $S_e = S_\epsilon = 1.1$, $S_q = 1.1$, $S_{xyz} = 1.2$, $S_\nu = 1.25$ (i.e. $\tau_\nu = 0.8$) and adjusted σ in other to match our solutions with the Maxwell construction solutions. We also extended the simulations to $\tau_\nu = 1.0$ and $\tau_\nu = 0.6$. Through numerical investigation with different values of sigma, we find that the simulation result from $\sigma = 0.102$ (Fig. 7.2) compares well with the results presented in (Li et al., 2013) and the Maxwell construction solutions (Table 7.1). Moving forward, we used the temperature $\mathrm{T}/\mathrm{T}_c = 0.5$ for the remaining cases in this study.

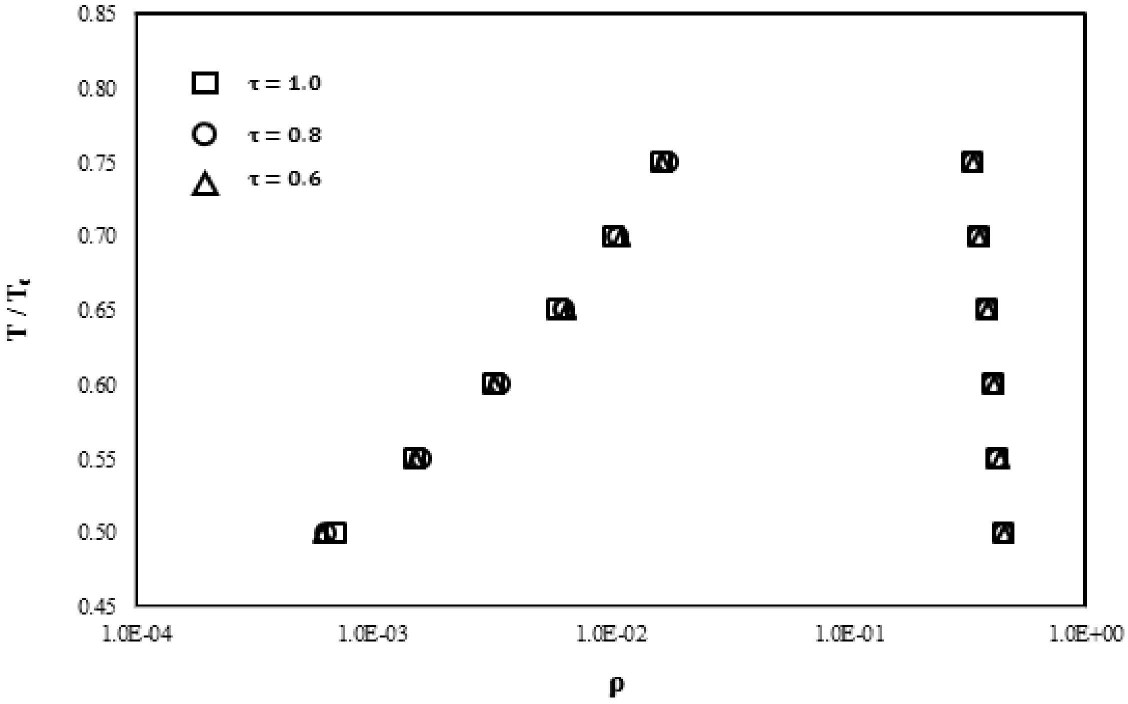

Fig. 7.2. Coexistence curve of C-S EOS at different relaxation times for $\sigma = 0.102$.

Table 7.1. Density ratios obtained with CS-EOS at different temperatures ($\tau = 0.8$).

T/Tc	ρ_l/ρ_g	ρ_l/ρ_g **(Li et al, 2013)**	ρ_l/ρ_g **Analytical**
0.60	0.408/0.00342	0.4079/0.00306	0.407/0.00324
0.55	0.432/0.001604	0.4318/0.001484	0.431/0.00147
0.50	0.456/0.000634	0.4547/0.000639	0.455/0.000606

7.4.2 Evaluating Spatial Accuracy

The spatial accuracy of the LBM multiphase model is tested for the case of a spherical droplet. To test the accuracy of the, we simulated different grid sizes $N_x \times N_y \times N_z = 41 \times 41 \times 41$, $N_x \times N_y \times N_z = 81 \times 81 \times 81$, $N_x \times N_y \times N_z = 121 \times 121 \times 121$ and $N_x \times N_y \times N_z = 181 \times 181 \times 181$. For each case, the radius of the droplet is set as $R = {}^{N_x}/_{4}$. Periodic boundary condition was implemented on all boundaries. Furthermore, we considered the mesh size $N_x \times N_y \times N_z = 181 \times 181 \times 181$ as the finest mesh and assumed the results are accurate. The error of mesh size N_x is defined as $\mathrm{Error}(N_x) = |\rho(N_x) - \rho(181)|$, where $\rho(N_x)$ means the density of the liquid or gas obtained by mesh $N_x \times N_y \times N_z$. Based on the log-log plot of the errors in Figure 7.3, we confirm that the multiphase model is approximately second-order accurate.

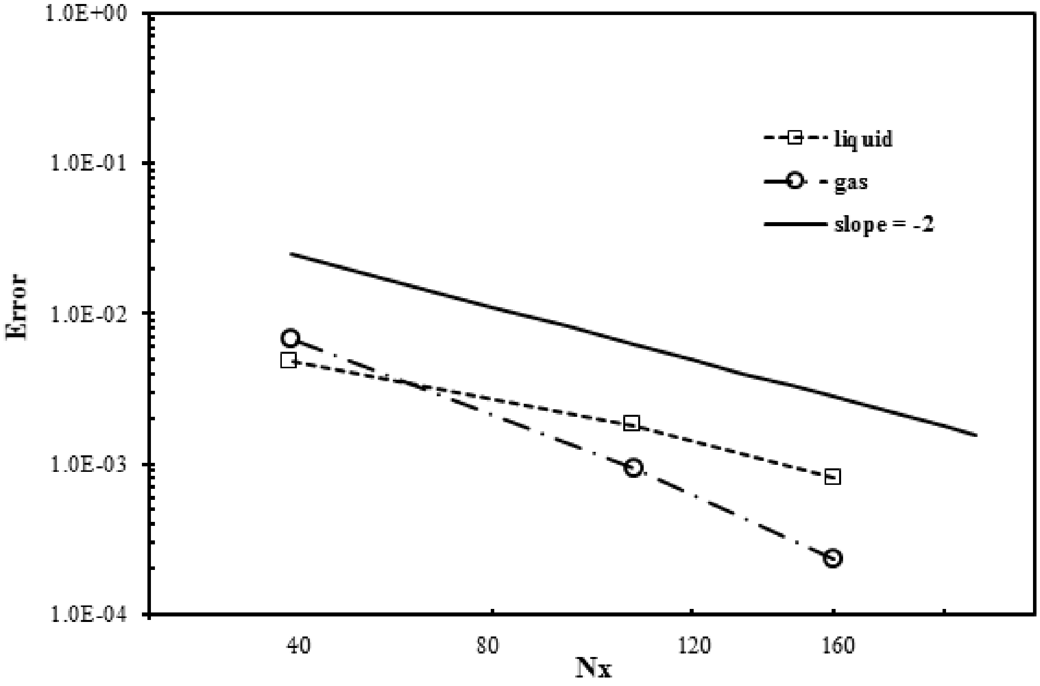

Fig. 7.3. Error of the densities in liquid and gas as a function of the mesh size. The line $\sigma = \text{slope} = -2$ represent the exact second-order spatial accuracy and it is supplied to guide the eyes.

7.4.3 Evaluation of Laplace law

To validate the model with Laplace law, we simulated 5 droplets with 20 < R < 40 lattice units in a 121 × 121 × 121 lattice. Periodic boundary conditions were applied in all three directions of the computational domain and no body force was applied. Initially, the droplets were places at the center of the domain and the density field initialized according to the Eq. (7.9).

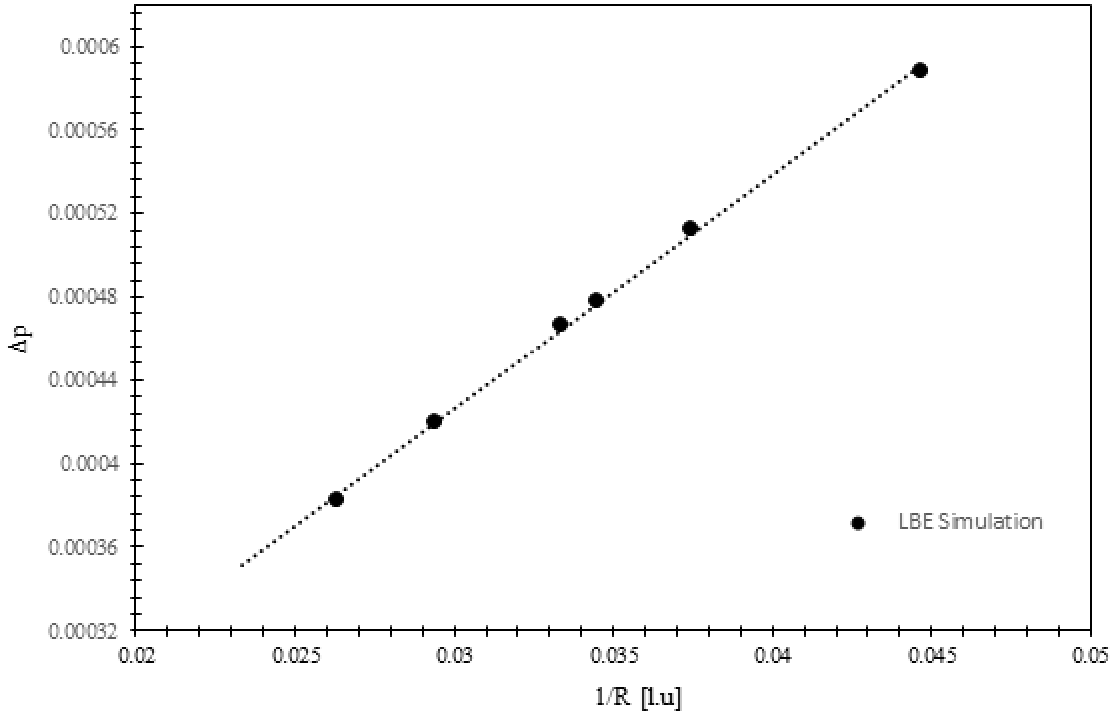

Fig. 7.4. Numerical validation of Laplace's law

In theory, the difference between the liquid and gas pressure is related to the surface tension and the radius of the droplet via the Laplace equation

$$\Delta p = \frac{\gamma}{R} \tag{7.10}$$

where γ is the surface tension, R is the radius of the droplet and Δp is the pressure difference across the interface. The surface tension $\gamma = 0.011$ was obtained from our simulation with a coefficient of determination 0.9988.

7.4.4 Evaluation of contact angles

As explained in section 2, different contact angles can be simulated by adjusting the parameter G_w. In this simulation, we adopted a 121 × 121 ×61 lattice. No-slip boundary conditions were applied on the top and bottom wall (*z*-direction) and periodic boundary condition in the remaining two directions (*x* and *y*). In addition, no body force was applied. The computation domain was initialized with a hemispherical droplet with radius $R = 30$ placed on the bottom wall with the initial density field computed as shown in equation 23. The parameter G_w is adjusted to simulate different contact angles. As the simulation progressed, the initial droplet shape evolved into an equilibrium state and achieved an equilibrium contact angle. The contact angles were measured with Image J LB-ADSA (Stalder et al., 2010). Details of the equilibrium contact angle and the corresponding G_w is provided in Table 7.2.

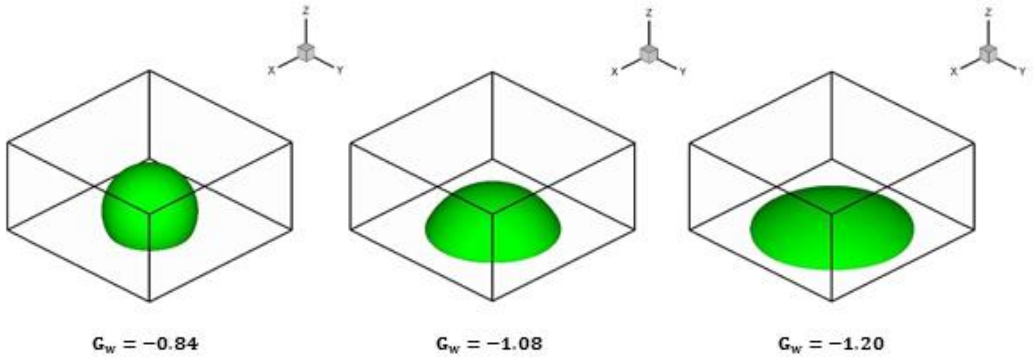

Fig. 7.5 LBM simulation of contact angles with different adhesion interacting force strength $\boldsymbol{G_w}$

Table 7.2. Adhesion interacting force strength $\boldsymbol{G_w}$ for the contact angles using C-S EOS at $T = 0.5T_c$ and $\tau = 0.8$

$\boldsymbol{G_w}$	**Contact Angle (º)**
-0.84	122.8
-1.08	67.4
-1.16	51.4
-1.20	43.5

7.4.5 Passive droplet displacement in a microchannel

We now focus our investigations on parameters that may affect passive droplet displacement by wedge-shaped surface wettability gradient in a microchannel. In our simulations, we considered the following cases, namely: the effect of different wedge-surface relative wettability, the effect of wedge angle, the effect of initial droplet position, and the effect of gravitational force for a droplet on an inclined surface. We first consider cases that involve negligible Bond number (Bond number is the ratio of gravitational force and surface tension forces $Bo = \frac{\Delta\rho g L^2}{\gamma}$). Since the surface tension forces will be dominant for these cases, we did not include the gravitational force (g = 0). Later, we simulated cases that include gravity. We considered a 101 × 301 ×101 computational domain. For boundary conditions, bounce-back boundary conditions were set at the bottom and top walls while periodic boundary conditions were applied on the remaining boundaries. A hemispherical droplet with initial radius $R = 25$ was placed on the bottom wall at lattice coordinates $(50, 260, 0)$.

7.4.6 Effect of Wedge-Surface Relative Wettability

We first analyzed the effect of different wedge-surface relative wettability on the displacement of the droplet. The contact angle of the surface of the bottom wall for the microchannel is set to θ_1 = 122.8^o (blue region in figures). Different contact angles θ_2= 67.4^o, θ_2 = 51.4^o and θ_2 = 43.5^o (red region in figures) were set for the wedges to simulate different degrees of hydrophilicity. To quantify the displacement, we measured the displacement of the trailing and leading edges of the droplet along the centerline x=50 lattice unit. Figure 7.6 show the dynamic behavior of the droplet as it moves along the microchannel for the different wedge relative wettability. We observed that, as the wetting condition on the wedge is increasingly more hydrophilic, the velocity of the leading edge of the droplet along the microchannel increased (Fig. 7.7a and Table 7.3). For example, at lattice time = 40,000 the displacements of the leading edges of the different wedge contact angles (67.4^o), (51.4^o), and (43.5^o), are 164, 196, and 206 lattice units respectively. Interestingly, the displacement of the trailing edge of the droplet produced similar behavior initially but towards the base of the wedge (leading edge is already at the base) we noticed contraction of the contact line of the droplet due to surface tension forces (Fig. 7.7b). Also, we noticed more stretching in the droplet as we reduced the contact angle on the wedge, particularly towards the base of the wedge (Fig. 7.7a). Figure 7.8 provides an insight into the dynamics of the droplet motion. It appears that droplet exhibited some form of creeping motion because there are regions of increasing (stretching) and decreasing (contracting) droplet length.

In general, increase in contact angle on the surface of the microchannel generated an increase in the average velocities of the trailing and leading edges of the droplet

(Table 7.3). This is expected because of the wettability gradient produced by the wedge gradient. Hence, the net adhesion force due to the hydrophilic nature of the wedge and the hydrophobic nature of the surface are in the same direction. That is, on the hydrophobic region, the adhesion force (pointing inward) at the leading edge of the contact line is less than at the trailing edge. Similarly, on the hydrophilic region, the adhesion force (pointing outward) at the leading edge is greater than at the trailing edge. This imbalance in the adhesion force produces a resultant force towards the base of the wedge. If this force is greater than the opposing viscous and frictional forces, an increase in the wedge surface contact angle generates an increase in the average velocity of the droplet (Fig. 7.7).

Meanwhile, this increase in contact angle on the surface of the microchannel appears not to significantly affect the deformation of the droplet (Fig. 7.8). The final droplet shape is consistent with experimental results in (Xianhua et al., 2016).

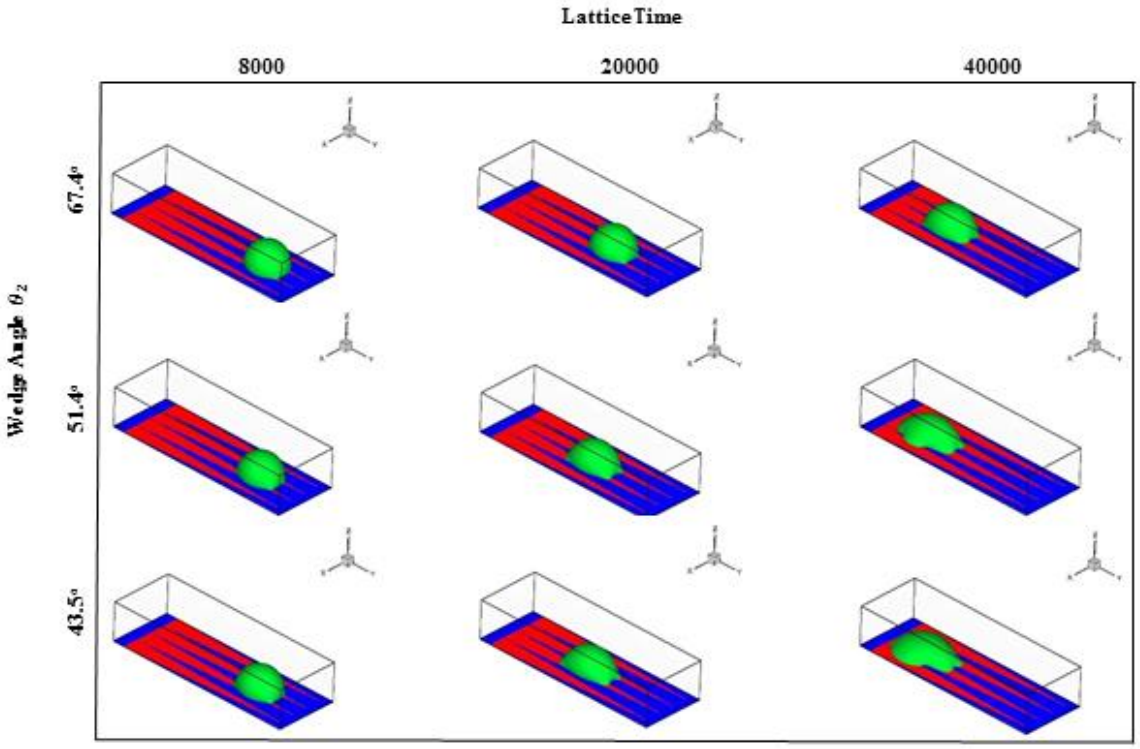

Fig. 7.6 Dynamic behavior of a droplet for different relative wedge wettability ($\theta_1 = 122.8^o$, $\theta_2 = 43.5^o$, $\theta_2 = 51.4^o$ and $\theta_2 = 67.4^o$) at different lattice times

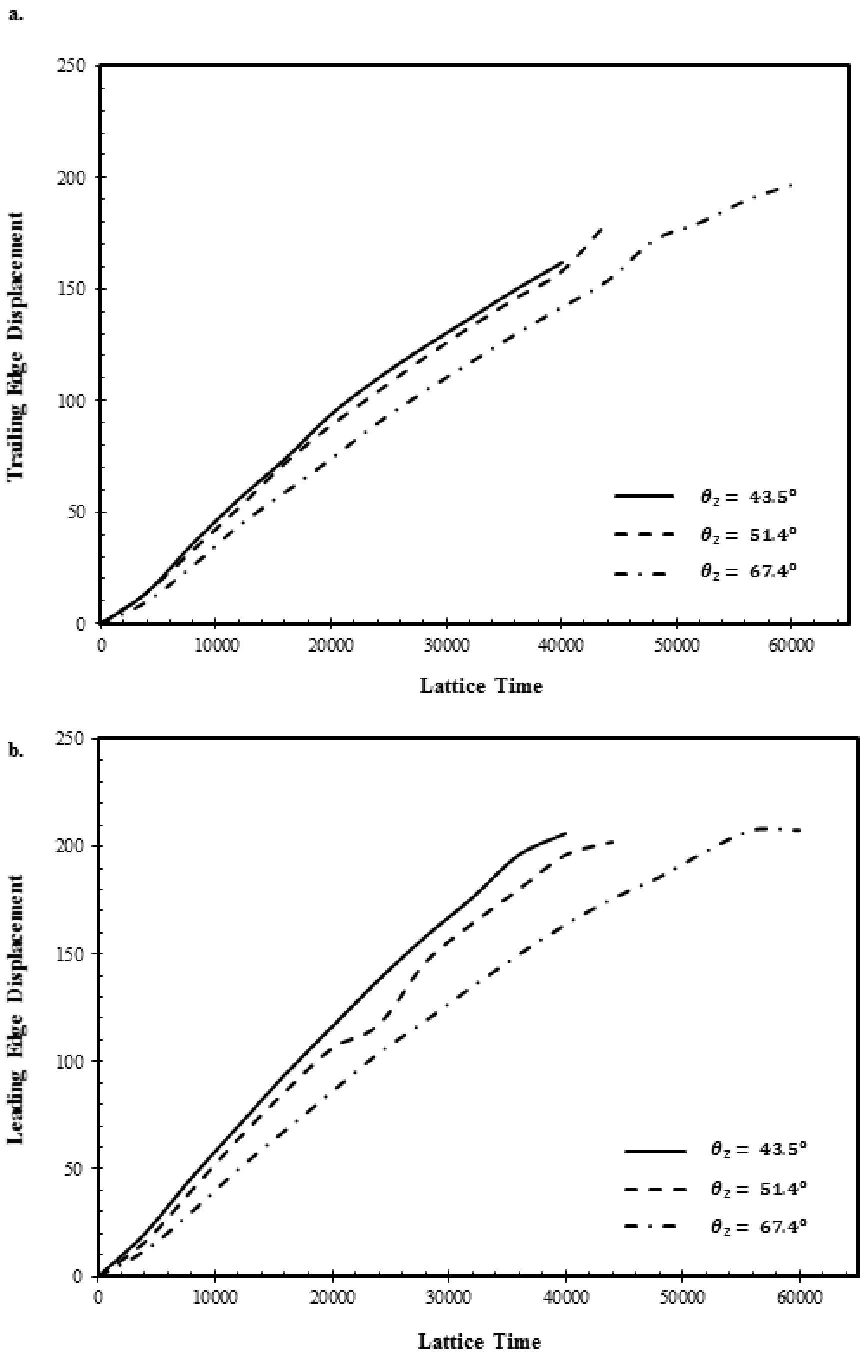

Fig. 7.7 Displacement of droplet as a function of lattice time for different relative wedge wettability ($\theta_1 = 122.8^o$, $\theta_2 = 43.5^o$, $\theta_2 = 51.4^o$ and $\theta_2 = 67.4^o$). (a) Trailing edge of droplet (b) Leading edge of droplet

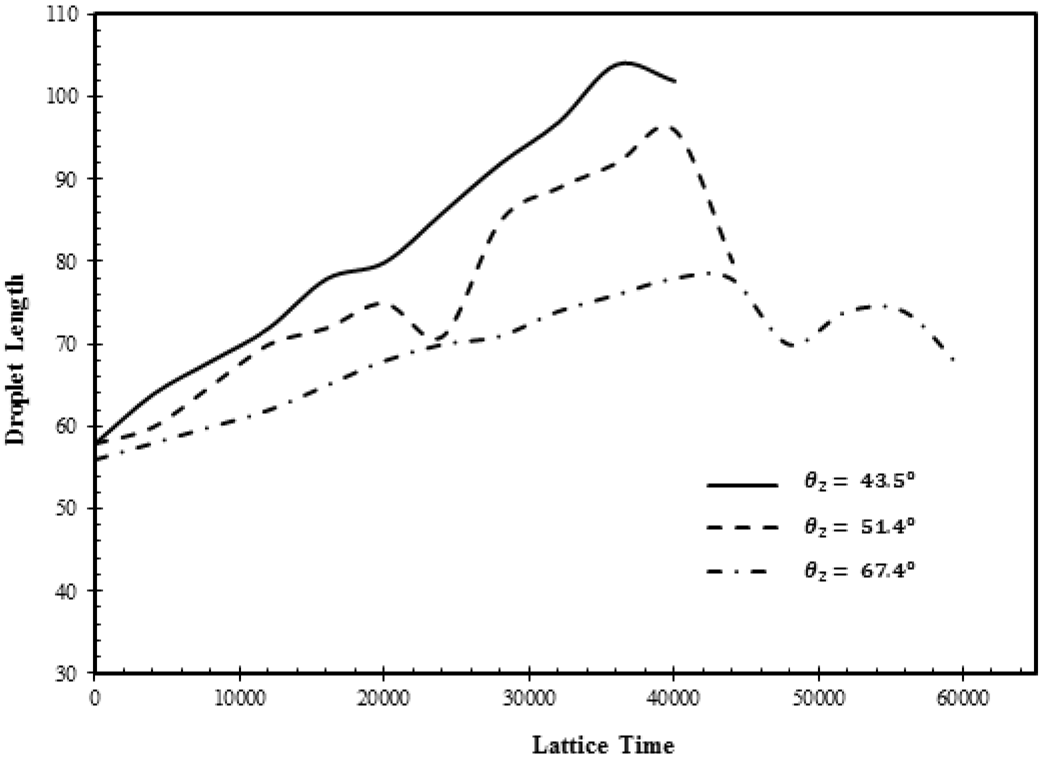

Fig. 7.8 The droplet length as a function of lattice time for different relative wedge wettability ($\theta_1 = 122.8^o$, $\theta_2 = 43.5^o$, $\theta_2 = 51.4^o$ and $\theta_2 = 67.4^o$)

Table. 7.3. Comparison of the average velocities of the trailing and leading edges of the droplet for different wedge-surface wettability configurations

Contact Angle of Surface $\boldsymbol{\theta_1}$ (º)	**Contact Angle of Wedge $\boldsymbol{\theta_2}$(º)**	**Trailing Edge Average Velocity**	**Leading Edge Average Velocity**
122.8	67.4	3.28E-03	3.71E-03
122.8	51.4	4.09E-03	4.59E-03
122.8	43.5	4.05E03	5.15E-03

The above results demonstrate that larger wettability difference between the wedge and surface results in larger driving forces. This in turn has a remarkable influence on the motion of the droplet. We therefore remark that the knowledge of this relationship may provide a model for the optimization of wettability gradient droplet manipulation microfluidic applications.

7.4.7 Effect of Wedge Angle

We also tested the effect of different wedge angles. For this analysis, we selected the case with (122.8º vs. 43.5º) from the previous section above because it generated the highest average velocity. Here, we keep the wedges apex in the same position and adjusted the height of the wedges to obtain different wedge angles. We tested three different wedge angles (β = 5.2º, β = 6.4º and β = 8.2º). Figure 7.9 shows the dynamic behavior of the droplet with different wedge angles (β = 5.2º, β = 6.4º and β = 8.2º). Like our observation from the previous section, the increase in the wedge angle does not appear to significantly alter the deformation of the droplet.

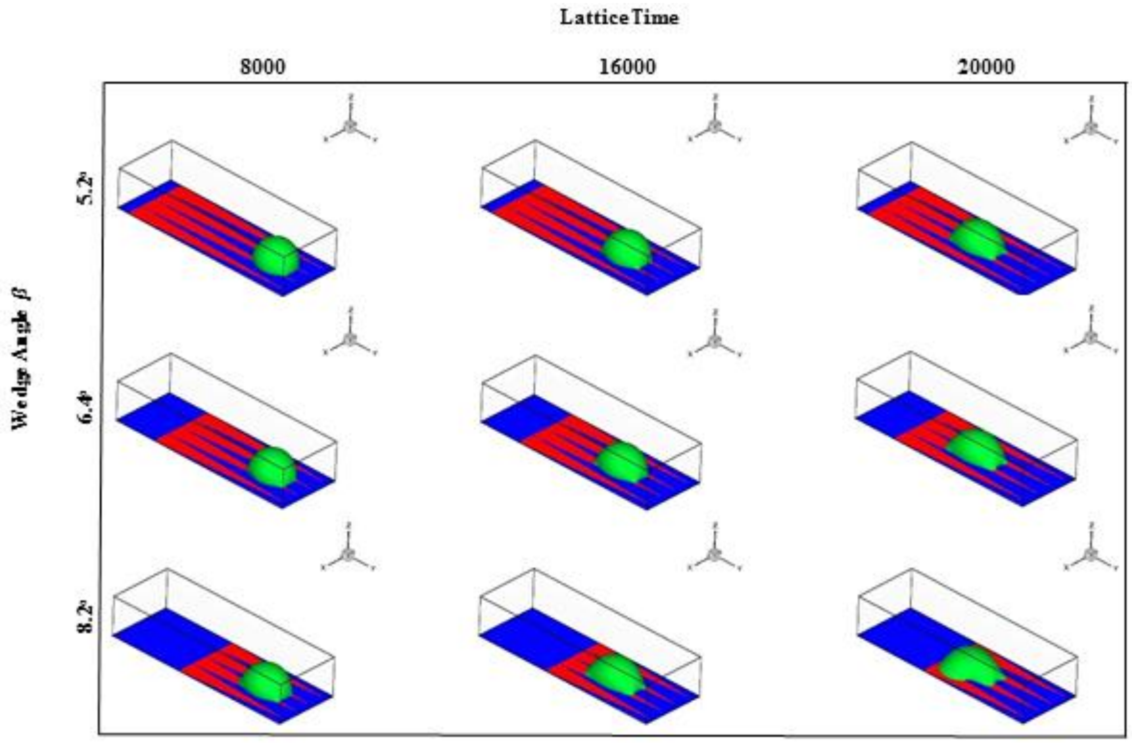

Fig. 7.9 Dynamic behavior of a droplet for different wedge angles (β = 5.2°, β = 6.4° and β = 8.2°) at different lattice times

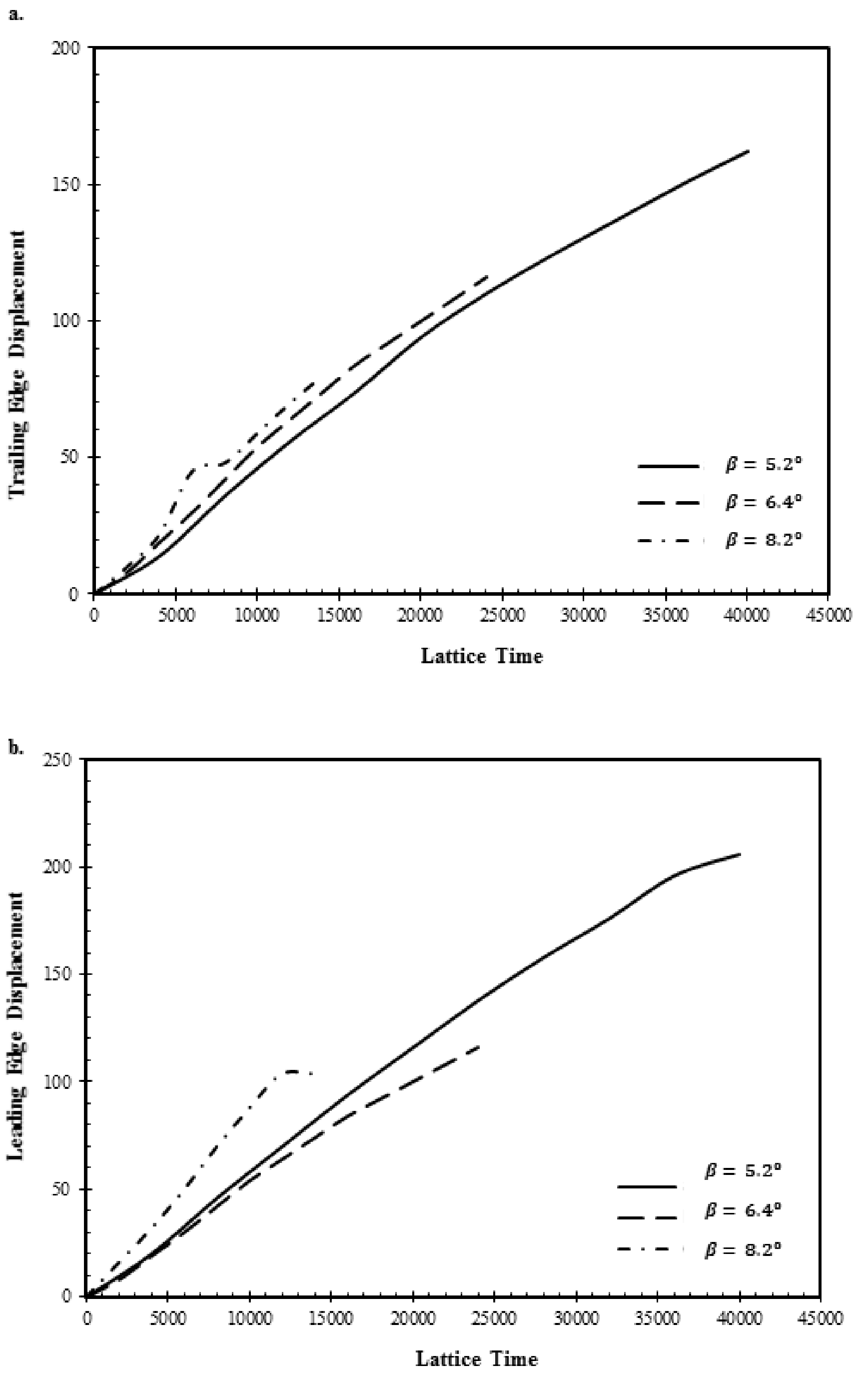

Fig. 7.10 Displacement of droplet as a function of lattice time for different wedge angles (β = 5.2°, β = 6.4° and β = 8.2°). (a) Trailing edge of droplet (b) Leading edge of droplet

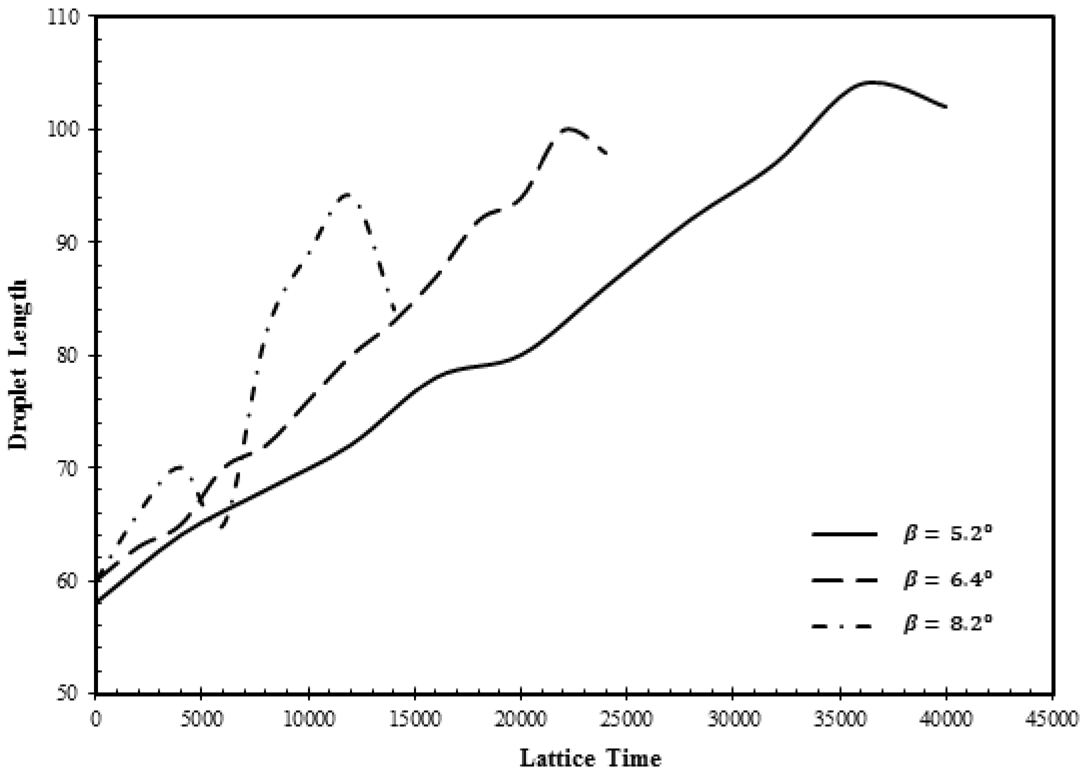

Fig. 7.11 The droplet length as a function of lattice time for different wedge angles (β = 5.2°, β = 6.4°, β = 8.2°)

As we increased the wedge angle, we noticed an increase in the displacement of the trailing and leading edges of the droplet (Fig.7.10a and b). Initially, the droplet starts off stretching and it appears that it attained a critical stretching condition after which it began to contract. In general, the magnitude of this stretching-contracting process increased with the increase in the wedge angle (Fig. 7.11).

Table. 7.4. Comparison of the average velocities of the trailing and leading edges of the droplet for different -wedge angles.

Wedge Angle $\boldsymbol{\beta}$ **(°)**	**Trailing Edge Average Velocity**	**Leading Edge Average Velocity**
5.2	4.05E-03	5.15E-03
6.4	4.83E-03	8.92E-03
8.2	5.71E-03	7.43E-03

Table 7.4 shows the average velocities of the trailing and leading edges of the droplet for different wedge angles. We observed 1.73 folds increase in the leading edge average velocity for a wedge angle increase from β = 5.2° to β = 6.4°. It appears that there exists a critical wedge angle, above which the average velocity of the leading edge begins to decrease. For example, table 4 show a 1.2 folds decrease in the average velocity of the leading edge of the droplet when the wedge angle was increased from β = 6.4° to β = 8.2°. The above result demonstrates that the average velocity of the droplet can be increased by increasing the wedge angle.

7.4.8 Effect of Droplet Initial Position

In this section, we investigate the effect of droplet initial position on the droplet dynamics. In the previous sections, the microchannel contained four wedges and the droplet was pinned by the apexes of two middle wedges. To simulate a different initial wedge position, we increased the number of wedges to five so that apexes of three middle wedges will pin the droplet. Similarly, we selected the (122.8° vs. 43.5°) configuration from previous sections for easy comparisons.

We first compared the deformation of the droplet on 4-wedge microchannel to the 5-wedge microchannel (Fig. 7.12). As expected, we observed more spreading and flattening of the droplet in the 5-wedge microchannel. Although, we observed similar displacement profiles for the leading and trailing edges of the droplet for the 4-wedge and 5-wedge microchannel, however, the 5-wedge cases generated slightly larger average velocities for both the leading and trailing edges of the droplet (Fig. 7.13).

Next, we increased the wedge angle and consistent with our results from the 4-wedge microchannel, we observed similar pattern of increase in the average velocities of the leading and trailing edges (Fig. 7.14 and Fig. 7.15). Interestingly, in Figure 7.16a for the droplet length, we noticed an initial stretching-contracting cycle prior to attaining critical stretching when the wedge angles are β = 5.2^o and β = 8.2^o for the 5-wedge microchannel. Nonetheless, we observed more stretching (greater magnitude of droplet length) in the 5-wedge microchannel (Fig. 7.16b). To compare the effect of the position of the droplet on the average velocities of the trailing and leading edges of the droplet, we fixed the wedge angle to β = 5.2^o for both the 4-wedge and 5-wedge microchannel. Table 5 shows a slight increase in the leading and trailing edge average velocities in the 5-wedge case. Similar to our observations in the 4-wedge case, the average velocities decreased when the wedge angle was increased from β = 6.4^o to β = 8.2^o.

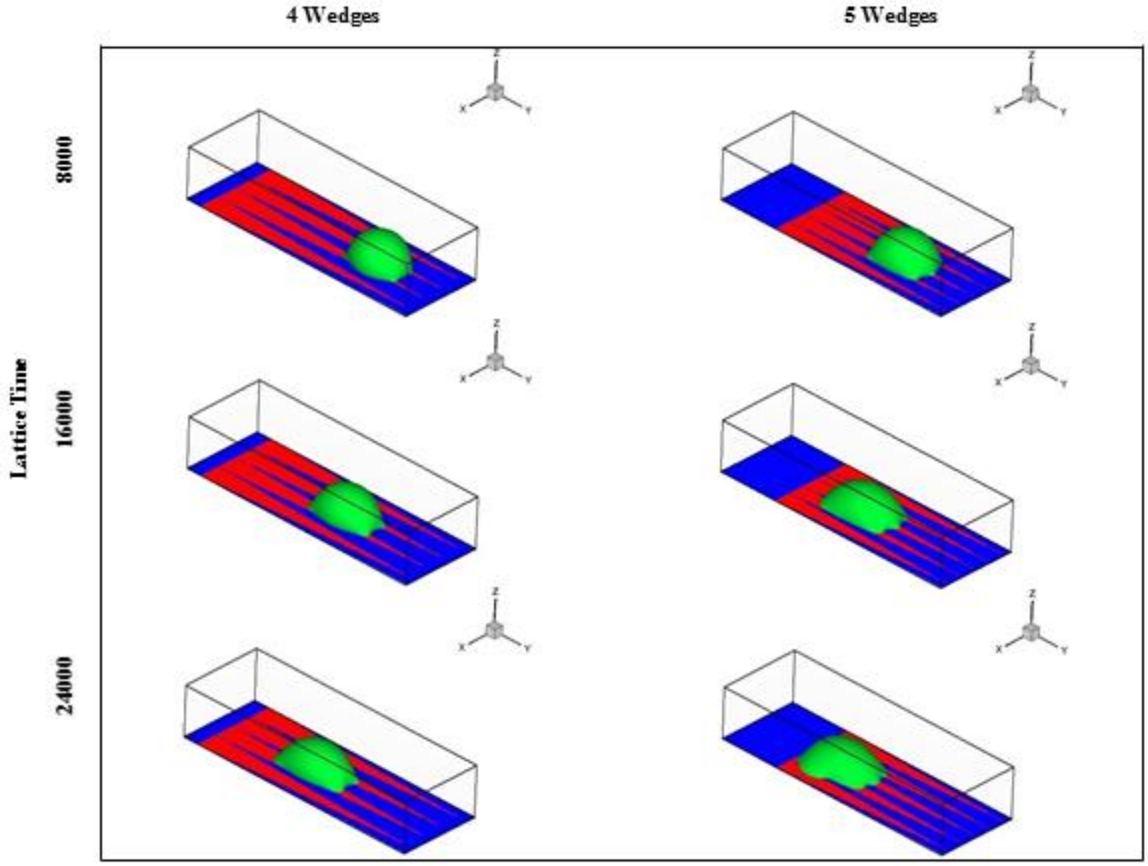

Fig. 7.12. Dynamic behavior of a droplet pinned by two and three wedges at different lattice times. Note: the height of the wedges was reduced for the 5-wedge case in other to keep the wedge angles the same for both cases ($\beta = 5.2^{o}$)

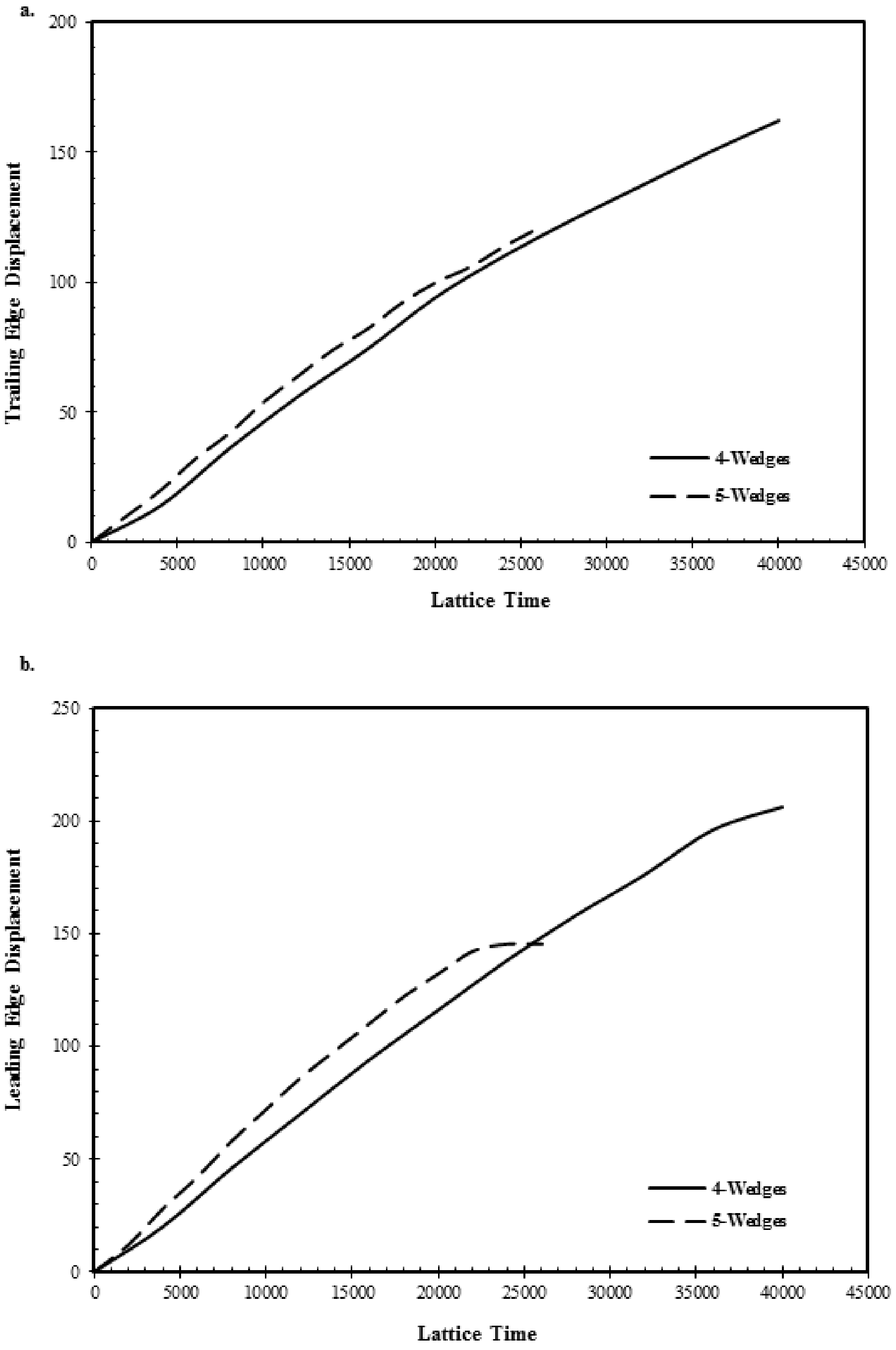

Fig. 7.13 Comparison of the displacement of droplet as a function of lattice time for 5-wedge and 4-wedge when $\beta = 5.2^o$ (a) Trailing edge of droplet (b) Leading edge of droplet

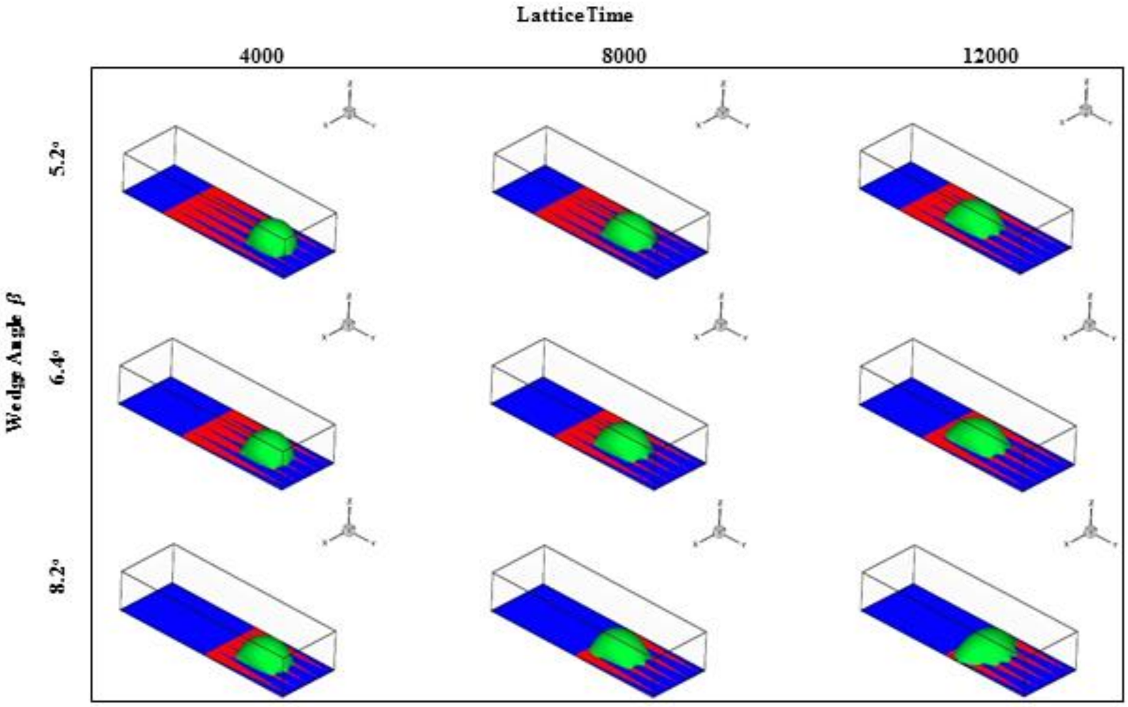

Fig. 7.14. Dynamic behavior of a droplet pinned by three wedges for different wedge angles ($\beta = 5.2^{\circ}$, $\beta = 6.4^{\circ}$, $\beta = 8.2^{\circ}$) at different lattice times

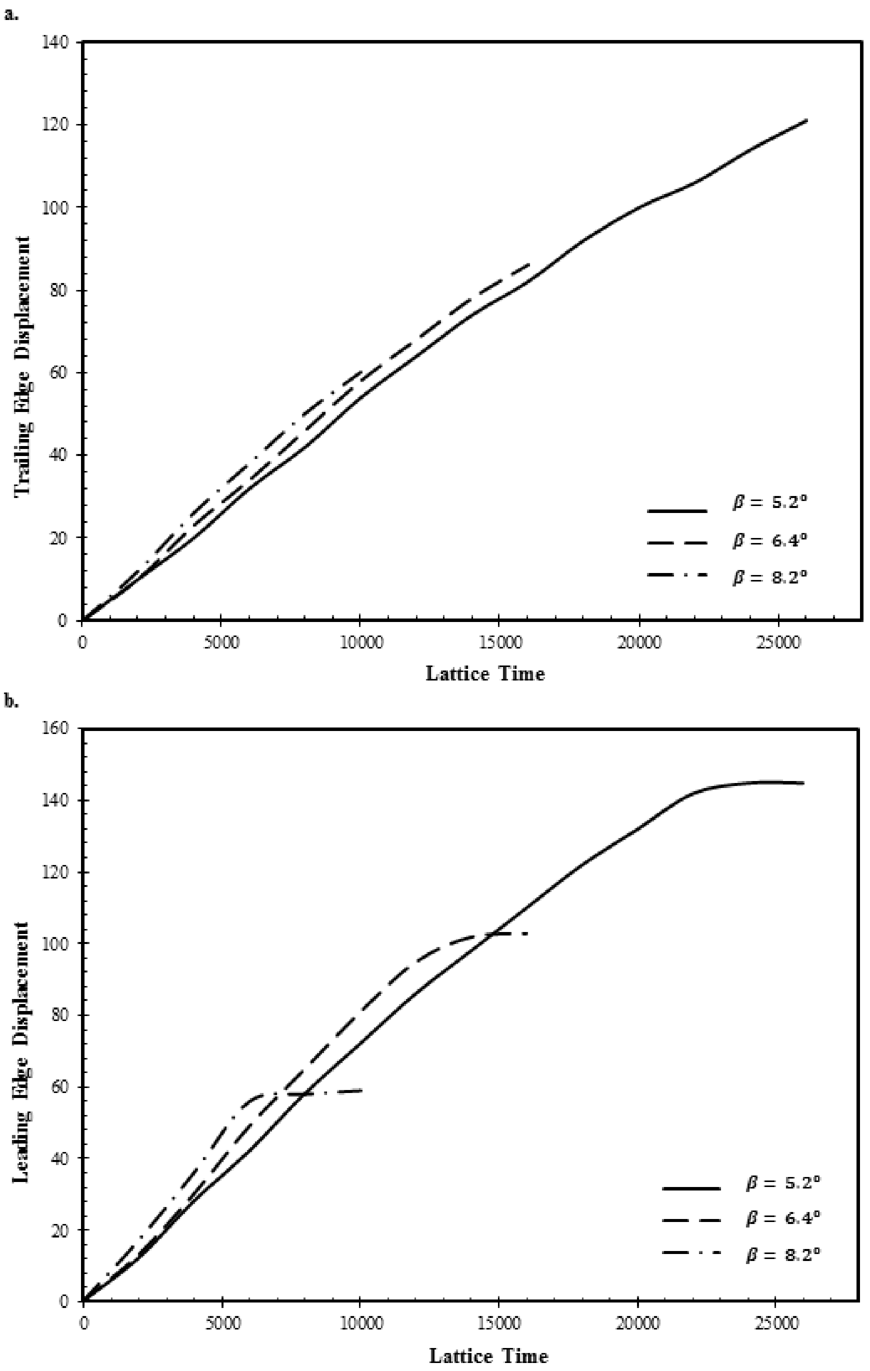

Fig. 7.15 Displacement of droplet as a function of lattice time for different wedge angles (β = 5.2°, β = 6.4°, β = 8.2°) in the 5-wedge case (a) Trailing edge of droplet (b) Leading edge of droplet

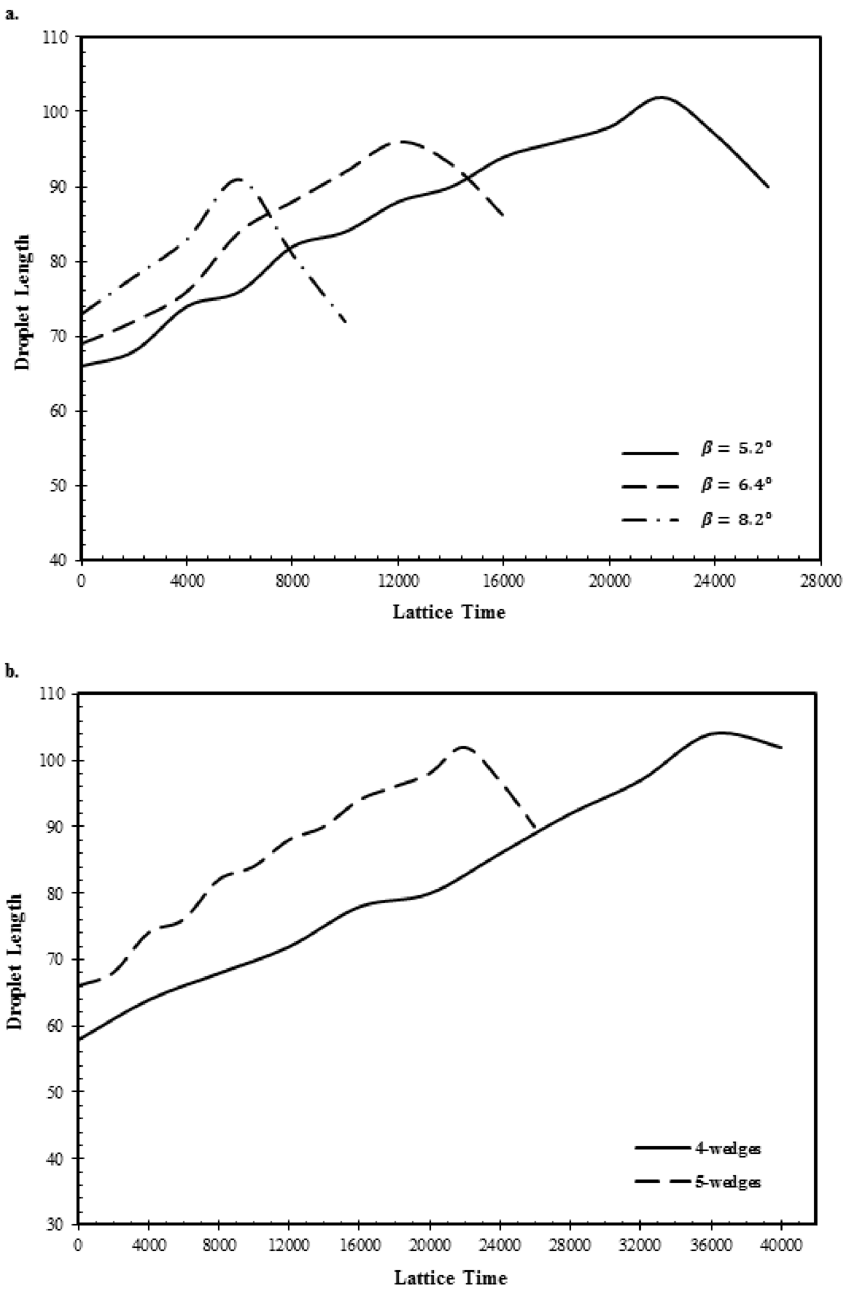

Fig. 7.16 The droplet length as a function of lattice time (a) Different wedge angles for the 5-wdge case (β = 5.2°, β = 6.4°, β = 8.2°) (b) 4-wedge case compared to 5-wedge case

Table. 7.5. Comparison of the average velocities of the trailing and leading edges of the droplet for different wedge configurations and wedge angles

Number of Wedges	**Wedge Angle $\boldsymbol{\beta}$ (º)**	**Trailing Edge Average Velocity**	**Leading Edge Average Velocity**
4	5.2	4.05E-03	5.15E-03
5	5.2	4.65E-03	5.58E03
	6.4	5.38E-03	6.44E-03
	8.2	5.00E-03	4.92E-03

7.4.9 Effect of Gravitational Force

In all previous cases, the effect of gravity was neglected. For comparison, we repeated (122.8º vs. 43.5º) case but this time around we included the body force $\mathbf{F}_{body} = \rho\boldsymbol{g}$ where $\boldsymbol{g}$ is the acceleration of gravity and ρ is the density of the phase. The gravitational acceleration $\boldsymbol{g} = (0,\ 0,\ g_z)$ is set to different values to simulate different droplet volumes. Namely: $1.0\ \mathrm{E}-05$, $5.0\ \mathrm{E}-06$, $2.5\ \mathrm{E}-05$, and $1.0\ \mathrm{E}-06$ lattice units (Table 7.6 and Fig. 7.17). We can observe in figure 16 that the profiles of the droplet length for the cases with gravity converges to the no-gravity case as the volume of the droplet decreases. As such, we believe there exists a critical droplet volume, for the cases presented in this study, below which the effect of gravity becomes negligible. Here our result show that below 0.156 (nL) droplet volume, gravitational acceleration can be neglected (Fig. 7.18).

Table. 7.6. Different droplet volumes in physical units simulated by varying $\mathbf{g}$.

$\mathbf{g}$	$\boldsymbol{\delta_x}\ (\mathbf{m})$	$\boldsymbol{\delta_t}\ (\mathbf{s})$	$\boldsymbol{V}\ (\mathbf{nL})$
1.0 E-06	1.4031E-06	1.1845E-06	0.156
2.5 E-06	1.9042E-06	2.1818E-06	0.391
5.0 E-06	2.3992E-06	3.4635E-06	0.780
1.0 E-05	3.0228E-06	5.4980E-06	1.560

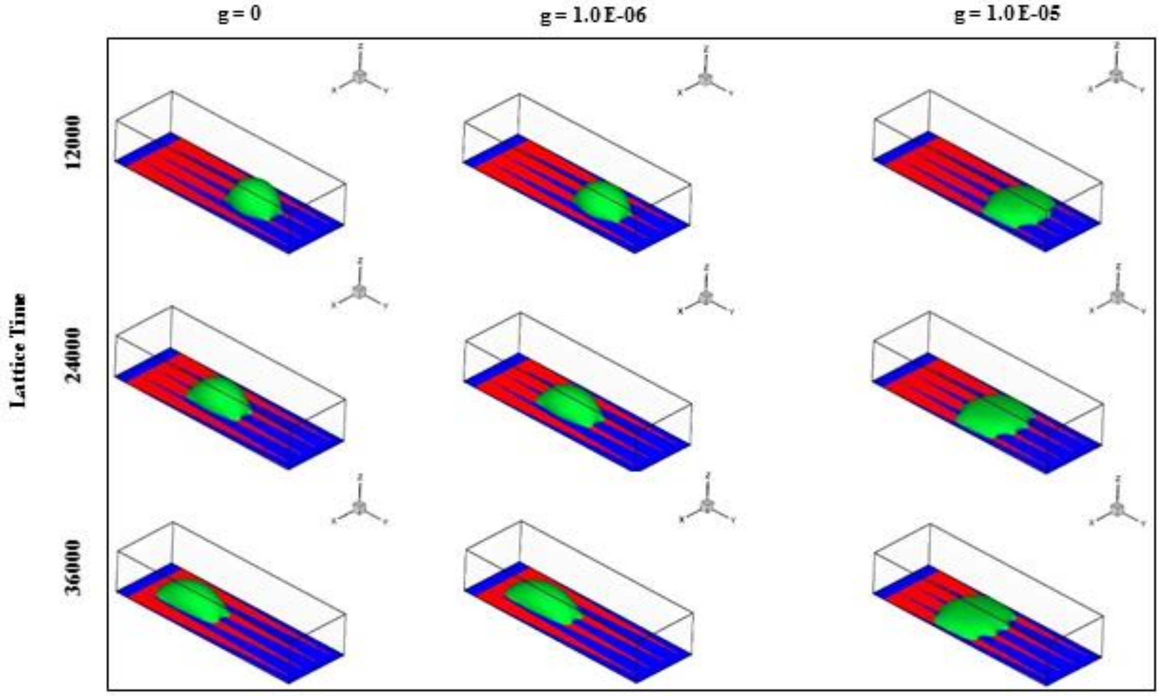

Fig. 7.17 Dynamic behavior of a droplet with and without gravitational accelerations

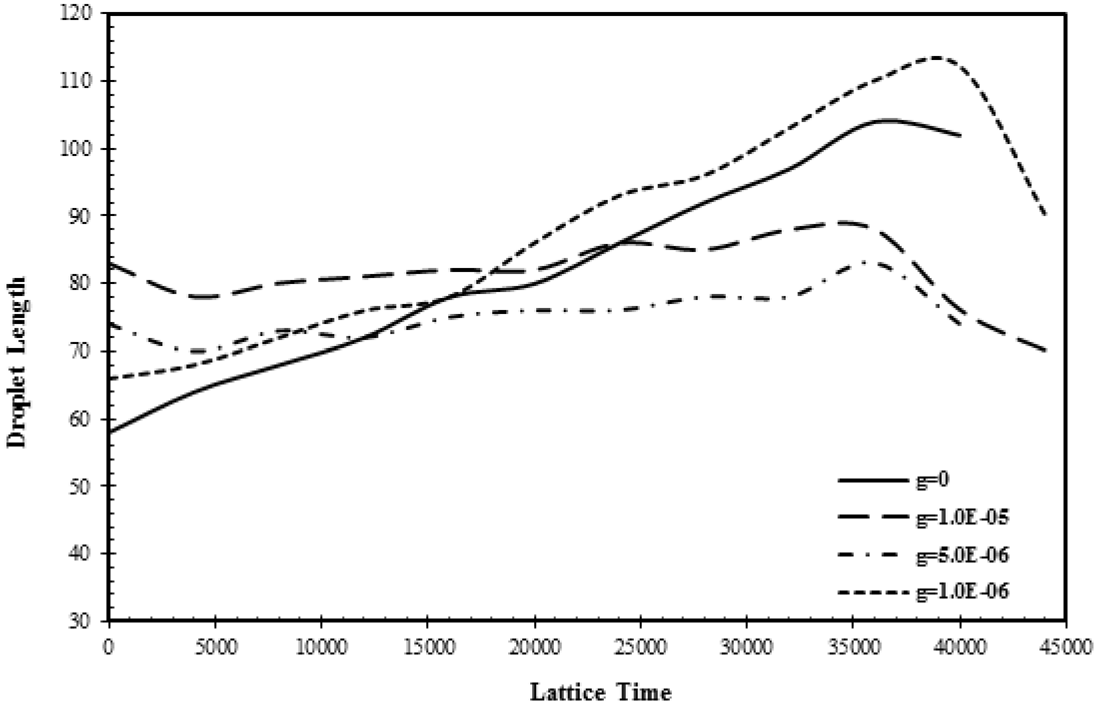

Fig. 7.18 The droplet length as a function of lattice time for different values of **g**

To further investigate the effect of the gravitational force, we simulated the displacement of a droplet ascending along an inclined microchannel with different angles of inclinations ($\alpha = -6^o$, $\alpha = -8^o$ and $\alpha = -12^o$). First we discuss our results when the volume of the droplet is 0.78 (nL). Contrary to our expectations, $\alpha = -12^o$ case was the only case that generated meaningful spontaneous motion of the droplet up the incline (Fig. 7.19 and Table 7.7). This suggests that there is an interplay between the profile of the contact line of the droplet and the driving forces. In contrast, for the 0.39 (nL) droplet, the average velocities of the droplet up the incline generally decreased as the angle of inclination of the microchannel was increased (Table 7.7). At $\alpha = -12^o$, the droplet was pinned to the bottom wall of the microchannel (Fig. 7.20). Finally, for the 0.16 (nL) droplet, the profile of the droplet was consistent with the no-gravity case (Fig. 7.21). In addition, like our observations in the 0.39 (nL) droplet, the average velocities of the droplet decreased with increase in the angle of inclination. However, the velocities are an order of magnitude larger (Table 7.7).

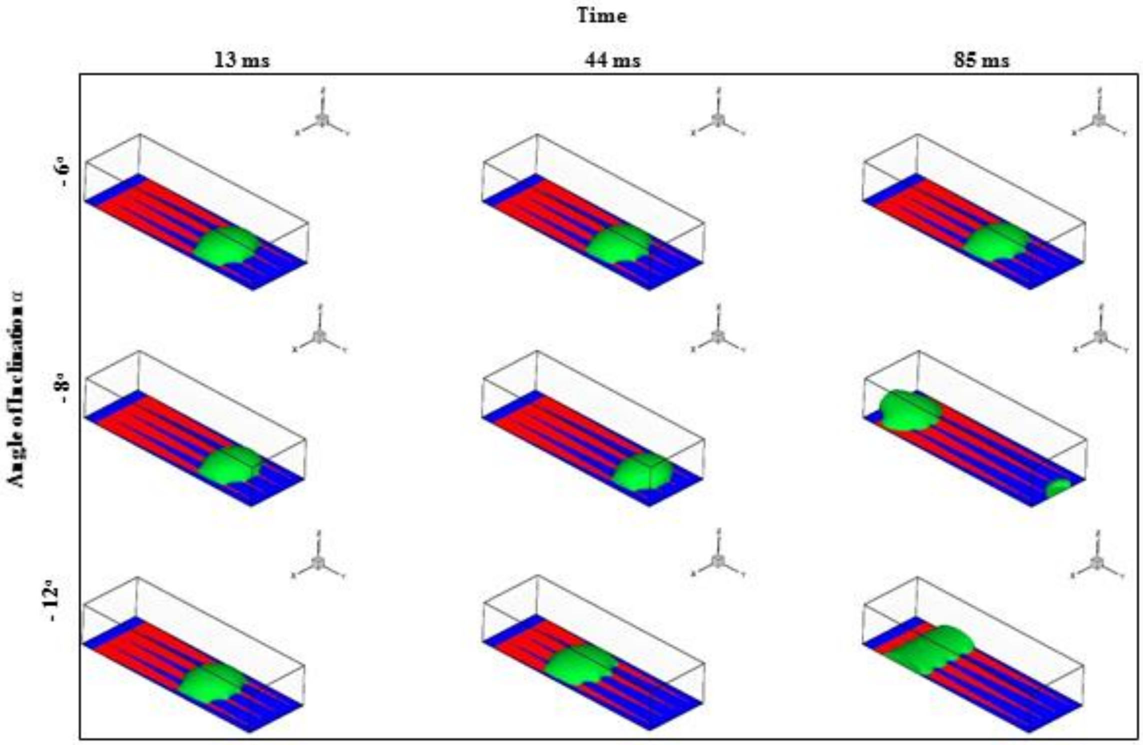

Fig. 7.19 Dynamic behavior of a droplet for different angles of inclination ($\alpha = -6^o$, $\alpha = -8^o$ and $\alpha = -12^o$) for 0.78 (nL) droplet at different times (in milliseconds)

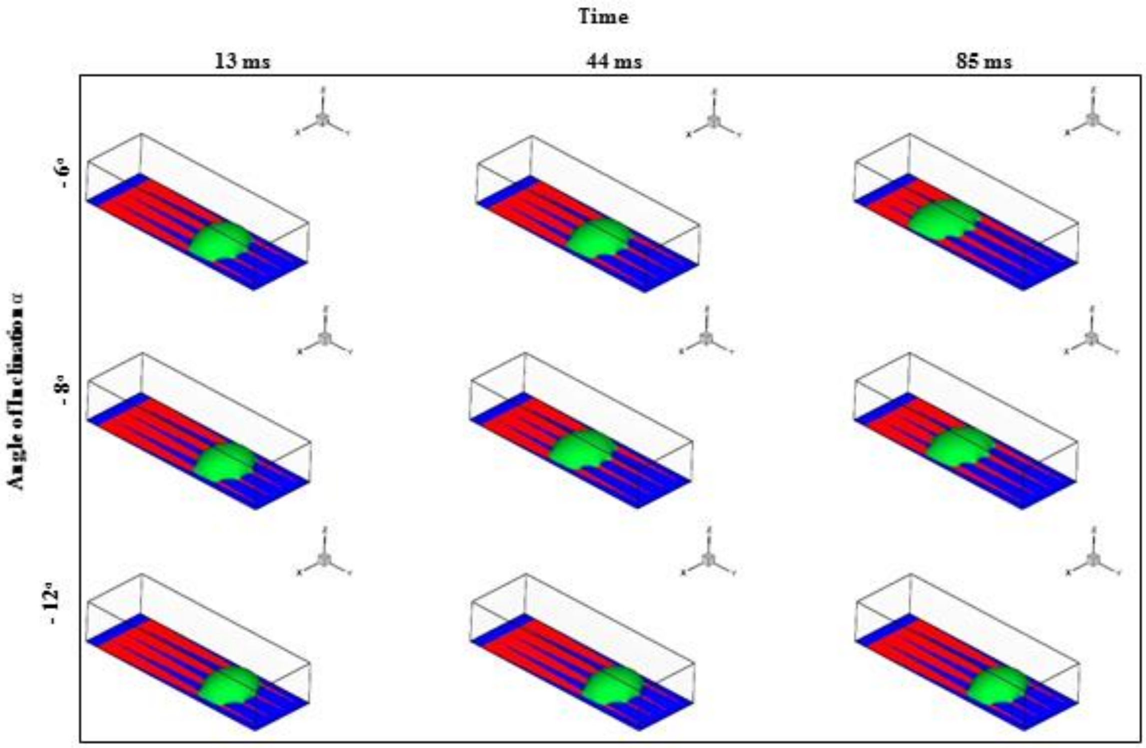

Fig. 7.20 Dynamic behavior of a droplet for different angles of inclination ($\alpha = -6^{\circ}$, $\alpha = -8^{\circ}$ and $\alpha = -12^{\circ}$) for 0.39(nL) droplet at different times (in milliseconds)

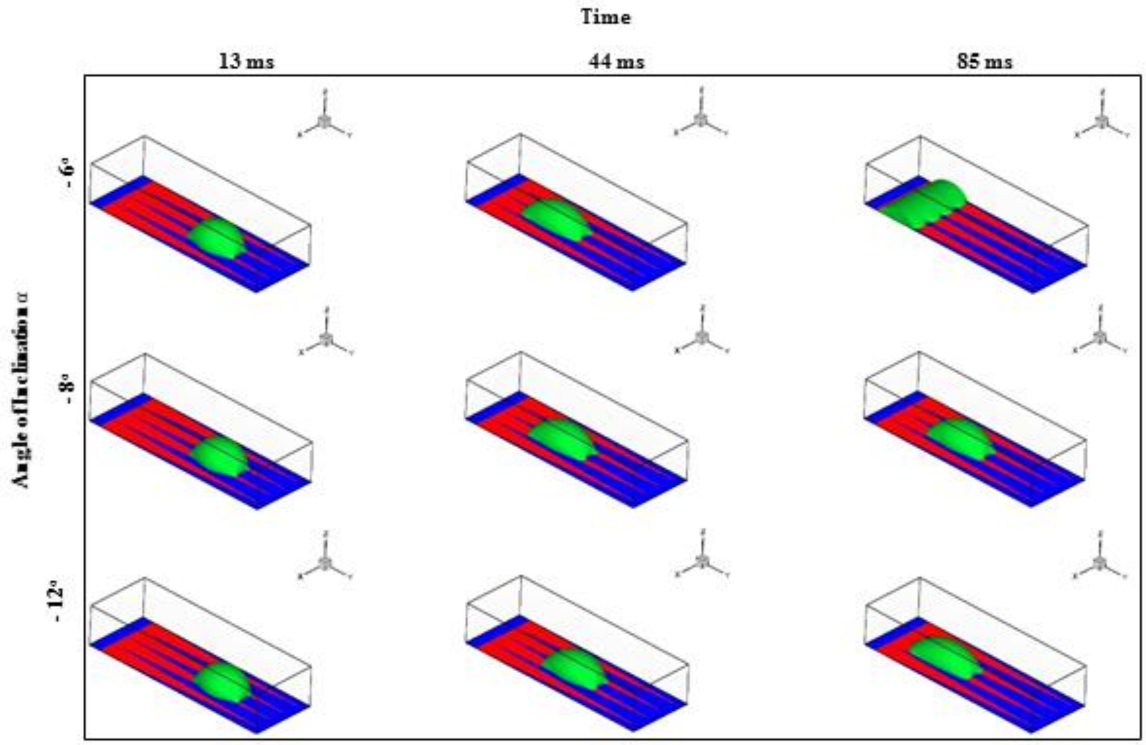

Fig. 7.21 Dynamic behavior of a droplet for different angles of inclination ($\alpha = -6^{o}$, $\alpha = -8^{o}$ and $\alpha = -12^{o}$) for 0.16 (nL) droplet at different times (in milliseconds)

Table. 7.7. Comparison of the average velocities ($^{m}/_{s}$) of the droplet up an incline with different angles of inclination

$\boldsymbol{V}$ **(nL)**	$\boldsymbol{\alpha = -6^{o}}$	$\boldsymbol{\alpha = -8^{o}}$	$\boldsymbol{\alpha = -12^{o}}$
0.156	1.6184E-03	1.2642E-03	1.0763E-03
0.391	8.2001E-04	5.4667E-04	--
0.780	--	--	1.2561E-03

7.5 Conclusion

In this study, a pseudopotential single component multiphase lattice Boltzmann method was successfully adopted to investigate the effects of different droplet parameters on the automatic motion of the droplet in a microchannel. We considered the effects of wedge-surface relative wettability, wedge angle, initial droplet position on wedges, and gravity and microchannel angle of inclination for a descending or ascending droplet.

Accordingly, we implemented an MRT pseudopotential LBM and incorporated the fluid interaction force via the improved forcing scheme proposed by Li et al. (2013) to overcome the density ratio restriction on the original Shan and Chen model (Shan and Chen 1993). Furthermore, we employed the Carnahan-Starling equation of state (Carnahan and Starling 1970a, b) and incorporated it into the model via the method proposed by Yuan and Schafer (Yuan and Schaefer 2006).

Our numerical results demonstrate that:

a. The relative wettability between the different regions of the michrochannel surface influences the motion of the droplet. We discovered that the average velocity of the droplet increases monotonically with increase in this relative wettability. In addition, we noticed that the profile of the droplet was not significantly deformed even as the contact angle of the hydrophilic wedges were decreased.

b. The average velocity increased with the wedge angle. For example, we obtained 1.73 folds increase in the average velocities of the droplet leading edge when the wedge angle was increased from $\beta = 5.2^{o}$ to $\beta = 6.4^{o}$. Unlike increase in the magnitude of relative wettability, increasing the wedge angle to β = 7.2^{o} resulted in a decrease in the average velocities of the trailing and leading edges of the droplet. Therefore, we conclude that there exists a critical wedge angle above which the average velocities begin to decrease due to hysteresis effect.

c. For the cases in this paper, there exists a critical droplet volume (0.156 nL) below which gravitational effects are negligible. In general, for the ascending droplet, we observed that the average velocity of the droplet up the incline decreases with increase in the angle of inclination. More importantly, we discovered a possible interplay between the droplet profile and the capillary driving forces. For example, we noticed a reversal in the direction of the motion of the droplet when the angle of inclination $\alpha = -8$ even though $\alpha = -12$ generated an uphill motion for the case when the droplet volume is 0.78 nL.

In summary, we were successfully able to investigate different parameters that affect droplet dynamic behavior on a patterned-wettability surface using an improved single component multiphase (SCMP) multi-relaxation time (MRT) lattice Boltzmann equation. Through this model we obtained a realistic density ratio that is approximately 720. Along the way, we discovered possible interplay between the droplet profile and the capillary driving forces. This result calls for a more detailed investigation of this droplet dynamic behavior.

7.6 References

Carnahan NF, Starling KE (1970) Analytical Equation for Rigid Spheres: Application to the Model of Longuet-Higgins and Widom for the Melting of Argon Physical Review A 1:1672-1673

Carnahan NF, Starling KE (1970) Thermodynamic Properties of a Rigid-Sphere Fluid The Journal of chemical physics 53:600-603 doi:doi:http://dx.doi.org/10.1063/1.1674033

Gambosi TI (1994) Kinetic theory of gases Cambridge atmospheric and space science series

Huang H, Krafczyk M, Lu X (2011) Forcing term in single-phase and Shan-Chen-type multiphase lattice Boltzmann models Physical Review E 84:046710

Humières D (2002) Multiple–relaxation–time lattice Boltzmann models in three dimensions Philosophical Transactions of the Royal Society of London Series A: Mathematical, Physical and Engineering Sciences 360:437

Li Q, Luo KH, Kang QJ, Chen Q (2014) Contact angles in the pseudopotential lattice Boltzmann modeling of wetting Physical Review E 90:053301

Li Q, Luo KH, Li XJ (2012) Forcing scheme in pseudopotential lattice Boltzmann model for multiphase flows Physical Review E 86:016709

Li Q, Luo KH, Li XJ (2013) Lattice Boltzmann modeling of multiphase flows at large density ratio with an improved pseudopotential model Physical Review E 87:053301

Martys NS, Chen H (1996) Simulation of multicomponent fluids in complex three-dimensional geometries by the lattice Boltzmann method Physical Review E 53:743-750

Raiskinmäki P, Shakib-Manesh A, Jäsberg A, Koponen A, Merikoski J, Timonen J (2002) Lattice-Boltzmann Simulation of Capillary Rise Dynamics Journal of Statistical Physics 107:143-158 doi:10.1023/A:1014506503793

Shan X (2008) Pressure tensor calculation in a class of nonideal gas lattice Boltzmann models Physical Review E 77:066702

Shan X, Chen H (1993) Lattice Boltzmann model for simulating flows with multiple phases and components Physical Review E 47:1815-1819

Shan X, Chen H (1994) Simulation of nonideal gases and liquid-gas phase transitions by the lattice Boltzmann equation Physical Review E 49:2941-2948

Stalder AF, Melchior T, Müller M, Sage D, Blu T, Unser M (2010) Low-bond axisymmetric drop shape analysis for surface tension and contact angle measurements of sessile drops Colloids and Surfaces A: Physicochemical and Engineering Aspects 364:72-81 doi:http://dx.doi.org/10.1016/j.colsurfa.2010.04.040

Sukop MC, Thorne DTJ (2007) Lattice Boltzmann Modeling: An Introduction for Geoscientists and Engineers. Springer Publishing Company, Incorporated,

Xianhua T, Yiying Z, Tielin S, Zirong T, Guanglan L (2016) Patterned gradient surface for spontaneous droplet transportation and water collection: simulation and experiment Journal of Micromechanics and Microengineering 26:115009

Yuan P, Schaefer L (2006) Equations of state in a lattice Boltzmann model Physics of Fluids 18:042101 doi:doi:http://dx.doi.org/10.1063/1.2187070

8. CHAPTER EIGHT: CONCLUSIONS AND FUTURE WORKS

The motivation behind this study was to apply the lattice Boltzmann method to model passive (spontaneous) droplet motion on microchannels with wettability patterned surface. We started by first evaluating different pseudo-potential based multicomponent multiphase wetting models. Our results demonstrated that the models with virtual fluids on the solid node outperformed the ones without. In this first study, we implemented the original Shan and Chen velocity shift forcing scheme. However, in recent years, many improvements have been made to the original Shan and Chen model to address some of its limitations. Therefore, in the subsequent study we incorporated these improvements in pseudo-potential based lattice Boltzmann method and addressed the following areas of improvement:

1. The problem of thermodynamic inconsistencies.
2. Incorporated interaction force that is consistent with the hydrodynamic equations.
3. Improved model to obtain large density ratio.
4. Implemented a multi-relaxation-time model as the single-relaxation-time model is known to be viscosity-dependent.

Following these improvements in our custom code, we investigated the effects of different droplet parameters on the spontaneous motion of a droplet on a microchannel with multi-wedge-shape wettability patterned bottom wall. These droplet parameters are: wedge-surface relative wettability, wedge angle, droplet initial position and effect of gravitational force. Since the phases are well separated (large density ratio) we used the single component multiphase model for this study. With the improvements, we could obtain a realistic density ratio (water-air system) that is approximately 720. Furthermore, we discovered possible interplay between the droplet profile and the capillary driven forces. Our results, demonstrated a critical droplet volume (0.78 nL) below which the effect of gravitational force becomes negligible. In general, our results are consistent with available test data in open literature as well as other numerical studies using techniques different from lattice Boltzmann method.

For future work, the work in this study for large density ratio should be extended to the multicomponent multiphase models (we have conducted preliminary research in this area). In addition, a more extensive study on the interplay between the capillary and inertia forces for a droplet on a microchannel with ideal and rough surfaces could be the subject of future studies. Equally important, is an experimental study to validate the results of the numerical work in this study. Finally, this study presents an insight into the potential use of lattice Boltzmann method for design and optimization of passive on-chip droplet manipulation techniques. This is particularly essential for the design of future point-of-care technologies. Most of these technologies often involve blood-air systems. Therefore, the work in this study should also be extended to the simulation of non-Newtonian fluids.